Hybrid PDE-ABM models: from oncology to virology

PhD Thesis

Sadegh Marzban
Supervisor: Gergely Röst, PhD

Doctoral School of Mathematics and Computer Science
University of Szeged, Bolyai Institute

Szeged
2023

Contents

List of Figures

List of Tables

Chapter 1

Introduction

1.1 Agent-Based Modeling (ABM)

Mathematical models describing natural phenomena can be encoded into computer programs, and then the behaviour of the system can be simulated. Beyond representing equations defined in the mathematical models, computer simulations can offer higher flexibility and finer resolution than we can analyse by equation based models. In this work, we strive for taking advantages of both methods: combining differential equations with computational simulations, we have access to the insights gained from mathematical analysis, and also to the rich dynamical behaviours we can observe by performing a large amount of computations.

A simulation utilizing agent-based modeling (ABM) involves capturing the properties and behaviors of abstract entities known as agents. Each agent in an ABM possesses characteristics and behaviors, and can act autonomously based on the environment and other agents in the model. This is similar to the concept of classes in many Object-Oriented languages. The interactions among agents in many ABMs lead to emergent behaviors that can only be described at the system level. An example can be found in the flocking of birds in which the birds exhibit properties similar to those of self-governing organisms. As emergent behavior is difficult to study directly, in contrast to the individual behavior of a single agent, ABMs are well suited to analyzing these types of complex systems. In this method, the fundamental idea is the definition of a discrete heterogeneous state space in which the elements or agents have collective interactions with each other and change their states accordingly [1]. This thesis utilizes ABM to investigate two biological phenomena. A model is developed to simulate the emergence of resistant cancer cells as a result of chemotherapy. We also study viral dynamics in a population of cells, characterizing influenza and SARS-CoV-2 infections, and evaluating the antiviral Paxlovid.

1.1.1 Cancer model

Chemotherapy is a method of cancer treatment that uses anti-cancer drugs as a cure or to prolong the patient's life while reducing their symptoms [2, 3]. As a result of selective pressure, tumor cells evolve in a way similar to Darwin's theory of natural selection, resulting in the appearance of the most suitable clones [4, 5, 6, 7]. As a consequence of chemotherapy, the tumor population develops resistant descendants. Lamarckian induction [8] is another way of developing resistant cells, which involves changing the gene expression of a subpopulation of sensitive cells in order to acquire resistance. Recently, a third way in which resistance can be manifested has been revealed. It is known that resistance strongly depends on intercellular communication and on the tumor microenvironment [9, 10]. Using an ordinary differential equation, we developed a mathematical model to describe how tumor cells evolve into those that are susceptible to chemotherapy or those that are resistant to chemotherapy. The three mechanisms of emergence of chemotherapy resistance as a result of the therapeutic drug were considered in the model. This ODE model does not provide information regarding the spatial structure of a tumor due to the use of ordinary differential equations. Therefore, we have created a spatial version of this ODE model based on an agent-based model in order to assess the model's capability to describe tumor growth.

1.1.2 Viral dynamics

Various mathematical models have proved to be useful in the analysis of viral infections. These mathematical models are particularly useful in light of the current and virtually unprecedented pandemic, as they provide insights based on mathematic analysis and computer simulations. This means that they are able to obtain results at an ideally low cost even in complex situations where real-life and real-time experiments can either be extremely risky or simply impossible. The spatial-temporal nature of biological phenomena is ubiquitous, and we cannot afford to ignore such a critical aspect of our models. One obvious example is virus diffusion, which enables virus particles to physically reach susceptible cells. Our study emphasizes the importance of monitoring virus distribution in both space and time - we demonstrate that simpler models that ignore spatial phenomena lose their predictive precision due to the absence of spatial diffusion.

Chapter 2

Hybrid PDE-ABM system

2.1 Introduction

Agent-based modeling is another (and in fact quite different) approach to describe complex space-time dynamics in viral spread. The cornerstone idea of this method is to define a discrete heterogeneous state space where the so-called agents or elements have collective interactions with each other and they change their states correspondingly [1]. The ABM concept has several important applications within the field of virus dynamics, in [32] the authors apply an agent-based model to simulate influenza interactions at the host level.

An agent-based model is a great tool to include randomness and natural variability into the system, while PDEs are faster to evaluate numerically: by forming bridges between these two modeling strategies we arrive to a hybrid system, the so-called hybrid PDE-ABM model. This section introduces this hybrid system and compares it with other methods. In addition, we introduce the platform we use to implement our approach.

2.2 Comparison of the hybrid model with ODE, PDE, and Agent-based models

An equation-based model can be thought of as a continuum model that is based on a system of ordinary differential equations (ODEs) or partial differential equations (PDEs). A PDE captures both the temporal variation and spatial-related evolution of a system state variable, whereas an ODE captures only the temporal variation of said variable. The viral load titers produced by non-spatial models are generally higher than those produced by spatial models, and the peaks of infection occur significantly earlier [12, 13]. When the number of infected cells is large, homogenous recruitment of immune cells is comparable to the ODE model, but not when the

number of infected cells is small at the beginning of the infection [13]. Due to these differences, important parameters, such as viral infectivity [14], and basic reproductive ratio [14], can be estimated incorrectly. To determine the effectiveness of a therapeutic intervention, the basic reproductive ratio is required [14]. There has been a growing interest in models that incorporate spatial dispersion of infection within an individual host in recent years. Based on these models, it is assumed that only the free virus disperses into the environment, whereas the host cells do not (for example, [14, 15], and the references therein are cited). The spatial dispersion of viruses can be explained by such hybrid differential equation systems (that is, systems of two ordinary differential equations (ODEs) for the cells, and one parabolic partial differential equation (PDE) for the virus). As a class of modeling tools, ABMs are particularly suited to modeling heterogeneous populations and capturing the behavior of systems with intrinsic discrete properties, such as systems of cells [16]. Moreover, ABMs are effectively embedded in a system biology approach: the behavior of the system emerges from simulations of 1) the dynamics of individual agents (for example, cells), 2) the interactions between agents, and 3) the effects of the environment. ABMs, as compared to continuum models, offer a more natural description of cellular systems as they describe the processes that govern the activities of agents (e.g., mitosis, apoptosis [17]). Using this bottom-up approach, it is not necessary to have an in-depth knowledge of the entire system since its behavior will emerge naturally from the basic rules imposed on it. Compared to equation-based models, ABMs can incorporate stochasticity more easily, given that equation-based models are generally deterministic. Therefore, multiple runs of the same ABM produce heterogeneous results, which are consistent with actual observations of the phenomena, thereby bringing ABMs closer to reality. Finally, ABMs have the potential to capture spatially-related aspects more effectively, such as tissue heterogeneity, tissue composition and tissue morphology, allowing for the integration of phenomena occurring on different scales within multiscale frameworks [18]. A number of modeling strategies have been introduced above that can be used to simulate phenomena at various levels of resolution to reach a high level of accuracy. Due to the fact that biological processes involve a wide range of spatio-temporal scales, it is necessary to integrate these tools into the multiscale models of biological systems. Agents are capable of receiving inputs from the environment, influencing their decision-making, and also being able to alter the environment around them. Discrete and continuous models have many distinct characteristics, but hybrid models combine aspects of both types. There are hybrid ABMs that incorporate continuum models to describe various parts of the overall system, including the environment and a part of the agent's decision-making process, as well as the behavior of the agents [19, 22, 23, 24]. A hybrid ABM can also be classified as multi-scale if a section of the model, such as the continuum model, leads to behaviors that occur at a different spatiotemporal scale than the ABM itself.

To reconcile the exchange of information between these hybrid multi-scale ABMs, the continuum models are solved using conventional numerical methods on a faster time scale than the ABMs; synchronization between the scales is required so that the ABMs are able to resolve the information exchange [25]. It is true that there are many platforms that are supported for developing ABMs (e.g., NetLogo, Repast, Swarm, SPARK, CHASTE, MASON, and FLAME [19, 20, 21, 25, 26, 27, 28] , but we have found that the hybrid automata library (HAL) [29] platform (written using an object-oriented programming language, Java) provides the flexibility necessary for linking and solving hybrid multi-scale ABMs.

2.3 HAL's platform

Each of HAL's components can function independently in order to maintain its fundamental decentralized nature. Spatial queries can be used to combine any number of components into a single model (see Figure 2.3.1 which is adapted from [29]).

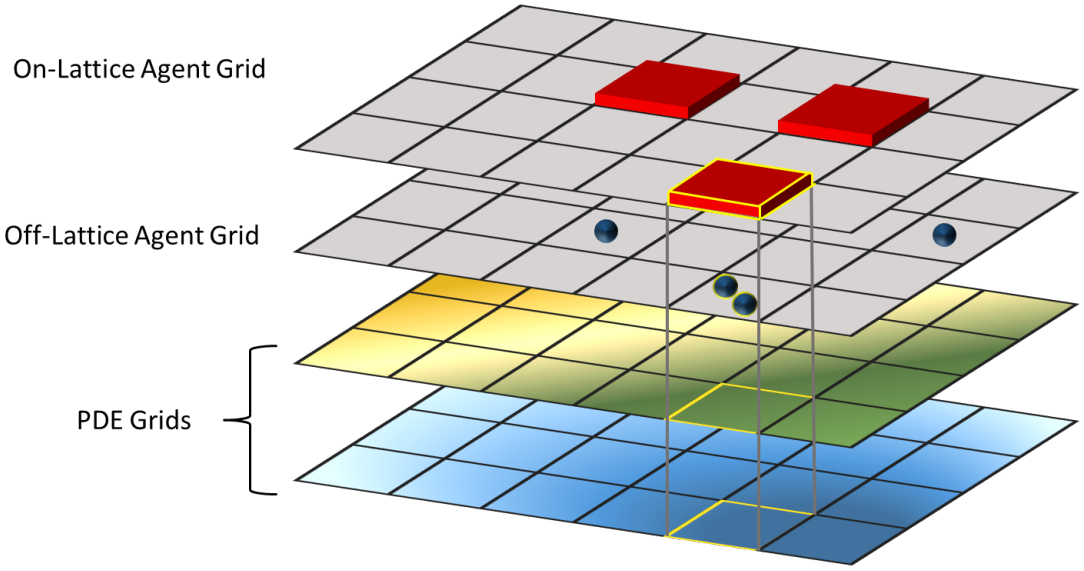

Figure 2.3.1: *A fundamental aspect of HAL's decentralized nature is the ability of its components to function independently. It is possible for the on-lattice agent to overlap with several other grids and PDEs (adapted from [29]).*

There are three ways in which stability can be achieved in a design:
First. Establishing safe interaction functions and preventing direct contact with internal components. Modelers, for example, are not permitted to alter the position properties of agents directly. Rather, they must call the provided movement functions which update the grid position of the agents as well for future spatial queries.
Second. Incorporating checks for invalid inputs into functions. As soon as one of

these problematic inputs is encountered, the program halts and displays an error message, such as inputting a diffusion rate constant that is unstable or moving two unstackable agents to the same location.
The third point. A series of small test programs are used to test HAL's algorithms. As a result of these tests, confidence in the algorithm implementation can be maintained. Three main areas are verified by unit tests: the accuracy of PDE algorithms, ABM aggregate behavior, and mathematical utilities. In addition, the PDEGrid functions were verified for convergence in time and space, as well as diffusion models using PopulationGrids [29].

Chapter 3

Cancer model

3.1 Introduction

Chemotherapy is a method for cancer treatment using anticancer drugs given as a curative agent or with the aim to prolong the patient's life and reduce the symptoms [2, 3]. During chemotherapy, a single drug or a combination of drugs is usually given at intervals in pulsed doses or cycles. Cytotoxic agents damage tumour cells, which may then lead to cell death, while application of cytostatic drugs suppress tumour growth without direct cytotoxic effect. Chemotherapy resistance – a major difficulty in cancer treatment – means that a tumour previously responsive to the therapy, begins to grow as cancer cells evolve the ability to prevent the development of an effective concentration of the active agent within them. Several ways can lead to resistance of tumour cells to chemotherapy. It has been shown that tumours evolve in a similar way as Darwinian evolution acts, i.e. tumour cells are affected by selective pressure which results in the emergence of the fittest clones [4, 5, 6, 7]. In case of chemotherapy, drugs operate as selective pressure agents. Under their effect, resistant descendant cells arise in the tumour cell population. Another way of development of resistant cells is Lamarckian induction [8], which means that a subpopulation of sensitive cells acquires resistance via changes in gene expression. A third way of appearance of resistance has recently been revealed. It is known that resistance strongly depends on intercellular communication and on tumour microenvironment. Information transfer among tumour and healthy cells affects both local and nonlocal interactions. The latter include long-range cell signalling, delivery of soluble factors and exchange of extracellular vesicles and they are responsible for the active modulation of tumour microenvironment. Microvesicles are extracellular particles released from the cell membrane transporting efflux membrane transporters, genetic information and transcription factors needed for their production in recipient cells. The important role played by microvesicles in the intercellular communication among cancer cells has been revealed by some recent studies [9, 10, 11, 30, 31, 33].

The way how microvesicles emitted by more aggressive donor cells are capable to transport cellular components to less aggressive acceptor cells resembles the transmission of infectious diseases.

In [34], the authors provided experimental evidence from in vitro assays to show that an important exogenous source of resistance is the action of chemotherapeutic agents. This action not only affects the signalling pathways but also the interactions among cells. The authors established a mathematical kinetic transport model consisting of a system of hyperbolic partial differential equations to describe the dynamics displayed by a system of non-small cell lung carcinoma cells exhibiting a complex interplay between Darwinian selection, Lamarckian induction and the nonlocal transfer of extracellular microvesicles. Here we consider a non-spatial version of that system, that allows us to perform a comprehensive mathematical analysis of its dynamics. Following establishing an ODE model to describe tumour growth and microvesicle transfer between cells, our next goal is to demonstrate that the ODE model is a reasonable approximation of the spatial phenomena (without, however, providing information regarding the spatial structure of the tumour). Thus, we use an agent-based model (ABM) to investigate a spatial extension of our ODE model.

3.2 ODE model

To formulate our model, let us denote by $S(t)$ the number of sensitive cells at time t and let $R(t)$ stand for the number of resistant cells. We denote by $c(t)$ the drug concentration in the patient's organism at time t. Let β denote the rate of microvesicle-mediated transfer from sensitive to resistant cells and θ is the cytotoxic action induced cell mortality of sensitive cells due to drugs. The notations ρ_0 and ρ_r stand for reproduction rates of sensitive and resistant cells, respectively, here we assume $\rho_0 > \rho_r$. Parameters μ_0 and μ_r denote death rates of sensitive and resistant cells, respectively, due to apoptosis. For the tumour growth, we assume a logistic form with carrying capacity K. The letter p stands for the rate of phenotype conversion due to Lamarckian induction. The notations α and ε stand for drug uptake rate of sensitive and resistant cells, respectively, while λ_0 denotes drug removal rate. The function $I(t)$ describes time-dependent drug dosage. With these notations, our model takes the form

$$\begin{aligned}
S'(t) &= -\beta(c(t))S(t)R(t) - \theta(c(t))S(t) + \rho_0 S(t)(K - S(t) - R(t)) - \mu_0 S(t) - p(c(t))S(t),\\
R'(t) &= \beta(c(t))S(t)R(t) + \rho_r R(t)(K - S(t) - R(t)) - \mu_r R(t) + p(c(t))S(t),\\
c'(t) &= -(\lambda_0 + \alpha S(t) + \varepsilon R(t))c(t) + I(t)
\end{aligned} \tag{3.2.1}$$

In the next section we make the simplifying assumption that the drug concentra-

tion $c(t)$ is constant, and investigate the case of changing drug concentration later. This assumption transforms (3.2.1) into the system

$$\begin{aligned} S'(t) &= -\beta S(t)R(t) - \theta S(t) + \rho_0 S(t)(K - S(t) - R(t)) - \mu_0 S(t) - pS(t), \\ R'(t) &= \beta S(t)R(t) + \rho_r R(t)(K - S(t) - R(t)) - \mu_r R(t) + pS(t). \end{aligned} \tag{3.2.2}$$

In Section 2, we will give a complete characterization of the global dynamics of system (3.2.2) depending on the parameters.

3.3 Description of the global dynamics

Let us define the following threshold parameters:

$$\begin{aligned} \mathcal{F}_1 &= K\rho_0 - p - \theta - \mu_0, \\ \mathcal{F}_2 &= K\rho_r - \mu_r, \\ \mathcal{F}_3 &= \mu_r(\beta + \rho_0) - (p + \theta + \mu_0 + K\beta)\rho_r. \end{aligned} \tag{3.3.1}$$

Proposition 3.3.1. *The sensitive cells die out whenever $\mathcal{F}_1 < 0$.*

Proof. We estimate $S'(t)$ as

$$S'(t) \leq S(t)(K\rho_0 - p - \theta - \mu_0 - p) = \mathcal{F}_1 S(t),$$

hence, if $\mathcal{F}_1 < 0$, then $S(t) \to 0$ as $t \to \infty$. □

Remark. It follows from Proposition 3.3.1 that no coexistence equilibrium can exist whenever $\mathcal{F}_1 < 0$.

Proposition 3.3.2.

1. *$\mathcal{F}_1 > 0$ and $\mathcal{F}_2 < 0$ imply $\mathcal{F}_3 > 0$.*
2. *$\mathcal{F}_1 < 0$ and $\mathcal{F}_2 > 0$ imply $\mathcal{F}_3 < 0$.*
3. *$\mathcal{D} < 0$ implies $\mathcal{F}_1 < 0$*

Proof. i) Suppose $\mathcal{F}_1 > 0$ and $\mathcal{F}_2 < 0$ hold but $\mathcal{F}_3 < 0$. Then we have $K\rho_0 > p + \theta + \mu_0$ and $K\rho_r < \mu_r$, hence, if $\mathcal{F}_3 < 0$ holds, then $\mu_r(\beta + \rho_0) < (p + \theta + \mu_0)\rho_r < K\rho_0\rho_r < \rho_0\mu_r$, which is a contradiction.

ii) This statement can be shown in an analogous way.

iii) In order to have $\mathcal{D} < 0$, the value $-4\beta p(\beta + \rho_0 - \rho_r)\mathcal{F}_1$ has to be positive, which can only happen is $\mathcal{F}_1 < 0$. □

The following simple statement concerning the existence of a coexistence equilibrium will be useful during the complete description of the global dynamics of system (3.2.2).

Proposition 3.3.3. *If $\mathcal{F}_1 > 0$ and $\mathcal{F}_3 < 0$ then there is no coexistence equilibrium.*

Proof. If $\mathcal{D} < 0$ then there is no coexistence equilibrium. Let us suppose that $\mathcal{D} > 0$. From Vieta's formulas, we obtain that if $\mathcal{F}_1 > 0$ and $\mathcal{F}_3 < 0$ then the equation $aR^2 + bR + c = 0$ has exactly one positive solution as $a > 0$ and $c/a < 0$. Similarly, the equation $\tilde{a}S^2 + \tilde{b}S + \tilde{c} = 0$ also has exactly one positive solution as $\tilde{a} > 0$ and $\tilde{c}/\tilde{a} < 0$. However, we now that for any coexistence equilibrium, the equality $\rho_0 S^* + R^*(\beta + \rho_0) = \mathcal{F}_1$ holds, hence, if R_1, R_2 and S_1, S_2 are the solutions of the two quadratic equations, then, in order to fulfil the previous equality, the S and R solutions corresponding to each other must have opposite signs. □

By linearizing (3.2.2) around the equilibria E_0 and E_R, respectively, and calculating the eigenvalues of the Jacobians of the linearized systems, we obtain the following results on the local stability properties of these two equilibria.

Proposition 3.3.4.

1. *E_0 is locally asymptotically stable if and only if $\mathcal{F}_1 < 0$ and $\mathcal{F}_2 < 0$.*
2. *E_R exists if and only if $\mathcal{F}_2 > 0$ and it is locally asymptotically stable if and only if $\mathcal{F}_2 > 0$ and $\mathcal{F}_3 < 0$.*

Theorem 3.3.5. *The global dynamics of equation* (3.2.2) *is completely determined by the threshold parameters $\mathcal{F}_1, \mathcal{F}_2, \mathcal{F}_3$ as follows.*

1. *If $\mathcal{F}_1 < 0$ and $\mathcal{F}_2 < 0$ then the only equilibrium E_0 is globally asymptotically stable.*
2. *If $\mathcal{F}_2 > 0$ and $\mathcal{F}_3 < 0$ then E_0 is unstable. The boundary equilibrium E_R is globally asymptotically stable. There is no coexistence equilibrium in this case.*
3. *If $\mathcal{F}_1 > 0$, $\mathcal{F}_2 < 0$ and $\mathcal{F}_3 > 0$ then E_0 is unstable. The coexistence equilibrium is globally asymptotically stable on $(\mathbb{R}_0^+)^2 \setminus X_S$. There is no boundary equilibrium and E_0 is globally asymptotically stable on X_S.*
4. *If $\mathcal{F}_1 > 0$, $\mathcal{F}_2 > 0$ and $\mathcal{F}_3 > 0$, then E_0 and E_R are unstable and the coexistence equilibrium E_C is globally asymptotically stable on $(\mathbb{R}_0^+)^2 \setminus X_S$. The boundary equilibrium E_R is globally asymptotically stable on X_S.*

The results of Theorem 3.3.5 are summarized in Table 3.3.1 where all possible combinations of the signs of the threshold parameters are listed along with the description of the existence and stability of the three possible equilibria. We note

Table 3.3.1: *Stability of equilibria depending on the threshold parameters.*

$\mathcal{F}_1$	$\mathcal{F}_2$	$\mathcal{F}_3$	E_0	E_R	E_C
$-$	$-$	$\pm$	GAS	$\times$	$\times$
$\pm$	$+$	$-$	unstable	GAS	$\times$
$+$	$-$	$+$	unstable	$\times$	GAS
$+$	$+$	$+$	unstable	unstable	GAS

that the remaining two combinations of signs cannot be realized: the combinations $\mathcal{F}_1 > 0, \mathcal{F}_2 < 0, \mathcal{F}_3 < 0$ and $\mathcal{F}_1 < 0, \mathcal{F}_2 > 0, \mathcal{F}_3 > 0$ are excluded by Proposition 3.3.2. The regions defined by the signs of the three threshold parameters $\mathcal{F}_1, \mathcal{F}_2, \mathcal{F}_3$ visualized in Figure 3.3.1. The '$+$' and '$-$' characters in the regions denote the signs of the parameters $\mathcal{F}_1, \mathcal{F}_2, \mathcal{F}_3$. The figure was prepared with $\beta = 0.0957$, $\rho_0 = 0.1$, $K = 0.538$, $\mu_0 = 0.01$, $\mu_r = 0.0262$ and $p = 0.01$, while the parameters θ and ρ_r are varied between 0 and 0.1. Using Theorem 3.3.5, one can identify which of the equilibria is globally asymptotically stable on the given region. That is, E_0 is globally asymptotically stable in the lower and middle regions on the right, E_R is globally asymptotically stable in the upper right and upper left regions, while E_C is globally asymptotically stable in the middle and lower regions on the left.

3.4 Stochastic individual-based spatial model

In the previous section, we established an ODE model to describe tumour growth and the transfer of microvesicles between cells which are spatial problems. Our next aim is to show that the ODE model provides a good overall approximation of the spatial phenomena (of course, without giving information about the spatial structure of the tumour). Hence, in this section, we use agent-based modeling (ABM) to investigate a spatial version of equation (3.2.2). We will compare this spatial model with the ODE model to assess how much information that model can provide in comparison with the spatial model. In order to simulate this ABM regarding to equation (3.2.2), we begin by defining the assumptions of the model and then describe the important technical aspects of the model in the implementation part. The following assumptions are considered for the ABM model.

1. There are two possible states for agents: we have sensitive or resistant cells.

2. If there is an empty space in the 8 cells Moore neighbourhood (Figure 3.4.1 (a)) of each cell, both sensitive and resistant cells divide with a probability of birth, P_b, which is equal to P_S or P_R, depending on the type of the given cell.

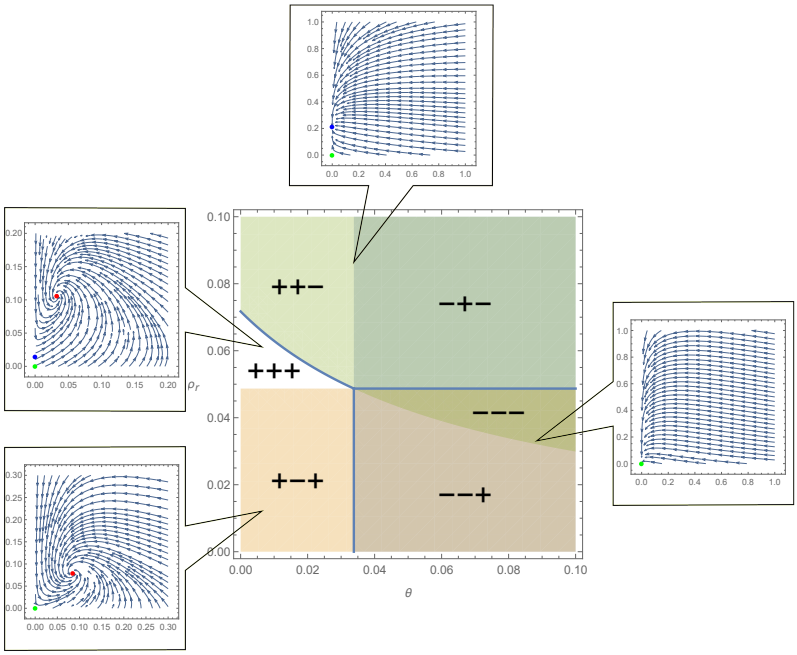

Figure 3.3.1: *Regions corresponding to the different combinations of the signs of the three threshold parameters* $\mathcal{F}_1, \mathcal{F}_2, \mathcal{F}_3$.

3. Sensitive cells die due to apoptosis with rate μ_S, and due to drug effect with rate θ_{ABM}. Resistant cells die due to apoptosis with rate μ_R. Let P_d denote the probability of death. Hence, in sensitive cells $P_d = \mu_S + \theta_{ABM}$ and in resistant cells $P_d = \mu_R$.

4. Phenotype conversion from sensitive to resistant cells can happen due to Lamarckian induction, the rate of which we denote by P_{ABM}. Another way of phenotype conversion is due to the transfer of microvesicles between cells. This phenomenon is described by two parameters, namely the distance from resistant cells (if there exists resistant cell(s) in the von Neumann neighbourhood of each sensitive cell) and the rate of phenotype conversion due to microvesicles is denoted by β_{ABM} in this model.

3.4.1 Computational implementation

In this subsection, we describe the important aspects of the ABM implementation. Numerical simulation of the ABM is implemented by using an open-source Java

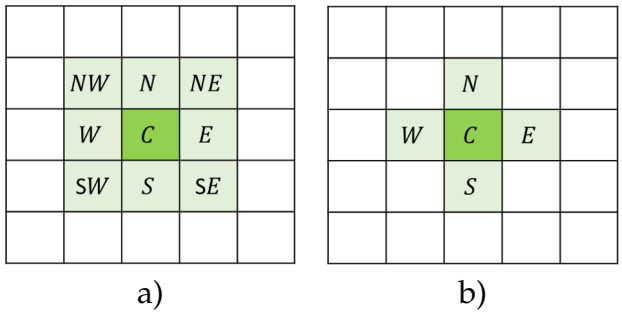

Figure 3.4.1: *a) Moore neighbourhood with radius* = 1 *b) von Neumann neighbourhood with radius* = 1.

library, Hybrid Automata Library (HAL) [29]. To execute the ABM model, we follow the scheme summarized in Figure 3.4.2 as a flow diagram of our spatial model. In this model, in order to consider the division and death probability, we compare them with a random number, r_1, which is generated for each cell in population at each time-step. If $r_1 < P_d$, the cell will die, but if $P_d < r_1 < P_d + P_b$, the Moore neighbourhood of the cell will be checked and if there is an empty space in the neighbourhood, the cell will create its daughter. Moreover, to take into consideration the phenotype conversion (*sensitive* $\rightarrow$ *resistant*) due to microvesicles, we check a von Neumann neighbourhood of each sensitive cell to see the spatial effect of microvesicles. The radius of this neighbourhood can be adjusted. If there exist resistant cells in the neighbourhood, for each of them, a random number, r_2, will be generated, and then we investigate $r_2 < \beta_{ABM}$ to check if due to at least one of the resistant cells in the neighbourhood, the conversion happens. Furthermore, there is another possibility for phenotype conversion (*sensitive* $\rightarrow$ *resistant*), due to Lamarckian induction in which case in each time loop sensitive cells convert to resistant ones with rate P_{ABM}. To take into account this conversion, we generate a random number, r_3, for each sensitive cell and if $r_3 < P_{ABM}$ this sensitive cell becomes a resistant.

3.5 Comparison of ABM and ODE model

3.5.1 Spatial model simulation

To simulate the ABM model, we start with a circle tumour (a von Neumann neighbourhood of the first tumour cell in the center of the domain) with a radius of 20 cells containing 1257 cells placed in the central domain such that 1% of them are resistant; these cells are randomly distributed among the remaining, sensitive cells. Furthermore, the domain consists of 200×200 square cells, so the total number of tumour cells cannot exceed 40000. The ABM model parameters are summarized

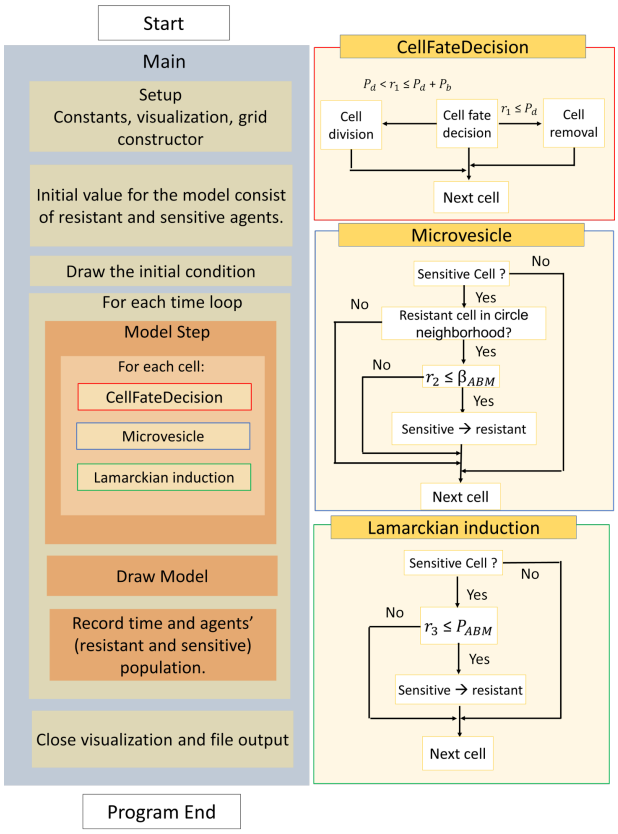

Figure 3.4.2: *ABM model flow diagram for equation* (3.2.2)

in Table 3.5.1. Figure 3.5.1 (a) shows the simulation of the ABM model considering the values in Table 3.5.1. In this figure, blue and green cells indicate sensitive and resistant cells, respectively. We can observe the coexistence of resistant and sensitive cells in Figure 3.5.1 (a). The number of both types of cells w.r.t. time in the same scenario is shown in Figure 3.5.2 (a). In order to study the sensitive cell mortality due to the drug, we increase θ from 0.03 to 0.12 while other parameters are fixed according to Table 3.5.1. This change leads to extinction which is demonstrated in Figure 3.5.1 (b), while the number of cells over time is plotted in Figure 3.5.2 (b). Finally, in Figure 3.5.1 (c) we depict the simulation of the ABM model with P_R increased from 0.01 to 0.1 while other parameters are fixed in Table 3.5.1. In this case, we can observe from Figure 3.5.1 (c) and Figure 3.5.2 (c) that after a while, resistant cells occupy the domain. Hence, we can observe three types of tumour destinies in the ABM model, all of which correspond to one of the scenarios described by the different regions shown in Figure 3.3.1.

Table 3.5.1: *Baseline parameters in the ABM model simulation.*

Symbol	Parameter	Value
P_{ABM}	Lamarckian induction	0.01
β_{ABM}	Rate of microvesicle-mediated transfer from sensitive to resistant cells	0.1
θ_{ABM}	Cell mortality of sensitive cells due to the drug	0.03
P_R	Probability of birth in resistant cells	0.01
P_S	Probability of birth in sensitive cells	0.2
μ_R	Probability of death in resistant cells	0.03
μ_S	Probability of death in sensitive cells	0.01
R_0	Initial value of resistant cells	12
S_0	Initial value of sensitive cells	1245

3.5.2 Comparison between ODE and stochastic agent-based model

We established the ABM model according to the corresponding ODE model (3.2.2). To compare the simulation results obtained from the agent based model and those from the ODE model (3.2.2), in Figure 3.5.5, we present solutions of (3.2.2) for various parameter sets. We note that although the same parameter values are used as for the agent based model, due to the differences in the role of the corresponding parameters of the two models, it is not possible to give a direct comparison of the results. However, the simulations can be applied to see that indeed, the outcomes of the simulations of the two models yield similar results. One can see that for both models, basically three different outcomes are possible: complete extinction of the tumour, a tumour with only resistant cells and a tumour with both sensitive and resistant cells. One can also observe that similar changes in the parameter values will yield equivalent changes in the outcomes of both models as shown by the examples presented in this section.

In spite of the equivalent qualitative results obtained from the two models, concerning the total amount of both types of cells, certainly there are quantitative differences between the two models. One of the most important of these is that in the ABM as a spatial model, we can adjust the radius of microvesicle transfer between cells, which is impossible to adjust directly in the ODE model as a non-spatial model. However, in part, it is present in the coefficient β in the ODE model as well. The main difference between the results yielded by the two models is that although we consider the effect of space in cancer cells in the ODE model, assuming parameters like β for microvesicles and K for carrying capacity, we cannot see the pattern of cell distribution in the space as we observe in the ABM model. This information about the cell pattern distribution enables us to know the growth process of the tumour,

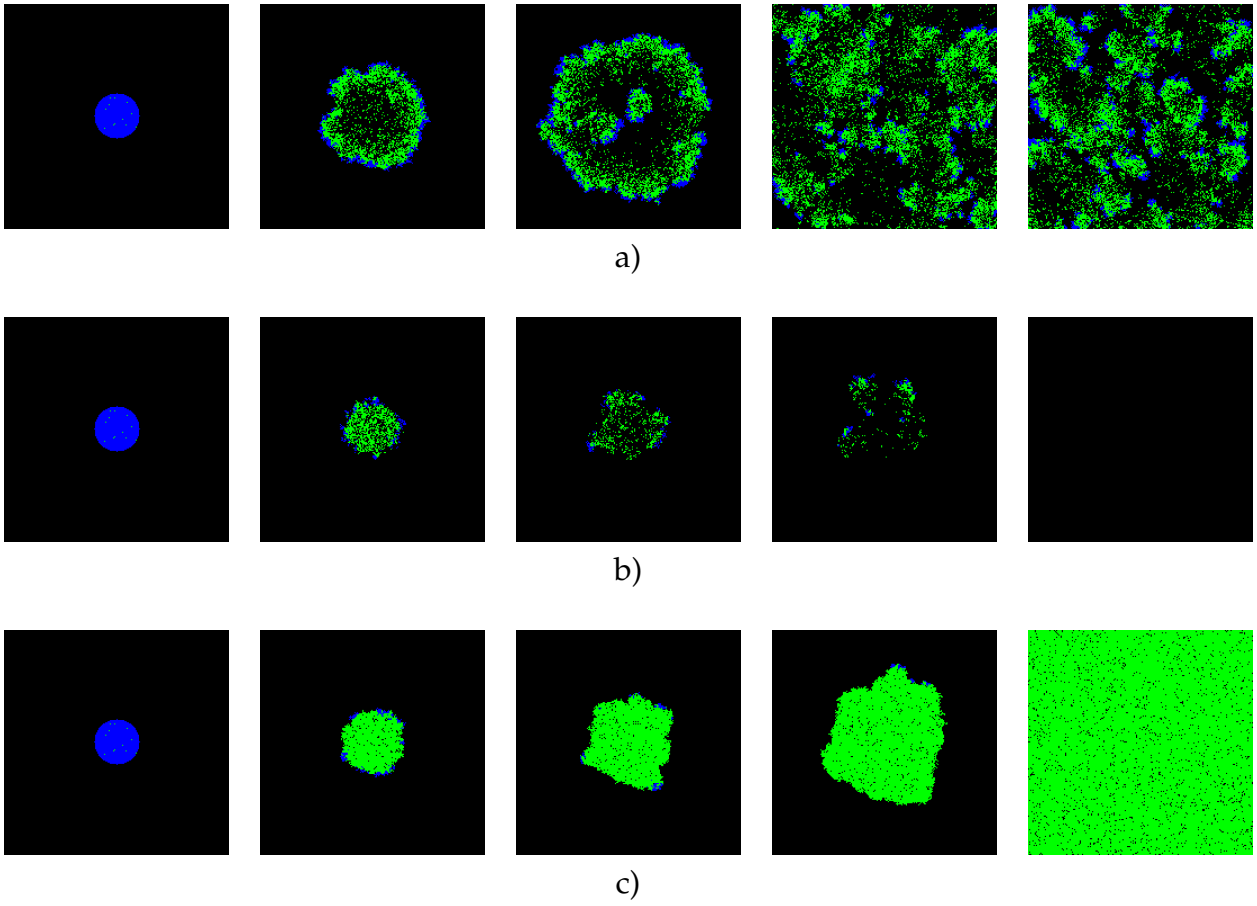

Figure 3.5.1: *ABM model simulation according to the different parameters leads to different scenarios in cells' pattern. Blue cells denote sensitive and green ones denote resistant cells. For all three simulations, all of the parameters in the ABM model are fixed as shown in Table 3.5.1. The only difference is in* ***b)*** $\theta = 0.12$, ***c)*** $P_R = 0.1$.

but the final outcome of tumour evolution is equivalent in both models. For instance, Figure 3.5.3 demonstrates the difference in cells pattern due to the differences in Lamarckian induction, P_{ABM}, and microvesicles effect, β. We assume all the ABM model parameters as given in Table 3.5.1, and we fix $P_S = 0.4$ for this simulation. The difference in parameters between these two simulations are in P_{ABM} and β that we assume $P_{ABM} = 0.08$ and $\beta = 0.0008$ in Figure 3.5.3(b) which is hundred times more in P_{ABM} and this amount less in β than our assumption for these parameters ($P_{ABM} = 0.0008$ and $\beta = 0.08$) in Figure 3.5.3(a). As seen, the cell growth procedure in these two simulations is different in the sense that the resistant cells are more randomly distributed in Figure 3.5.3(b) than in Figure 3.5.3(a). In contrast, in both simulations, the tumour evolves into a state of coexistence of resistant and sensitive cells with more resistant cells at the end, which is a quite similar destiny. Therefore, the ABM model provides more knowledge about the transient of cells development

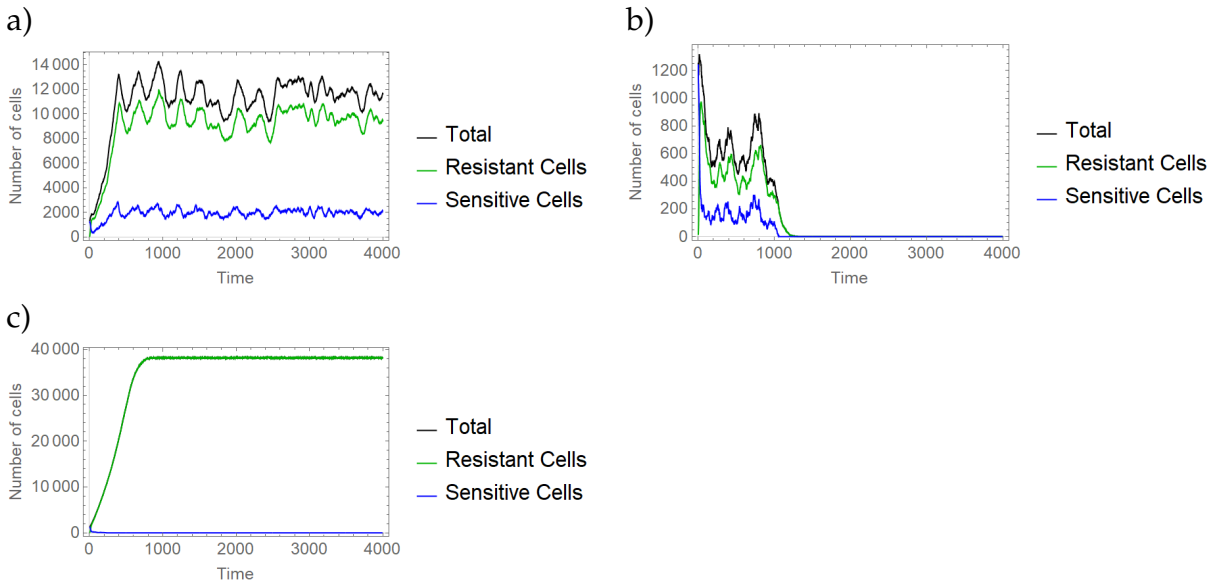

Figure 3.5.2: *The number of all tumour cells, sensitive and resistant cells in ABM model under three different parameters' values demonstrated in Figure 3.5.1.* ***a)*** *is the simulation with parameters' values in Table 3.5.1,* ***b)*** *is the same simulation like* ***a*** *considering higher value for rate of cell mortality of sensitive cells due to the drug,* $\theta = 0.12$*,* ***c)*** *is also the same simulation like* ***a*** *with higher value for probability of birth in resistant cells,* $P_R = 0.1$*.*

in cancer than the ODE model while it needs more computational load.

3.6 Discussion

We established a mathematical model describing the evolution of tumour cells sensitive or resistant to chemotherapy. In the model, we considered three ways of emergence of chemotherapy resistance as a result of the therapeutic drug: Darwinian selection, Lamarckian induction and, based on recent discoveries, the emergence of resistance via the transfer of microvesicles from resistant to sensitive cells, which happens in a similar way as the spread of an infectious agent.
Our simple ODE model (3.2.2) certainly has its limitations. As we use ordinary differential equations, our model cannot provide information about the spatial structure of a tumour.To assess the capabilities of our model in describing tumour growth, we have also established a spatial version of the model in the form of an agent based model. Comparing the two models, we can deduce that the ODE model performs well in reproducing the possible outcomes of the tumour growth: as for total mass of the two cell types, there is no further scenario provided by the ABM than the ones experienced with the ODE model. Of course, this model will only give us information about the tumour mass and not about the spatial distribution of the

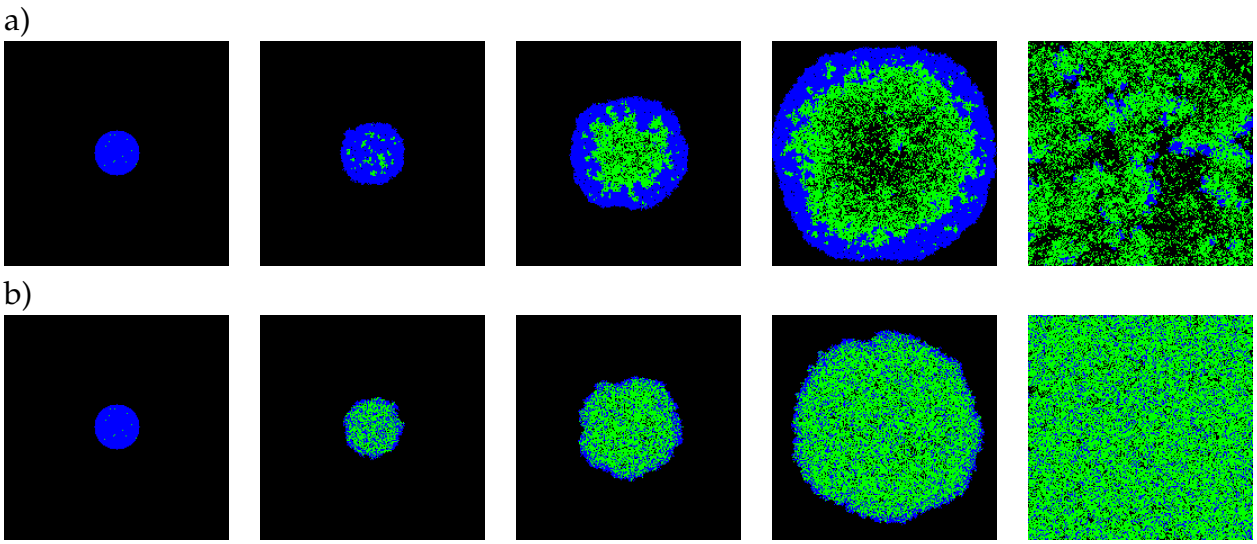

Figure 3.5.3: *Two different scenarios of cell growth considering the effect of microvesicles and Lamarckian induction. Parameters in the ABM model are as shown in Table 3.5.1 and* $P_S = 0.4$*. The difference between the two simulations is in* ***a)*** $\beta = 0.08$ *and* $p = 0.0008$ *and in* ***b)*** $\beta = 0.0008$ *and* $p = 0.08$*.*

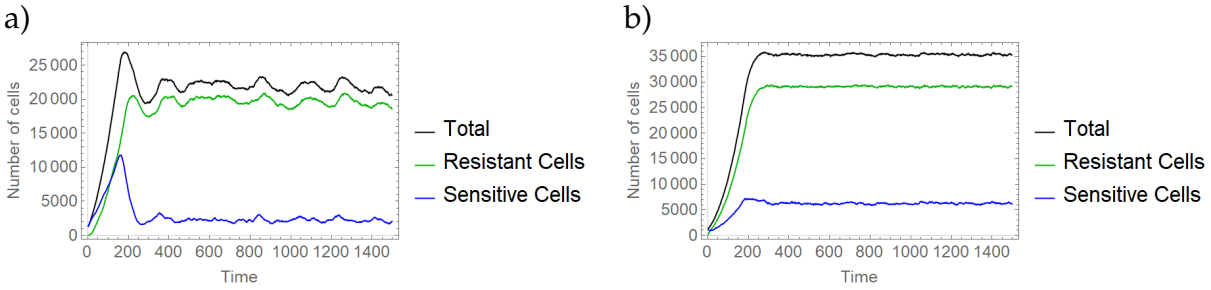

Figure 3.5.4: *The number of tumour cells including sensitive and resistant cells in ABM model under two different parameters' values demonstrated in Figure 3.5.3.* ***a)*** $P_S = 0.4$*,* $\beta = 0.08$ *and* $p = 0.0008$*,* ***b)*** $P_S = 0.4$*,* $\beta = 0.0008$ *and* $p = 0.08$*.*

two types of the tumour cells or the direction of spatial growth of the tumour. Also, the simulations suggest that the ODE model and the agent based model react in a similar way to parameter changes. Furthermore, the ODE model cannot describe the transfer of microvesicles as a spatial phenomenon in a way the ABM is capable to do so, although by modifying the parameter β in the ODE, in some extent we also consider the effect of distance between cells on the transfer of microvesicles.
In its present form, the effect of microvesicles and Lamarckian induction is described in a simple way in our model, especially in the simplified form (3.2.2). To consider these phenomena in a more realistic way can be subject of future research.

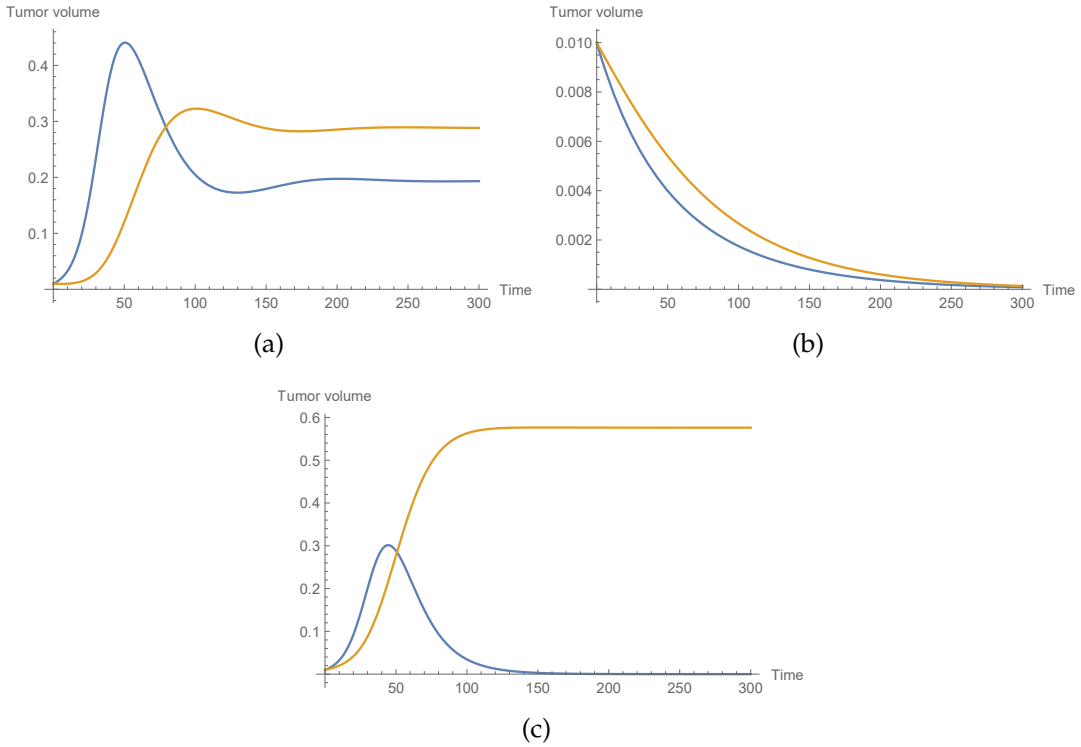

Figure 3.5.5: *The number of sensitive and resistant cells in solutions of model* (3.2.2) *with three different parameter sets. Figure* ***a)*** *shows solutions with parameter values in Table 3.5.1, in Figure* ***b)*** *a higher value is applied for the rate of cell mortality of sensitive cells due to the drug,* $\theta = 0.17$*, while in Figure* ***c)*** *we apply a higher value for the birth rate of resistant cells,* $\rho_r = 0.1$*. Blue curves denote sensitive, orange curves denote resistant cells.*

Chapter 4

Viral dynamics for SARS-COV-2 and influenza

4.1 Introduction

Mathematical models have been powerful tools in tackling the challenges posed by the appearance of the COVID-19 disease caused by the novel SARS-CoV-2 coronavirus. In the ongoing and virtually unprecedented pandemic these mathematical models are invaluable as they are able to provide insights or predictions based on mathematical analysis and computer simulations. This means that their results are obtained at an ideally low cost even in complex situations where real-life and real-time experiments to obtain these same results would be either extremely risky or simply not possible. There is a large variety of both large,- and small-scale mathematical models related to COVID-19, the present article is dedicated to cellular level investigations – we examine virus dynamical phenomena such as in-host viral transmission between individual cells. Specifically, we use a hybrid mathematical approach for our study, focusing on SARS-CoV-2 and influenza infections.

Throughout the investigation of the above mentioned hybrid model we need a simple and already comprehensively understood model we can use as a reference system – for this purpose we will consider a specific version of an ODE prototype model, the May-Nowak system (for an extensive overview see [41]; while for a concrete application we refer to [42]). This classical model is given by

$$\begin{cases} H_t = -\beta HV, & t > 0, \\ I_t = \beta HV - \delta I, & t > 0, \\ V_t = pI - cV, & t > 0, \end{cases}$$

where the $H = H(t), I = I(t)$ and $V = V(t)$ functions respectively correspond to the number of healthy cells, infected cells and virus particles, and they depend on

time only. This model plays a crucial part in our article in several ways: *a)* in the development process of the more sophisticated hybrid model we use the ODE model to compare and match the respective solutions, *b)* we exploit the fact that there is more information available on the exact parameters of this classical model and use their converted version in the hybrid system, and finally, *c)* we can demonstrate both the advantages and challenges offered by the relatively new hybrid system in comparison to a well-known model.

The above ODE model is widely used to describe in-host viral dynamics. While this method proves to be extremely useful, the quality of information it can provide is naturally limited since it uses time as its single independent variable, and cannot capture spatial effects. Spatiotemporal phenomena are ubiquitous in biological applications, and often we simply cannot afford to leave out such an important factor from our models: the most obvious example for this is virus diffusion itself, which makes it possible for viruses to physically reach susceptible cells. One of the most powerful tools that does capture these crucial spatial mechanisms is the rich analytical theory of partial differential equations – PDE models are often used to investigate complex systems in viral infection dynamics, see [43] just to mention one SARS-CoV-2-related example.

Agent-based modeling is another (and in fact quite different) approach to describe complex space-time dynamics in viral spread. The cornerstone idea of this method is to define a discrete heterogeneous state space where the so-called agents or elements have collective interactions with each other and they change their states correspondingly [1]. The ABM concept has several important applications within the field of virus dynamics, in [32] the authors apply an agent-based model to simulate influenza interactions at the host level.

As seen above, different frameworks – including agent-based models and PDE systems – have been applied to construct viral dynamics models. An agent-based model is a great tool to include randomness and natural variability into the system, while PDEs are faster to evaluate numerically: by forming bridges between these two modeling strategies we arrive to a hybrid system, the so-called hybrid PDE-ABM model, which unites the different advantages of these methods (see [44]). For the purpose of investigating the in-host viral spread of SARS-CoV-2 and influenza, our hybrid model is chosen and tailored by carefully considering certain dimension-related aspects of the problem: virus particles are several magnitude smaller than epithelial cells ([45], [46], [47]), and as a consequence, it is natural to capture virus concentration by a continuous function, while cells are modeled in a straightforward way as discrete entities in space. In other words, we obtain our hybrid model by merging a) a PDE representing virus concentration, and b) an agent-based model describing host cells and their three possible states (healthy, infected, and dead). We complete the hybrid PDE-ABM model by formulating a meaningful connection

between the separate parts, i.e. by giving definition to all the considerable interactions and feedback processes that take place between the model's discrete and continuous parts, such as for example cells responding to their environment's virus concentration level. We highlight that our implementation of the proposed hybrid system is based on a free and open source software package, HAL (Hybrid Automata Library) [29].

The novelty of this chapter consists both in its approach and results. While PDE-ABM hybrid models have existed before HAL [29], the latter is primarily focused to serve cancer-related research – we have adapted, configured, and applied this tool to allow investigations in a completely different field of application: host-level virus infections. Our methodology and results demonstrate that both our model and its implementation technique provide a suitable framework to investigate problems in virology and immunology. We emphasise the importance of monitoring virus propagation in both space and time – we show that simpler models that disregard spatial phenomena correspondingly lose predictive precision due to ignoring spatial diffusion. The numerical simulations we perform using the hybrid system as a foundation give spatially explicit information regarding cellular-level virus spread for SARS-CoV-2 in a high-resolution state space, which is one of the main achievements of our article. The successful, computer-simulated replication of real *in vitro* experiments regarding SARS-CoV-2 propagation is also new to our knowledge. Finally, we highlight that our results allow us to gain insight into why the respective outcomes of influenza and SARS-CoV-2 infections are different.

4.2 Mathematical framework

The purpose of this section is to give a detailed description of the two main systems we use to model virus spread. We begin by defining the hybrid PDE–ABM model and introducing its variables, then we briefly outline a classical ODE model – the latter can be viewed as a simpler mean-field model that approximates the more complex hybrid framework by averaging over spatial variables. Once all the fundamental features of both systems are defined, we continue this section by expressing the connection between the corresponding model parameters, and conclude with the numerical implementation of the hybrid system.

4.2.1 The hybrid PDE–ABM model

As described in the Introduction, the main hybrid system is constructed via forming bridges between two important and rather different modeling techniques: we merge a discrete agent based model and a continuous PDE, and we create a meaningful connection between them by carefully designing their interactions with

each other. We highlight the fact the model we obtain this way is defined in both space and time.

We begin by setting the notation for the domain we construct our model upon: let Ω be the mathematical representation of the part of lung tissue, or in the case of an *in vitro* experiment, the relevant area of the investigation we are considering. Now we are ready to introduce the discrete part of our hybrid system.

One of the most important modeling decisions in the first part of the model construction is approaching epithelial cells as discrete agents. In more detail, we define a two dimensional ABM state space by introducing a lattice of $k_1 \times k_2$ agents representing epithelial cells: naturally, $k_1, k_2 \in \mathbb{N}$, and cells are identified via the (i, j) indices (corresponding to the respective agent's place in the grid), where $(i, j) \in \mathcal{J} = \{(i, j) | 1 \leq i \leq k_1, 1 \leq j \leq k_2\}$. By introducing the $\Omega_{i,j}$ notation for the open set occupied by the (i, j)-th cell, we obtain that $\bar{\Omega} = \bigcup_{(i,j)\in\mathcal{J}} \bar{\Omega}_{i,j}$.

Regarding the states of the ABM space's agents, each agent can have three possible states in our approach. This is formally grasped by following state function, which represents the concept that a cell is either *healthy*, *infected*, or *dead*:

$$s_{i,j}(t) = \begin{cases} \text{H}, & \text{if the } (i,j)\text{-th cell is healthy at time } t \\ \text{I}, & \text{if the } (i,j)\text{-th cell is infected at time } t \\ \text{D}, & \text{if the } (i,j)\text{-th cell is dead at time } t. \end{cases}$$

In terms of state dynamics, we use the following assumptions:

- for simplicity, we do not account for cell division or cell birth taking place during the time frame of the infection;
- the only reason for cell death is viral infection itself, i.e. death related to any other natural cause is ignored;
- all healthy cells are susceptible target cells;
- once a cell gets infected, it is not possible for it to become healthy again;
- the *healthy* $\rightarrow$ *infected* state change: a healthy cell may become infected once the virus has reached the given cell; moreover, infection is randomized and it occurs with a probability of P_I, where we highlight that P_I increases linearly with the virus concentration in the given cell (for more details see Section 4.2.3 on P_I's relationship to other parameters and Section 4.2.4 on implementation);
- the *infected* $\rightarrow$ *dead* state change: an infected cell dies with a probability of P_D, but similarly to infection, death too is approached from a stochastic viewpoint.

The stochastic element in the above state changes is of key importance. The inclusion of natural randomness makes the complex PDE-ABM hybrid model not only more realistic than the relatively simple ODE model, but also compared to a pure PDE system.

We note that apart from following the state changes of all cells on an individual level, we also introduce three additional system variables as functions taking discrete (in fact, natural) values: $H(t)$, $I(t)$ and $D(t)$ respectively denote the total number of healthy, infected, and dead cells in the two-dimensional ABM state space.

Now we are ready to consider the second part of our hybrid model. Let us begin by observing that the size of an epithelial cell is relatively significant ([46], [47]) and hence indeed it was a natural idea above to define cells as separate entities and follow their states on an individual level (instead of exclusively considering the total number of healthy, infected and dead cells as continuous functions for example). One of the cornerstone observations in the second part of the model is that viruses, on the other hand, are several magnitude smaller compared to epithelial cells [45] – we incorporate this simple but crucial biological fact into our system by modeling virus concentration as a continuous function. Hence, in the second part of the model we approach virus concentration $V^h = V^h(t,x,y)$ as a variable that is continuous in both space and time, and as such, we capture it by means of a partial differential equation:

$$\frac{\partial V^h(t,x,y)}{\partial t} = D_V \Delta V^h - \mu_V \cdot V^h(t,x,y) + \sum_{(i,j)\in\mathcal{J}} g_{i,j}(t,x,y), \quad t>0,\ (x,y)\in\Omega, \tag{4.2.1}$$

where D_V denotes the virus diffusion coefficient, μ_V is a constant ratio representing virus removal, while $g_{i,j}$ stands for the viral source term (the latter is assumed to be continuous) for the (i,j)-th cell. The above equation essentially grasps the basic concept that viruses spread across the domain primarily via diffusion (convective flows are ignored in this model), the immune system removes viruses in a constant ratio, while new virus particles are generated by infected cells in a process described by the $g_{i,j}$ functions:

$$g_{i,j}(t,x,y) = \begin{cases} 0, & \text{if } s_{i,j}(t) = \text{H and } (x,y)\in\Omega_{i,j} \\ f_{i,j}(t,x,y), & \text{if } s_{i,j}(t) = \text{I and } (x,y)\in\Omega_{i,j} \\ 0, & \text{if } s_{i,j}(t) = \text{D and } (x,y)\in\Omega_{i,j} \\ 0 & \text{if } (x,y)\notin\Omega_{i,j} \end{cases} \tag{4.2.2}$$

We point out that in the above formula we do not specify any particular exact $f_{i,j}(t,x,y)$ form for the viral source term $g_{i,j}(t,x,y)$ for the case when $s_{i,j}(t) = \text{I}$ and $(x,y)\in\Omega_{i,j}$ (i.e. when the (i,j)-th cell is infected). As noted in [48], very little is known about the shape, duration and magnitude of viral burst, and hence, we allow

any reasonable and smooth $f_{i,j}(t,x,y)$ function here that meets the following two criteria. Firstly, any concrete choice for $g_{i,j}$ needs to represent the general fact the (i,j)-th epithelial cell starts secreting virions at some point after it becomes infected. Thus, naturally, $g_{i,j}$ takes positive values at least in some subset of $\Omega_{i,j}$ at some point after the event of infection (but of course, as formulated above, outside of this given cell $g_{i,j}$ is zero). Secondly, the $g_{i,j}$ function needs to be defined in a way so that the well-posedness of system (4.2.1) is guaranteed: specifically, any concrete definition of the viral source term has to be Hölder continuous with Hölder exponent $\alpha \in (0,1)$, i.e. we assume $g_{i,j}(t,x,y) \in C^{\frac{\alpha}{2},\alpha}((0,\infty)\times\bar{\Omega})$ for any $t>0$,$(x,y)\in\bar{\Omega}$ and any $(i,j)\in\mathcal{J}$. The latter ensures the global existence of system (4.2.1)'s solution (see Appendix B). As an example, we can consider a definition where we use the mollified version of a constant rate release within the (i,j)-th cell. As for the details and changes related to the construction of $g_{i,j}$ in the implementation process, see Section 4.2.4.

The PDE-ABM hybrid model cannot be complete without explicitly taking into account the meaningful interactions that each part-system has on the other, hence we briefly highlight these connections again. The continuous viral part affects the agent-based subsystem through the *healthy* $\rightarrow$ *infected* state change described in the ABM section above. On the other hand, the discrete ABM part makes a difference within the continuous viral equation thanks to the $g_{i,j}$ source functions (representing the fact that once a cell gets infected, at some point it starts spreading the virus).

4.2.1.1 The well-posedness and ultimate boundedness of the PDE model

In this subsection, we shall establish the global existence and ultimate boundedness of the virus concentration function described by equation (4.2.1). We make the following suitable assumption:

$$(\mathbf{H_1}): g_{i,j}(t,x,y) \in C^{\frac{\alpha}{2},\alpha}([0,\infty)\times\bar{\Omega}) \cap L^{\infty}((0,\infty)\times\Omega)$$
$$\text{is nonnegative for each } (i,j)\in\mathcal{J} \text{ and } \alpha\in(0,1).$$

Theorem A.1 (Well-posedness and ultimate boundedness) Let $\Omega\subset\mathbb{R}^2$ be a bounded domain with smooth boundary. Suppose that the parameters D_V, μ_V are positive. Then for a non-negative initial value function $V_0^h(x,y)\in C^0(\bar{\Omega})$ system (4.2.1) has a unique non-negative global solution $V^h(t,x,y)$ defined on $[0,\infty)\times\bar{\Omega}$. Moreover, the solution $V^h(t,x,y)$ is ultimately bounded and satisfies $\limsup_{t\to\infty}\max_{\bar{\Omega}} V^h(t,x,y) \le \frac{B}{\mu_V}$, where B is defined in (4.2.3).

Proof. We use the lower-upper solution method for our proof. According to $(\mathbf{H_1})$, we define

$$\Big\| \sum_{(i,j)\in\mathcal{J}} g_{i,j}(t,x,y) \Big\|_{L^{\infty}((0,\infty)\times\Omega)} := B. \tag{4.2.3}$$

Let $\overline{V}(t,x,y) = \big(\sup_{\bar{\Omega}} V_0^h(x,y) - \frac{B}{\mu_V}\big)e^{-\mu_V t} + \frac{B}{\mu_V} := V^\star(t)$ and $\underline{V}(t,x,y) = 0$. Since

$$\begin{aligned}&\frac{\partial \overline{V}(t,x,y)}{\partial t} - D_V \Delta \overline{V}(t,x,y) + \mu_V \overline{V}(t,x,y) - \sum_{(i,j)\in\mathcal{J}} g_{i,j}(t,x,y)\\ &\geq \frac{dV^\star(t)}{dt} + \mu_V V^\star(t) - B = 0\end{aligned} \tag{4.2.4}$$

and

$$\begin{aligned}&\frac{\partial \underline{V}(t,x,y)}{\partial t} - D_V \Delta \underline{V}(t,x,y) + \mu_V \underline{V}(t,x,y) - \sum_{(i,j)\in\mathcal{J}} g_{i,j}(t,x,y)\\ &= -\sum_{(i,j)\in\mathcal{J}} g_{i,j}(t,x,y) \leq 0.\end{aligned} \tag{4.2.5}$$

Clearly the boundary condition satisfies $\frac{\partial \overline{V}}{\partial \nu} = 0 \geq 0 = \frac{\partial \underline{V}}{\partial \nu}$ and the initial condition satisfies $\overline{V}(0,x,y) = \sup_{\bar{\Omega}} V_0^h(x,y) \geq 0 = \underline{V}(0,x,y)$. Thus $(\overline{V}(t,x,y), \underline{V}(t,x,y))$ is a pair of coupled upper solution and lower solution of system (4.2.1). From $(\mathbf{H_1})$, we get that the function $f(t,x,y,V^h) = -\mu_V V^h + \sum_{(i,j)\in\mathcal{J}} g_{i,j}(t,x,y)$ is Hölder continuous with exponent α with respect to t and x,y on $\bar{Q}_T \times [m,M]$, and $f_{V^h}(t,x,y,V^h) = -\mu_V \in C(\bar{Q}_T \times [m,M])$, where $Q_T = (0,T] \times \Omega$, $m = \min_{\bar{Q}_T} \underline{V}(t,x,y)$ and $M = \max_{\bar{Q}_T} \overline{V}(t,x,y)$. In view of [56, Theorem 2.4.6], system (4.2.1) has a unique solution defined on $(0,T] \times \Omega$ satisfying

$$0 \leq V^h(t,x,y) \leq V^\star(t). \tag{4.2.6}$$

By the arbitrariness of T, the solution of system (4.2.1) exists globally in time. Clearly, from the definition of $V^\star(t)$, we know that $V^\star(t) \leq \max\{\frac{B}{\mu_V}, \sup_{\bar{\Omega}} V_0^h(x,y)\}$. Then it follows from (4.2.6) that $\limsup_{t\to\infty} \max_{\bar{\Omega}} V^h(t,x,y) \leq \frac{B}{\mu_V}$, which ends the proof of the theorem. □

In fact, since $\sum_{(i,j)\in\mathcal{J}} g_{i,j}(t,x,y) \in C^{\frac{\alpha}{2},\alpha}([0,\infty)\times\bar{\Omega})$, it follows from the regularity theory of parabolic equation that system (4.2.1) has a unique classical solution $V^h(t,x,y) \in C^{1+\frac{\alpha}{2},2+\alpha}([0,\infty)\times\bar{\Omega})$. Here the lower-upper solution method is mainly employed to estimate the upper bound of virus particles in the whole spatial domain Ω as time evolves.

4.2.2 The ODE model

In this subsection we consider a simpler viral dynamics system which will serve as a reference model for the hybrid framework in our epidemiological investigations. We consider the following – only time-dependent – ODE system:

$$\begin{cases} \frac{dH(t)}{dt} = -\beta H(t)V(t), & t > 0, \\ \frac{dI(t)}{dt} = \beta H(t)V(t) - \delta I(t), & t > 0, \\ \frac{dV(t)}{dt} = pI(t) - cV(t), & t > 0, \\ \frac{dD(t)}{dt} = \delta I(t), & t > 0, \\ H(0) = H_0 \geq 0, I(0) = I_0 \geq 0, V(0) = V_0 \geq 0, D(0) = D_0 \geq 0, \end{cases} \tag{4.2.7}$$

where the $H(t), I(t), V(t), D(t)$ functions represent the number of healthy cells, the number of productively infected cells, the number of viruses released by infected cells and the dead cells at time t, respectively; β denotes the healthy cells' infection rate, δ stands for the death rate of infected cells, p is the virus production rate, and c is the virus removal rate. We emphasise the fact that unlike the hybrid PDE-ABM model, the above ODE system is not defined in space.

Technically, the $V(t)$ function can be defined to represent either the number of viruses or the virus concentration itself depending on the specific application we are considering. In Section 4.3's simulation results $V(t)$ stands for concentration.

Simply because of the physical meaning behind these functions, the respective initial values are naturally set in the region $\Gamma = \{(u_1, u_2, u_3, u_4) \in \mathbb{R}^4 : u_1, u_2, u_3, u_4 \geq 0\}$. For the well-posedness and boundedness of model (4.2.7) see Appendix C.

The basic reproduction number of system (4.2.7) is given by

$$\mathcal{R}_0 = \frac{p\beta H_0}{c\delta}, \tag{4.2.8}$$

for the derivation of this number and how it governs the threshold dynamics of the system, see Appendix D.

4.2.2.1 The well-posedness and boundedness of the ODE model

Theorem A.2 Let's suppose $(H_0, I_0, V_0, D_0) \in \Gamma$ for our initial data. Then system (4.2.7) has a unique solution $(H, I, V, D) \in \Gamma$, i.e. Γ is positively invariant.

Furthermore, the solution of system (4.2.7) satisfies

$$\begin{aligned} &0 \le H(t) \le H_0, \quad 0 \le \limsup_{t\to\infty} V(t) \le \frac{p(N-V_0)}{c}, \\ &0 \le \limsup_{t\to\infty} I(t) \le (N-V_0)\min\{1, \frac{p\beta H_0}{c\delta}\}, \ 0 \le D(t) \le N - V_0. \end{aligned} \tag{4.2.9}$$

where $N = H_0 + I_0 + V_0 + D_0$.

Proof. **Existence and Uniqueness.** By the continuity of right side of Eq. (4.2.7), system (4.2.7) has at least one solution in $[0, b)$ with $0 < b \le \infty$. Since the term on the right-hand side of system (4.2.7) satisfies the local Lipschitz property with respect to H, I, V, D in Γ, the uniqueness of solutions follows from the standard theory of ordinary differential equations.
Positive Invariance and Boundedness. For $H \ge 0, I \ge 0, V \ge 0, D \ge 0$, since

$$\begin{aligned} &\dot{H}(t)\big|_{H=0} = 0 \ge 0, \quad \dot{I}(t)\big|_{I=0} = \beta HV \ge 0, \\ &\dot{V}(t)\big|_{V=0} = pI \ge 0, \quad \dot{D}(t)\big|_{D=0} = \delta I \ge 0, \end{aligned} \tag{4.2.10}$$

it follows from [55, Theorem 5.2.1] that the solution $(H(t), I(t), V(t), D(t))$ of system (4.2.7) is nonnegative for all $t \ge 0$ whenever $H_0 \ge 0, I_0 \ge 0, V_0 \ge 0, D_0 \ge 0$. Therefore Γ is positively invariant with respect to system (4.2.7).

Since $\dot{H}(t) = -\beta H(t)V(t) \le 0$, we get $0 \le H(t) \le H_0$. Also from system (4.2.7), we obtain

$$\frac{d(H(t) + I(t) + D(t))}{dt} = 0 \quad \Rightarrow H(t) + I(t) + D(t) = N - V_0. \tag{4.2.11}$$

As $H(t) \ge 0, D(t) \ge 0$, we get $I(t) \le N - V_0$. From the third equation of system (4.2.7), we have

$$\frac{dV(t)}{dt} \le p(N - V_0) - cV,$$

which implies that

$$\limsup_{t\to\infty} V(t) \le \frac{p(N-V_0)}{c}. \tag{4.2.12}$$

From (4.2.12), we know that for any $\varepsilon > 0$ there exists $T(\varepsilon) > 0$, s.t. when $t \ge T(\varepsilon)$, $V(t) \le \frac{p(N-V_0)}{c} + \varepsilon$. Thus

$$\frac{dI(t)}{dt} \le \beta H_0(\frac{p(N-V_0)}{c} + \varepsilon) - \delta I.$$

By the comparison principle of ordinary differential equations, we get

$$\limsup_{t\to\infty} I(t) \leq \frac{p\beta H_0(N-V_0)}{c\delta}. \tag{4.2.13}$$

Since $I(t) \leq N - V_0$, we get $\limsup_{t\to\infty} I(t) \leq (N-V_0)\min\{1, \frac{p\beta H_0}{c\delta}\}$. This completes the proof. □

4.2.2.2 The threshold dynamics of the ODE model

The basic reproduction number $\mathcal{R}_0$ can be deduced by simple reasoning: a single infected cell produces virus with rate p during its expected lifetime $1/\delta$, summing up to p/δ viruses. Virus particles generate infected cells (in a healthy cell population) with rate βH_0, in an expected time period $1/c$. Overall we find the number of new infected cells originated from the initial cell as given in (4.2.8). For a more formal derivation, one can also use the next generation approach [58].

Theorem A.3 If $\mathcal{R}_0 > 1$, then the disease-free equilibrium of the form $e_* = (H_0, 0, 0, D_s)$ is unstable, where $H_0 > 0$, D_s being an arbitrary nonnegative constant. This means an infection can be established. Furthermore, system (4.2.7) cannot undergo a Hopf bifurcation around e_*.

Proof. The Jacobian matrix J_* around the disease-free equilibrium e_* is given by

$$J_* = \begin{bmatrix} 0 & 0 & -\beta H_0 & 0 \\ 0 & -\delta & \beta H_0 & 0 \\ 0 & p & -c & 0 \\ 0 & \delta & 0 & 0 \end{bmatrix}. \tag{4.2.14}$$

Thus the characteristic equation can be calculated as

$$\lambda^2[\lambda^2 + (c+\delta)\lambda + c\delta - p\beta H_0] = 0, \tag{4.2.15}$$

which has eigenvalues $\lambda_{1,2} = 0, \lambda_{3,4} = \frac{-(c+\delta)\pm\sqrt{(c+\delta)^2-4(c\delta-p\beta H_0)}}{2}$. Clearly, if $\mathcal{R}_0 > 1$ then $\lambda_3 > 0$ and $\lambda_4 < 0$, i.e. the characteristic Eq. (4.2.15) has a positive real eigenvalue, which indicates that e_* is unstable. In addition, it is easy to see that there are no pairs of purely imaginary roots in characteristic Eq.(4.2.15) for any variational parameter, which implies that a Hopf bifurcation cannot occur. This completes the proof of the theorem. □

4.2.3 The connection between the two main models and their parameters

In this subsection we examine the relationship between the two main models' respective parameters. Expressing these connections is not always a trivial task as the hybrid PDE-ABM framework exists in space, while the ODE model's functions are defined as variables only in time. In order to match the two different systems' corresponding parameters, we need to fix some basic features of the spatial domain: first of all, let A denote the complete area of the state space; moreover, for simplicity let us assume that each cell has the area of a unit space – for the latter we introduce the notation σ^2. Finally, let τ denote the unit step in time.

1. **Parameters related to cell death:** We emphasise that the two main models use different approaches to quantify the chance of an infected cell's death – on the one hand, the (4.2.7) ODE model works with a δ death *rate*; on the other hand, the hybrid system uses a P_D *probability*. We can easily obtain a conversion between probability and rate by following the exact meaning behind these parameters. When infected cells die with a death rate δ, their natural decay can be described by the function $e^{-\delta t}$; hence, the probability of an infected cell's death between any two arbitrary time points t_1 and t_2 is given by

$$\frac{e^{-\delta t_1} - e^{-\delta t_2}}{e^{-\delta t_1}} = 1 - e^{-\delta(t_2 - t_1)}.$$

   Specifically, for a time interval of length τ the above formula means that an infected cell dies within that given time frame with a probability of $1 - e^{-\delta\tau}$.

   Applying the Taylor expansion of the exponential function and combining it with the fact that τ is small, we arrive to the $1 - e^{-\delta\tau} \approx \delta\tau$ approximation, i.e. we the connection between δ and P_D is given by

$$P_D \approx \delta \cdot \tau. \tag{4.2.16}$$

2. **Parameters related to new infections:** In this part we establish a connection between the ODE model's infection rate β and the hybrid system's probability of infection P_I. Similarly to the previous point, we need to quantify a relationship between parameters of different dimensions – one being a *rate*, the other a *probability* – but this time the solution is a bit more complex due to the role of spatial factors. We first focus on the hybrid model's P_I parameter solely within the context of the PDE-ABM system. We define the probability of a cell's infection in a way that this probability is directly proportional to the local virus

concentration $V^h(\Omega_{i,j})$ in the (i,j)-th cell (n.b. the number of viruses per unit space) and to the τ time unit, i.e. we have

$$P_I(V^h(\Omega_{i,j}), \tau) = \iota \cdot V^h(\Omega_{i,j}) \cdot \tau, \tag{4.2.17}$$

where ι is some appropriately set constant value. Our next step is to express the relationship between β and P_I for a specifically chosen, simplified scenario – we temporarily assume a homogeneous virus distribution over the domain Ω. Now, the key to expressing P_I in terms of β consists in carefully counting the newly infected cells over one iteration in both the ODE and the hybrid systems. Assuming H healthy cells and a V total number of viruses at a given time, the corresponding number in the ODE model is naturally $\beta \cdot V \cdot H \cdot \tau$. When we switch to the context of the spatial hybrid model, we need to keep in mind that the virus particles are now spread throughout the entire domain Ω, and as a consequence, a single cell is exposed only to the locally, physically present virus particles, whose number is $\bar{v} = V/A$. This means that the expected value of the total number of newly infected cells in the hybrid system is $H \cdot P_I(\bar{v}, \tau)$. Setting the respective values in the two main models equal leads us to

$$P_I(\bar{v}, \tau) = \beta \cdot A \cdot \bar{v} \cdot \tau. \tag{4.2.18}$$

The final step is to combine (4.2.17) and (4.2.18) – by substituting $V^h(\Omega_{i,j}) = \bar{v}$ in the former we immediately obtain $\iota = \beta \cdot A$. The connection between β and P_I is thus captured by

$$P_I(V^h(\Omega_{i,j}), \tau) = \beta \cdot A \cdot V^h(\Omega_{i,j}) \cdot \tau. \tag{4.2.19}$$

We highlight that the hybrid model's P_I parameter takes the above form exclusively when the PDE-ABM model's parameters are configured with a very specific goal in mind: to match the ODE system. Otherwise, when the hybrid software is used completely as a standalone, ι is simply a parameter in the hybrid model.

3. **Parameters related to virus production:** The (4.2.7) ODE model's parameter p corresponds to virus production rate per unit time. Respectively, in our spatial hybrid model's virus dynamical equation (4.2.1) the parameter $g_{i,j}$ represents the virus production rate per unit time per unit space[2] – in particular, $g_{i,j} = f_{i,j}$ within infected cells (see 4.2.2), hence, clearly, $f_{i,j}$ matches p.

4. **Parameters related to virus removal:** Analogously, the respective pair of the

hybrid model's m_V parameter is the ODE system's c virus removal constant.

5. **Parameters related to virus diffusion:** We highlight that the hybrid model's diffusive constant D_V does not have a corresponding parameter in the ODE system, as the latter model is defined only in time and diffusivity is strictly related to spacial dimensions.

We summarize the respective parameters' relationship to each other in Table 4.2.1.

Table 4.2.1: *Description of the hybrid PDE-ABM model's parameters and their relationship to the ODE system. Naturally, the notations [healthy cell], [infected cell] and [dead cell] represent a healthy cell, an infected cell and a dead cell – as a unit – respectively. Analogously, [virion]/σ^2 stands for the concentration unit.*

Symbol	Parameter	Unit	Value corresponding to the ODE model
P_I	Probability of infection for the (i,j)-th cell		$\beta \cdot A \cdot V^h(\Omega_{i,j}) \cdot \tau$
P_D	Probability of death of an infected cell		$\delta \cdot \tau$
$f_{i,j}$	Virus production rate of an infected cell	$\frac{[\text{virion}]}{\sigma^2 \cdot \tau}$	p
D_V	Virus diffusion	$\sigma^2\tau^{-1}$	
μ_V	Virus removal rate	τ^{-1}	c
H_0	The initial number of healthy cells	[healthy cell]	H_0
I_0	The initial number of infected cells	[infected cell]	I_0
$V_0^h(x,y)$	The initial value of virus concentration	[virion]/σ^2	V_0
D_0	The initial number of dead cells	[dead cell]	D_0

τ: time unit
σ: space unit

4.2.4 Implementation

This section describes important technical details related to the hybrid PDE-ABM framework's implementation. Our numerical computations are based on a free and open source java software package, HAL (Hybrid Automata Library) [29]; our source code is publicly accessible in the Github repository [49].

We note that most of our work concerning implementation is centred around customizing the generic HAL package to our concrete virological application, e.g. managing and tracking healthy, infected and dead cells, or putting certain probablistic state change approaches into practice. The deeper, application-independent segments of the HAL library on the other hand do not require any further consideration or optimization from our side, we rely on these core parts without effectuating any modifications. Just to mention one example, the numerical stability for the finite difference diffusion fields is an essential, integral part of HAL itself, and our implementation respects and preserves the original code on these levels – as a consequence, we use the implicit method that the underlying HAL library uses for dealing with the diffusion term.

We simulate the PDE-ABM model's behaviour in an $\Omega \subset \mathbb{R}^2$ two-dimensional bounded domain, hence the ΔV^h Laplacian takes the form of $V^h_{xx} + V^h_{yy}$, where $(x, y) \in \Omega$. The resolution of the state space is chosen to be 200×200, which means we work with a total number of $40,000$ cells (this choice is mainly due to the hybrid model's computational demands – we found that concerning the number of cells $40,000$ is a reasonable value for exploring virus dynamics on an ordinary computer).

Concerning the spatial boundary, we apply Neumann boundary conditions on the edges of the hybrid state space. This approach is favourable for our investigations by guaranteeing zero flux across the boundary. The "closed world" we get as a result is beneficial since it allows us to realistically observe the damage caused by a certain amount of infected cells without external disturbance. Wall-like edges of laboratory assays also naturally correspond to no-flux Neumann boundary conditions, and thus we expect this setting to match the outcome of *in vitro* experiments.

As for the initial conditions in our simulations, we consider the case where we have zero virus concentration in the beginning, but we do have a small number of infected cells in the domain to start with – the virus will spread from these infected cells and as a result, more and more originally healthy cells become infected. This first generation of infected cells is chosen and distributed randomly. Each cell independently has a 0.0005 probability to be in infected state at the beginning of the simulation, otherwise it is in healthy state (with probability 0.9995). The number of initially infected cells is denoted by χ. Figure 4.2.1 illustrates the initial state of our hybrid PDE-ABM model.

After giving a clear definition of the initial and boundary conditions in our implementation, we highlight another interesting technical detail: the internal realization

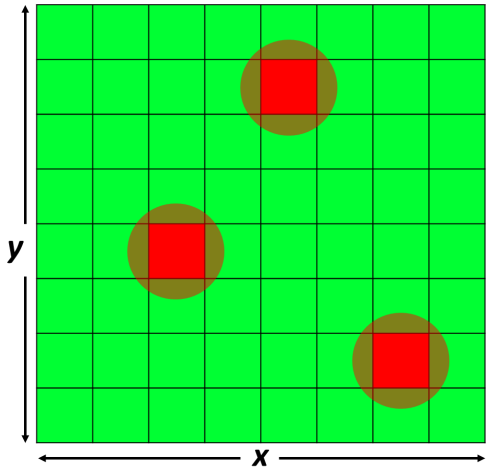

Figure 4.2.1: *An ABM state space where most cells are healthy, while a small number of randomly infected cells start spreading the virus in the domain.*

of the virus production functions. At the abstract definition of the hybrid PDE-ABM model we assumed that the virus source term in (4.2.1) was continuous. This was important for certain theoretical reasons (see Appendix B), but as we move on to implementation-related decisions and solutions, we make a simplifying step regarding this source function. We take a discretized approach, namely, throughout the simulations, a given cell's $g_{i,j}$ virus production function (and in particular, $f_{i,j}$) is quantified assuming that infected cells have a constant virus production rate; formally, $g_{i,j}(t,x,y) =$ a non-zero constant when $s_{i,j}(t) = \mathrm{I}$ and $(x,y) \in \Omega_{i,j}$. We highlight that what really happens at the implementation process is that in each time loop and for each cell (thus, for all $(i,j) \in \mathcal{J}$) we solve equation (4.2.20) to obtain the virus concentration in a given cell:

$$\frac{\partial V^h(t,x,y)}{\partial t} = D_V \Delta V^h - \mu_V \cdot V^h(t,x,y) + g_{i,j}(t,x,y), \quad t > 0,\ (x,y) \in \Omega_{i,j}. \tag{4.2.20}$$

We also emphasise that in order to make the model as realistic as possible, we take some probabilistic considerations into account, and as a result we use a stochastic approach in the implementation of both cell infection and cell death.

- *Stochastic implementation of a healthy cell's infection:* In the $P_I = \beta \cdot A \cdot V^h(\Omega_{i,j}) \cdot \tau$ expression (obtained in (4.2.19)) we assume that the infection rate β and the A area of the domain are constant, but $V^h(\Omega_{i,j})$ is changing in both space and time – once the virus concentration is recalculated for a given cell, we then compare the correspondingly updated P_I value with an $r^I_{i,j}$ random number, which is generated newly for each cell. In case the cell's P_I value is greater than

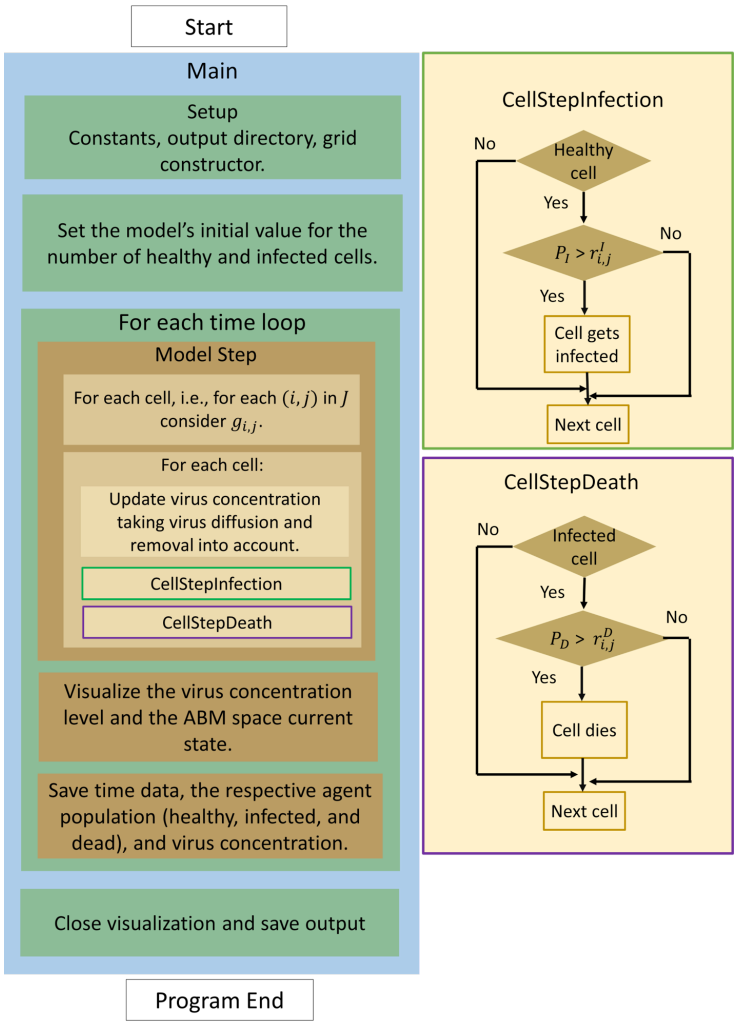

Figure 4.2.2: *The program flow diagram of the PDE-ABM model's numerical simulation based on HAL [29].*

$r^I_{i,j}$, the cell in question gets infected.

- *Stochastic implementation of an infected cell's death:* Similarly, a random $r^D_{i,j}$ number is generated for each infected cell at each time-step, and the given cell's death is determined by comparing this random number with P_D: naturally, the infected cell dies if P_D is greater than $r^D_{i,j}$.

All of the random numbers noted above are real numbers from standard uniform distribution on the interval (0,1) and they are obtained by means of Java's random number generator.

Figure 4.2.2 shows the flow diagram of the program we implemented to simulate the virus spread and observe the spatial distributions of infected cells.

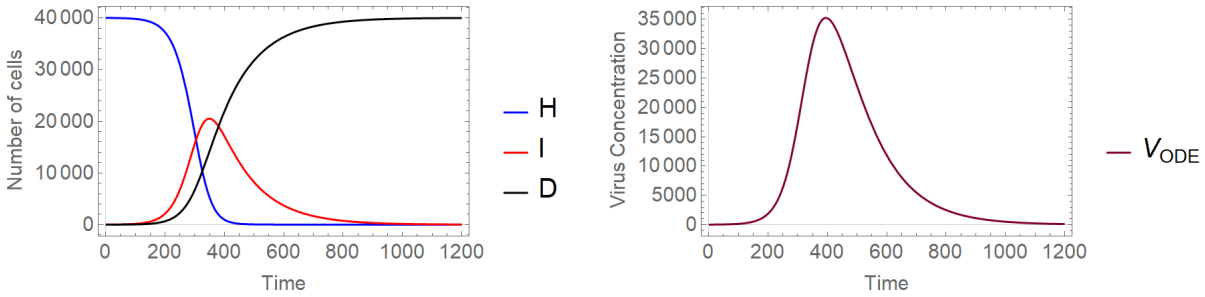

Figure 4.3.1: *A sample solution of model* (4.2.7) *considering the parameters given in* (4.3.1) *with* $H_0 = 40000 - I_0$, $I_0 = 20$, $V_0 = 0$ *and* $D_0 = 0$ *as initial values.* ***Left*** *Number of cells over time.* ***Right*** *Virus concentration over time.*

4.3 Results

We present and explain our most significant computational results in this section. In particular, we illustrate the advantages of the spatiotemporal hybrid system over the classical ODE model, we show an example where we successfully recreate the actual results of an *in vitro* experiment assessing SARS-CoV-2 propagation, moreover, by means of the PDE–ABM system we explore and compare the spatial patterns of influenza and COVID–19.

4.3.1 Comparing the hybrid PDE–ABM model and the ODE model through their solutions

This section is principally dedicated to illustrating the impact of the PDE–ABM model's built-in extra information regarding spatial factors such as diffusion. In the following steps we compare the numerical solutions of the (only time-dependent) ODE model and the hybrid spatiotemporal PDE–ABM system. We emphasise the fact that in this subsection we consider a generic scenario that does not necessarily correspond to influenza or SARS–CoV–2 specifically. Our main goal here is to outline a comparison itself between the two main models making sure that their parameters represent the same virus infection in identical circumstances – with the very important exception of virus diffusion, which incorporates spatial effects.

As for the ODE model's simulation, we consider the following parameter values:

$$\beta = 10^{-6}, \quad \delta = 8 \times 10^{-3}, \quad p = 4 \times 10^{-2}, \quad c = 2 \times 10^{-2}. \tag{4.3.1}$$

Figure 4.3.1 depicts the solution of the ODE model (4.2.7) using the parameter values defined in (4.3.1) and the initial conditions $H_0 = 40000 - I_0$, $I_0 = 20$, $V_0 = 0$ and $D_0 = 0$.

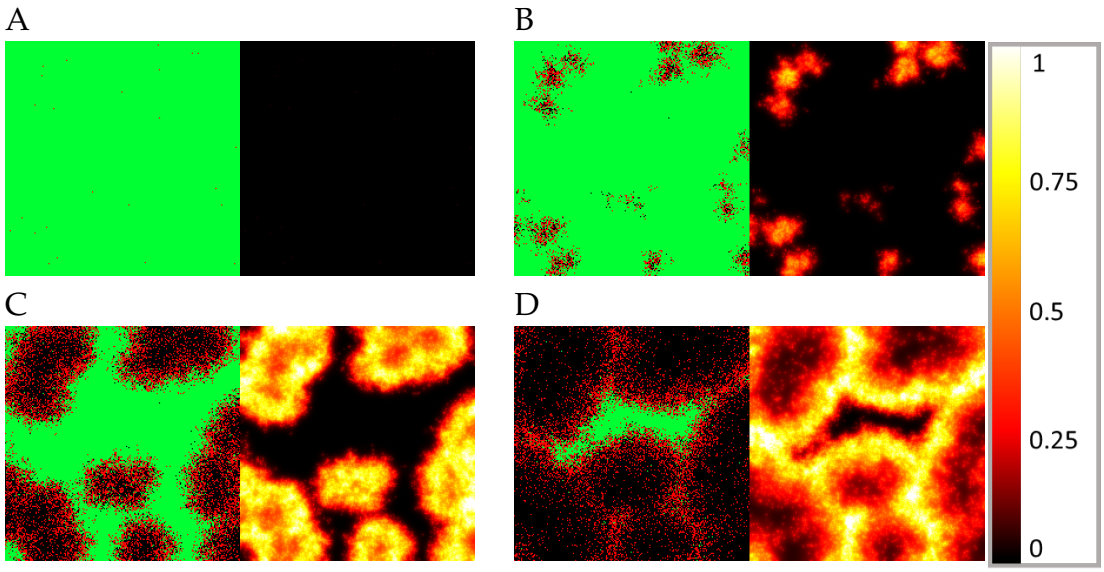

Figure 4.3.2: *Sample hybrid PDE-ABM results considering* (4.3.2) *and* $\boldsymbol{D_{V1} = 0.2}$ *at t = 0, 240, 480, and 720 (**A** - **D**). Infected, healthy, and dead cells (denoted by red, green, and black squares, respectively) are shown on the left and virus spread is depicted on the right in all four subfigures (**A** - **D**). The colour bar is understood in virions per unit space (see Table 4.2.1).*

Once the ODE parameters are set, most of the corresponding hybrid parameter values are automatically defined through the connections described in Table 4.2.1. We obtain

$$P_I = 0.04 \times V^h(\Omega_{i,j}), \quad P_D = 8 \times 10^{-3}, \quad f_{i,j} = 4 \times 10^{-2}, \quad \mu_V = 2 \times 10^{-2}. \tag{4.3.2}$$

Naturally – due to the fact that the ODE model is defined only in time – the hybrid system's diffusion coefficient is an exceptional parameter missing from the list above. To demonstrate the notable difference made by virus diffusion in the hybrid model's numerical solutions (and to compare the latter with the ODE model's solution), we simulate our spatial model with two different diffusion coefficients:

$$D_{V1} = 0.2, \quad D_{V2} = 20 \cdot D_{V1} = 4. \tag{4.3.3}$$

Figure 4.3.2 and Figure 4.3.3 illustrate the different cell and virus dynamics emerging from scenarios that are identical apart from their diffusion coefficients. Both graphs demonstrate cell states on the left and virus spread on the right, captured in four different time points. Infected cells (denoted by red squares) are apparently distributed randomly at the initial state, and virus spread in the domain is clearly originating from infected cells. Comparing these two images we can observe the following significant differences. Firstly, as one would naturally expect, a higher

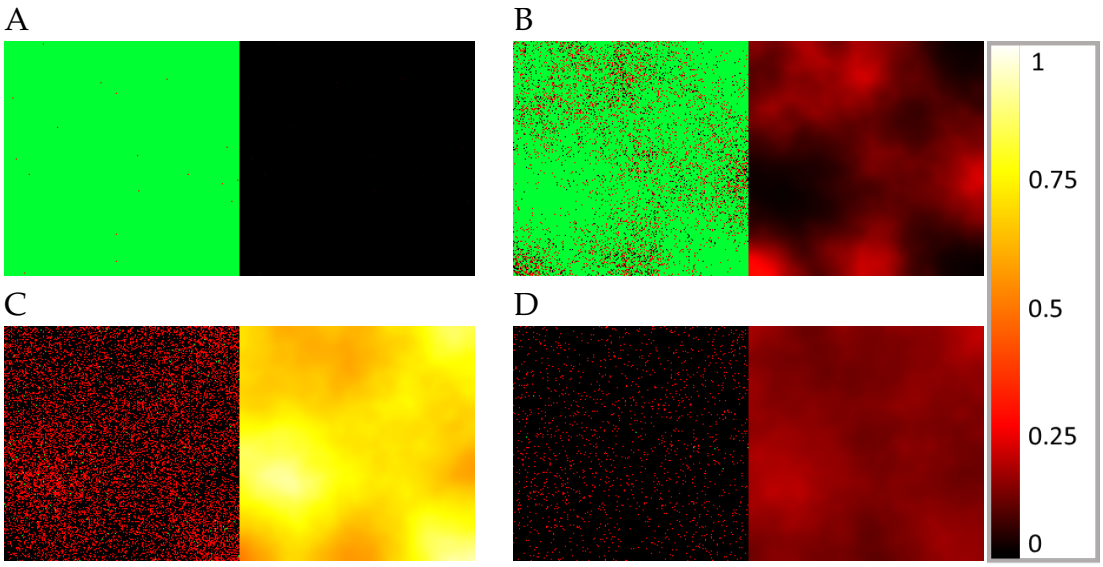

Figure 4.3.3: *Sample hybrid PDE-ABM results considering* (4.3.2) *and* $D_{V2} = 4$ *at t = 0, 240, 480, and 720 (**A** - **D**). Infected, healthy, and dead cells (denoted by red, green, and black squares, respectively) are shown on the left and virus spread is depicted on the right in all four subfigures (**A** - **D**). The colour bar is understood in virions per unit space (see Table 4.2.1).*

diffusion coefficient results in a much more homogeneous infection spread in space. In more detail, Figure 4.3.2 captures a typical low-diffusion scenario where infected cells are found mainly in separate, island-resembling sets, while Figure 4.3.3 shows a fundamentally different phenomenon: the layout of infected cells in the latter image is apparently much more even. An analogous difference is visible on the level of spatial virus distribution as well. On the one hand, Figure 4.3.2 presents distinctive, sharp borders and well-defined lines that characterize low-diffusion virus dynamics, on the other hand, Figure 4.3.3 shows – roughly speaking – foggy, blurred shades corresponding to the increased diffusion value. Our second observation is related to the total number of surviving cells by the end of the simulation: this value is clearly higher for the output obtained with a smaller diffusion coefficient, i.e. in Figure 4.3.2. In other words, according to our simulations, a higher diffusion value results in a higher number of cells that get damaged by infection (i.e. cells that are either currently infected or are already dead).

Figures 4.3.4 and 4.3.5 examine the identical scenarios with a different approach: they describe the corresponding virus dynamics in terms of aggregated cell numbers and virus concentration. These figures contain information in a condensed format – their clarity allows us to detect further dynamical differences caused by different diffusion values. Firstly, we can observe that the magnitude of the virus concentration peak is almost two-folds bigger for a higher diffusion value (Figure 4.3.5) than in the corresponding lower diffusion case (Figure 4.3.4). The peak itself is reached at

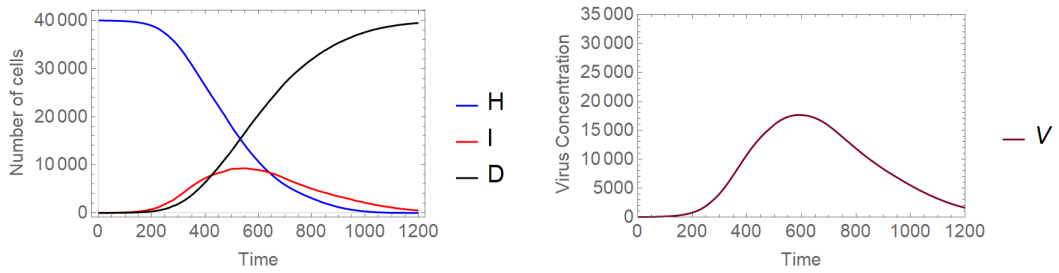

Figure 4.3.4: *A sample solution of the hybrid PDE-ABM model considering parameters specified in* (4.3.2) *and* $\boldsymbol{D_{V1} = 0.2}$. ***Left*** *Number of cells over time.* ***Right*** *Virus concentration over time.*

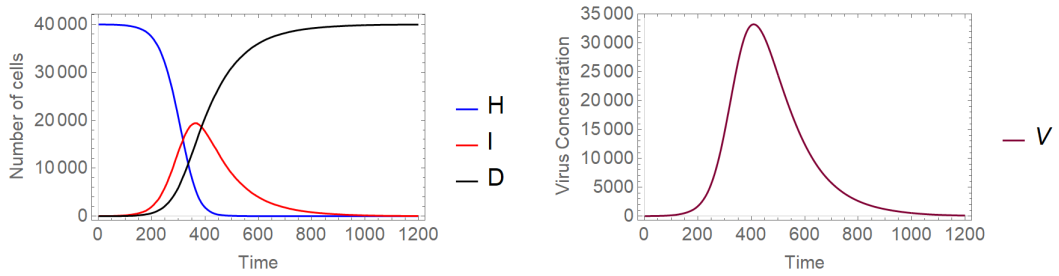

Figure 4.3.5: *A sample solution of the hybrid PDE-ABM model considering parameters specified in* (4.3.2) *and* $\boldsymbol{D_{V2} = 4}$. ***Left*** *Number of cells over time.* ***Right*** *Virus concentration over time.*

around 400τ for $D_{V2} = 4$, while for $D_{V1} = 0.2$ the analogous event takes place only after 600τ, i.e. in the latter case the peak is reached approximately one and a half times slower. The sharpness of these peaks is clearly another significant difference too – a lower diffusion value seems to lead to a flatter virus concentration curve. We highlight that analogous features are visually obvious for the number of infected cells too. Finally, we observe that the faster fall in the number of healthy cells and the quicker increase in the number of dead cells in Figure 4.3.5 suggest that in this particular setting a higher diffusion coefficient leads to a worse scenario overall, according to our results.

Finally, in Figure 4.3.6 we compare the solution of the ODE system with the respective numerical solutions calculated for our spatial hybrid model considering the previously described two different virus diffusion values. Figure 4.3.6 illustrates a special relationship between the solutions of the two main systems: increasing the spatial model's diffusion coefficient apparently impacts the hybrid system's solution in a way that it, roughly speaking, gets closer to the ODE model's numerical solution – this corresponds to the fact that the ODE system represents a scenario where all particles can interact with any other particle, i.e. in some sense the diffusion coefficient is infinite. In other words, the lower the actual virus diffusion value is, the

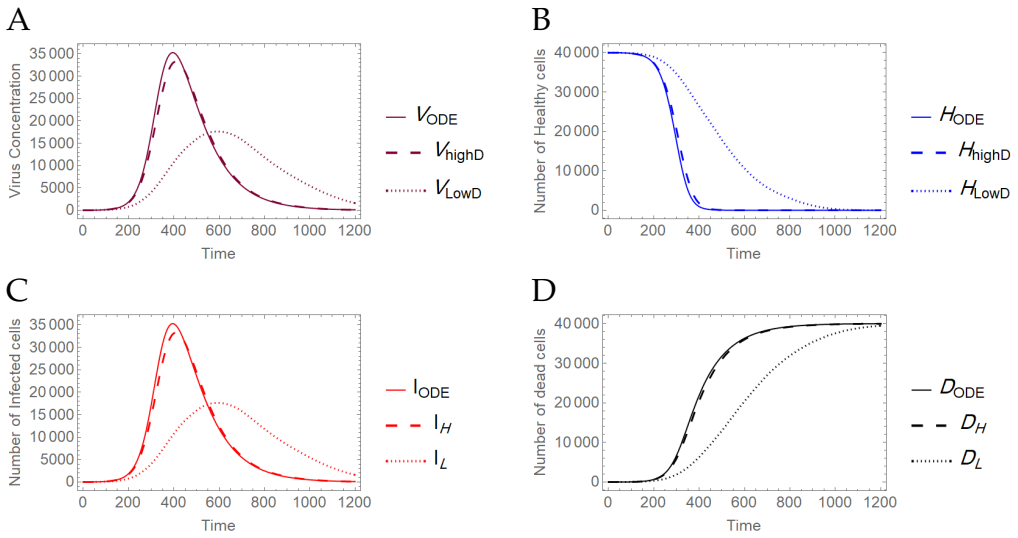

Figure 4.3.6: *Comparison between the ODE model and the hybrid PDE-ABM system with two different diffusion values (as given in (4.3.3)). It is clearly seen that the outputs are very similar for a high diffusion coefficient, as opposed to the case of low diffusion coefficient.* ***A*** *Virus concentration over time.* ***B*** *Number of healthy cells over time.* ***C*** *Number of infected cells over time.* ***D*** *Number of dead cells over time.*

more important it is to consider a more complex spatiotemporal system to model the respective virus spread.

4.3.2 Applications

In one way or another, all applications of the proposed PDE–ABM hybrid model naturally focus on exploiting or predicting spatial information regarding virus spread. The first application is to perform a simulation to obtain as much information as possible on the spatial dynamics of a COVID–19 infection and we compare our computer-generated predictions with actual results of *in vitro* experiments. We also investigate some important differences between influenza and COVID–19 – these are identified more easily thanks to the additional spatial information that is integrated into the hybrid model.

4.3.2.1 Predicting the spatiotemporal spread of SARS–CoV–2 in human airway epithelial cells

Perhaps one of the most straightforward applications is the prediction of spatial virus propagation itself. In this first scenario we simulate the spatial spread of a SARS-CoV-2 infection over the course of seven days and we compare our results with real-life observations obtained by scientific experiments. Specifically, we consider

Figure(4B) in [59], where the authors examine the spread of fluorescent SARS-CoV-2 in human airway epithelial cells at the indicated days with or without peptide treatment – naturally, when we compare our results, we focus on the graphs listed in the line that corresponds to our scenario (i.e. investigating uninhibited virus propagation excluding any treatment).

Examining Figure 4.3.7 (the first one is part of Figure(4B) in [59]), we observe that the key events and features of virus spread match in a reassuring way: the first significant and bigger sign of infection appears at day 4, a clearly visible peak is reached at day 6, while a slight decrease in the infection's severity starts to show between day 6 and day 7. At the same time we highlight that there is a natural limit to how accurately our simulations can recreate the specific events depicted in [59]: firstly, to our best knowledge, the exact values of virus death rate, infection rate and diffusion are not specified in [59]. Secondly, the authors have not disclosed the number of cells they worked with – this means that the resolution of the corresponding ABM fields are different (theirs being unknown). The latter is particularly important as it is most likely one of the reasons why the computer-simulated results are less "sharp" compared to the experimental scenario's images: roughly speaking, the generated results resemble ink spreading in water to some extent, while the *in vitro* results have an apparent grain-like structure. This matter can possibly be the subject of future investigation.

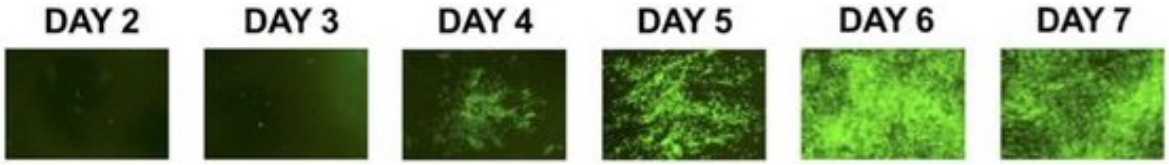

Experimental *in vitro* results of [59] assessing viral spread.

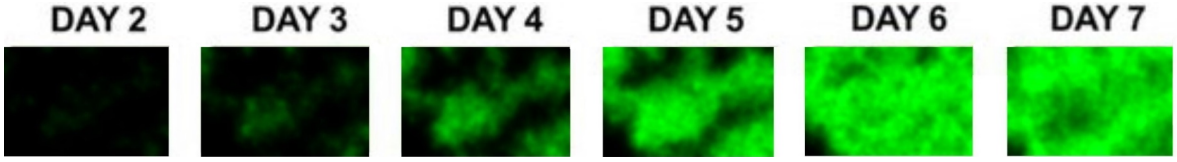

Figure 4.3.7: *The simulated spatiotemporal dynamics of SARS–CoV–2 virus spread in human airway epithelial cells – the results were obtained by our source code implementing the hybrid PDE–ABM model. This sequence of pictures from our model output shows a striking resemblance to Figure(4B) in [59] (seen below), where the latter depicts real experimental results assessing viral propagation. Note the colour choice we apply in this figure: in order to match our simulation's colours to the experimental results in [59], in this particular image the colour green represents virus particles and not healthy cells.*

4.3.2.2 Investigating and comparing the main properties of influenza and COVID-19

While Section 4.3.1 focused on comparing the ODE model's and the hybrid system's respective solutions in a generic scenario, the present – and in some sense, main – section's goal is to explore these solutions for two specific viruses, namely, influenza and SARS-CoV-2.

In order to investigate the propagation of an influenza or COVID-19 infection, we need to set up both of our models with parameters that represent the features of the previously mentioned viruses as accurately as possible. This is a nontrivial task not only because SARS-CoV-2 is relatively new for scientists, but also because several other small, technical, but important issues arise when we want to compare two different kinds of solutions. One particularly intriguing example is the accurate setting of the D_V diffusion coefficient – the $0.65\mu m^2/s \approx 0.2\sigma^2/\text{min}$ value we use in the remaining part of this article is chosen from a reasonable range. We elaborate the limitations, practical considerations and further details concerning the parametrization process in Appendix A. Here we just refer to the tables containing the final values – the ODE model's parameter setting is summed up in Table 4.3.1, while the parameter values we use during the simulations for the hybrid PDE-ABM model are given in Table 4.3.2.

Table 4.3.1: *Description of the* (4.2.7) ***ODE model's*** *parameters. Naturally, the notations [healthy cell], [infected cell] and [dead cell] represent a healthy cell, an infected cell and a dead cell – as a unit – respectively.*

Symbol	Parameter	Unit	Value for influenza	Value for COVID-19	Ref
β	Infection rate	$\text{ml} \cdot [\text{virus copy}]^{-1} \cdot \text{min}^{-1}$	0.94×10^{-7}	1.01×10^{-7}	
δ	The infected cell death rate	min^{-1}	2.66×10^{-3}	7.2×10^{-4}	[42] - [51]
p	The virus production rate	$[\text{virus copy}] \cdot \text{min}^{-1} \cdot \text{ml}^{-1} [\text{infected cell}]^{-1}$	1.666×10^{-2}	3.72×10^{-3}	[42] - [51]
c	The virus removal rate	min^{-1}	2.08×10^{-3}	1.67×10^{-3}	[42] - [51]
H_0	The initial number of healthy cells	[healthy cell]	$40000 - 20$	$40000 - 20$	
I_0	The initial number of infected cells	[infected cell]	20	20	
V_0	The initial value of virus concentration	[virus copy] / ml	0	0	
D_0	The initial number of dead cells	[dead cell]	0	0	

$\tau = 1$ min

Table 4.3.2: *Description of the **hybrid PDE-ABM model's** parameters. Naturally, the notations [healthy cell], [infected cell] and [dead cell] represent a healthy cell, an infected cell and a dead cell – as a unit – respectively.*

Symbol	Parameter	Unit	Value for influenza	Value for COVID-19	Ref
P_I	Probability of infection		$3.76 \times 10^{-3} \times V^h(\Omega_{i,j})$	$4.04 \times 10^{-3} \times V^h(\Omega_{i,j})$	
P_D	Probability of the infected cell death		2.66×10^{-3}	7.2×10^{-4}	
$f_{i,j}$	Virus production from an infected cell	[virus copy] $\cdot$ ml $^{-1}\cdot$ min$^{-1}\cdot$ [infected cell] $^{-1}$	1.666×10^{-2}	3.72×10^{-3}	
μ_V	The virus removal rate	min^{-1}	2.08×10^{-3}	1.67×10^{-3}	
D_V	Virus diffusion	μm^2 / s σ^2 / min	$[3.18 \cdot 10^{-3}, 3.18]$ $[0.97 \cdot 10^{-3}, 0.97]$	$[3 \cdot 10^{-6}, 3]$ $[9 \cdot 10^{-7}, 0.9]$	[48] ,[54]
H_0	The initial number of healthy cells	[healthy cell]	$40000 - \chi$	$40000 - \chi$	
I_0	The initial number of infected cells	[infected cell]	χ	χ	
$V_0^h(x,y)$	The initial value of virus concentration	[virus copy] / ml cell $^{-1}$	0	0	
D_0	The initial number of dead cells	[dead cell]	0	0	

$\tau = 1$ min $\quad \sigma = 14\mu m$

Now we are ready to compare the two different models' predictive performances. Firstly, we consider the case of influenza. Figure 4.3.8 shows the respective numerical solutions obtained by the ODE model and the hybrid system – we note that the solution given by the ODE model is similar to the one described in [52]. We also refer back to an observation we made in Section 4.3.1 regarding the diffusion coefficients: the lower this diffusion value is, the further the hybrid and ODE models' respective solutions are from each other. Finally, we highlight another important aspect in connection with Figure 4.3.8. The authors of [42] and [50] suggest that in the upper respiratory tract about 30%-50% of the epithelial cells are destroyed at the peak of infection. This corresponds to our simulated results in a reassuring way.

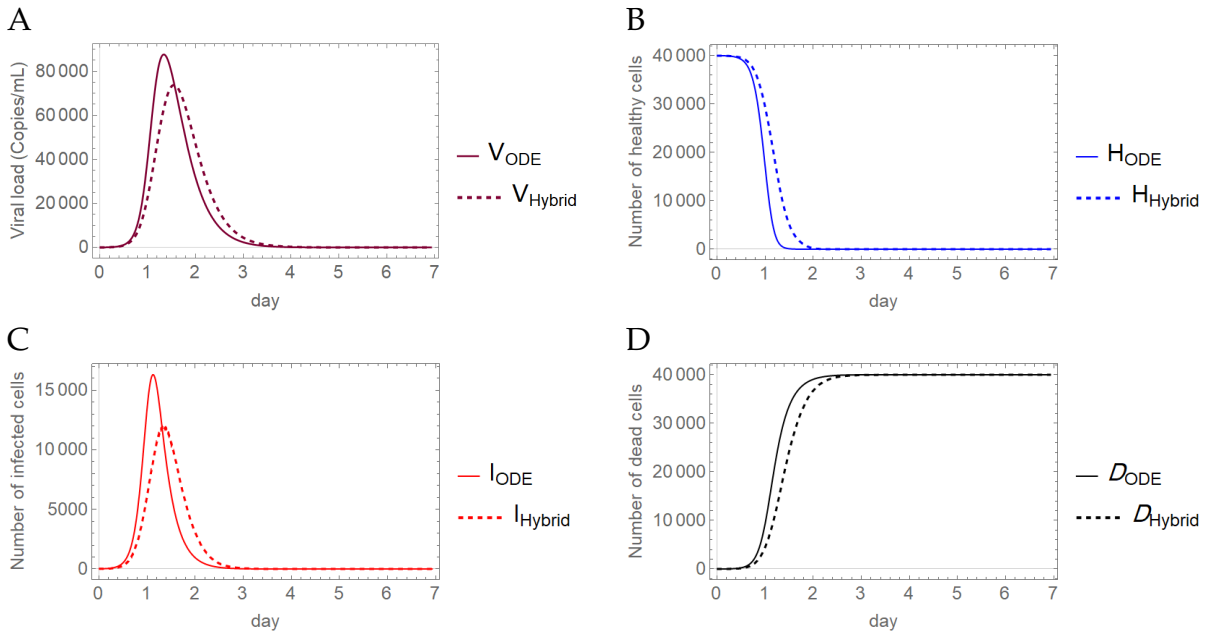

Figure 4.3.8: *Comparison of the ODE model (solid lines) and the hybrid PDE-ABM model (dashed lines) for influenza using the parameters in Tables 4.3.1 and 4.3.2, applying* $D_V = 0.2\sigma^2/min$ *in the hybrid model. All figures depict a change taking place over the course of seven days; specifically,* ***A*** *Viral load (copies/ml),* ***B*** *Number of healthy cells,* ***C*** *Number of infected cells,* ***D*** *Number of dead cells.*

The second subject of our comparative investigations is COVID-19. Similarly to the concept of the previous image, Figure 4.3.9 demonstrates the simulated results given by the ODE model and the PDE-ABM hybrid system, but in this case the computations were executed with the parameters representing COVID-19. We observe that the ODE model and the hybrid system generate solutions that are somewhat closer to each other than their respective solutions computed for influenza.

From this point in this section we examine influenza and SARS-CoV-2 propagation exclusively by means of the hybrid PDE-ABM system.

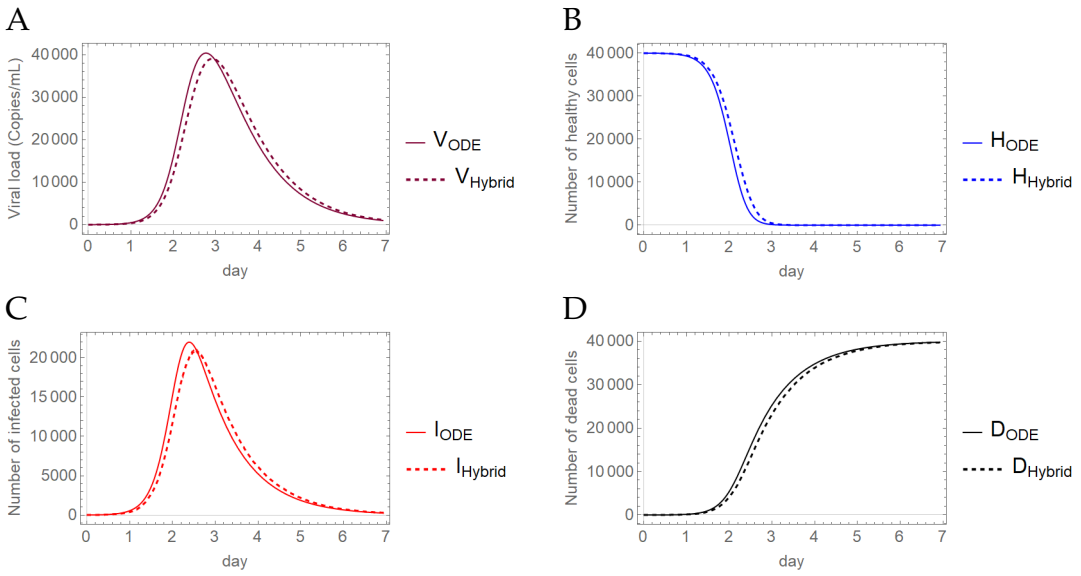

Figure 4.3.9: *Comparison of the ODE model (solid lines) and the hybrid PDE-ABM model (dashed lines) for SARS–CoV–2 using the parameters in Tables 4.3.1 and 4.3.2, applying* $D_V = 0.2\sigma^2/min$ *in the hybrid model. All figures depict a change taking place over the course of seven days; specifically,* ***A*** *Viral load (copies/ml),* ***B*** *Number of healthy cells,* ***C*** *Number of infected cells,* ***D*** *Number of dead cells.*

In order to compare the dynamical features of SARS-CoV-2 and influenza, we firstly simulate the viral load and the number of infected cells for both of these two viruses, the numerical solutions are presented in Figure 4.3.10 (the respective functions for the two different viruses are shown together). First of all, we highlight that while the solutions depicted in this image are only time-dependent functions, the advantage of the hybrid PDE-ABM model is present even behind this particular result – the fact that these numerical solutions were calculated by means of the spatiotemporal hybrid model ensures that their respective values take important physical aspects such as diffusion into account. In particular, we refer to [60] for connecting some of our results to real data and describing the course of influenza infection: this work reports that virus shedding increases sharply between 0.5 and 1 day after challenge and peaks at day 2, while the average duration of viral shedding is 4.8 days. Our computer simulated results shown in Figure 4.3.10 for influenza clearly match with the experimental data of [60].

Some of the results in Figure 4.3.10 might seem surprising at first sight. The image on the left demonstrates that in terms of viral load the peak occurs sooner for influenza, and the value itself taken at this peak is much higher too for influenza compared to COVID-19. On the other hand, if we consider the number of infected cells, the image on the right represents temporal behaviours – and in particular peak values – that in some sense seem like the opposite of the previous observations made

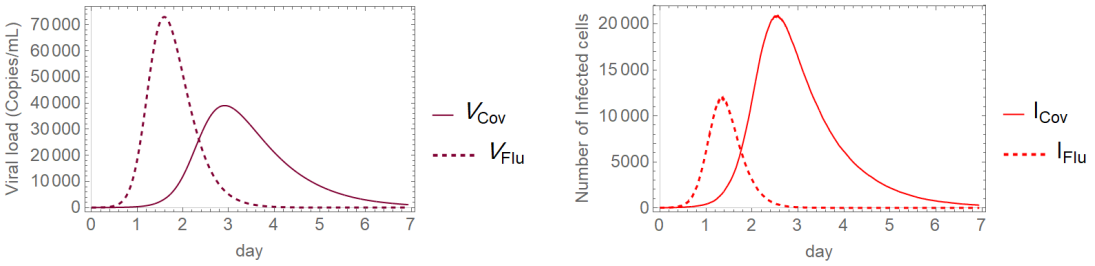

Figure 4.3.10: *The difference between influenza and SARS–CoV–2 infections. The viral load* ***(Left)*** *and the number of infected cells* ***(Right)*** *simulated for influenza (dashed line) and COVID-19 (solid line) using the hybrid PDE-ABM model with* $D_V = 0.2\sigma^2/min$.

for virus concentration. In more detail, the peak of the number of infected cells is much higher for COVID-19 than the respective value for influenza; however, in terms of time to peak, influenza remains to be the "faster" virus out of the two by reaching its maximum in less than two days.

The intriguing features pointed out above will be addressed in more detail after the following discussion of spatial patterns.

Figures 4.3.11 and 4.3.12 demonstrate the distributional patterns of influenza and SARS-CoV-2 propagation. Comparing Figure 4.3.11 with Figure 4.3.12 it is apparent that while both COVID-19 and influenza propagation tend to show spatial patterns that, roughly speaking, resemble flocks or well-outlined explosions, the the sharpness itself of this phenomenon is slightly weaker in the case of COVID-19. In particular, we refer to Figure 4.3.11 / (**B**) vs. Figure 4.3.12 / (**C**): if these images are approached as terrain levels, then the land described by influenza generally seems to have larger gradients in terms of topographic contour lines. We note that this becomes even more apparent for higher diffusion values, where we see rather homogeneous, blurry spatial patterns for SARS-CoV-2, while influenza infection preserves sharper frontlines. We provide supplementary images dedicated to exploring the model's sensitivity to different diffusion parameters in our public github repository [49], where we also share further visual data to grasp the infection dynamics.

We finish this section with emphasising the significance of the hybrid PDE-ABM model by revisiting the results presented in connection to Figure 4.3.10 and observing them in a new light – in particular, we explore how the detailed spatiotemporal layout given in Figures 4.3.11 and 4.3.12 contribute to a better understanding of the original functions of (and questions behind) Figure 4.3.10.

As we have seen at the discussion of Figure 4.3.10, the number of infected cells have a significantly smaller peak value for influenza compared to COVID-19. The new information regarding spatial patterns in Figures 4.3.11 and 4.3.12 gives insight into what really happens in the background. The fact that the ratio of red and black agents can be so high for SARS-CoV-2, while it always remains relatively low for

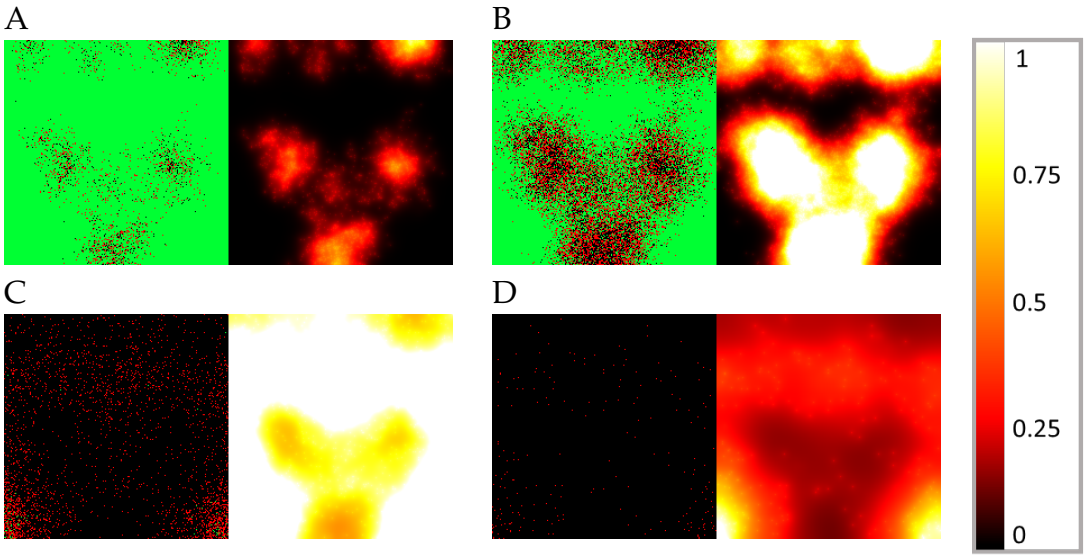

Figure 4.3.11: *Simulated spatiotemporal numerical solutions captured **A** 16 hours, **B** 24 hours, **C** 48 hours, and **D** 64 hours after influenza infection. The computations were performed by means of the hybrid PDE-ABM model using $D_V = 0.2\sigma^2/min$. Infected, healthy, and dead cells (denoted by red, green, and black squares, respectively) are shown on the left, while virus spread is depicted on the right in all four subfigures (**A** - **D**). The colour bar is understood in virus copies per ml per cell (see Table 4.3.2).*

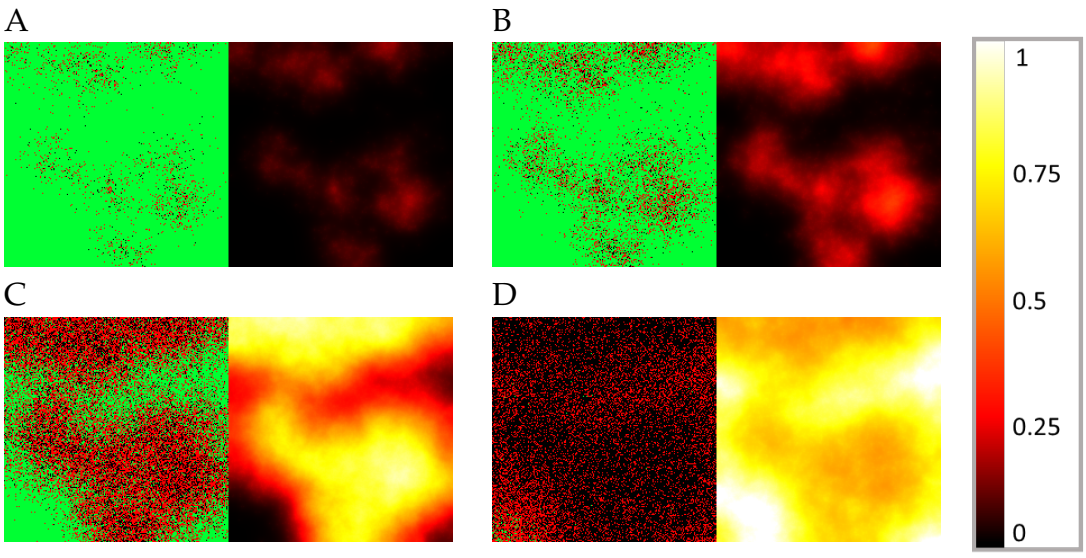

Figure 4.3.12: *Simulated spatiotemporal numerical solutions captured **A** 32 hours, **B** 40 hours, **C** 56 hours, and **D** 88 hours after SARS-CoV-2 infection. The computations were performed by means of the hybrid PDE-ABM model using $D_V = 0.2\sigma^2/min$. Infected, healthy, and dead cells (denoted by red, green, and black squares, respectively) are shown on the left, while virus spread is depicted on the right in all four subfigures (**A** - **D**). The colour bar is understood in virus copies per ml per cell (see Table 4.3.2).*

influenza suggests that influenza-infected cells do not live nearly as long as cells that got infected by SARS-CoV-2 (in fact this is supported by the P_D values of Table 4.3.2).

Carefully comparing Figures 4.3.11 and 4.3.12 can also help us identify a reason why the (quick) viral load peak is higher for influenza in Figure 4.3.10 when its cell-analogue is clearly higher for COVID-19. We begin by exploring what happens on the level of virus concentration when we have (approximately) the same amount of infected cells. In particular, Figure 4.3.11 /(**B**) and Figure 4.3.12 / (**B**) are both scenarios where we seem to have approximately the same amount of infected cells, and at the same time the difference between the corresponding virus concentration images is strikingly apparent. This suggests that the key feature behind the originally mentioned phenomenon might be a difference between the strength of the respective viral source functions – this is in fact verified by the $f_{i,j}$ values of Table 4.3.2. Hence, these observations are significant not just in themselves, but also examples of biological insights provided by the hybrid PDE-ABM model.

4.4 Discussion and concluding remarks

we have applied two different models for investigating the dynamical aspects of virus spread. The first model we considered was a hybrid PDE-ABM system, which is essentially a result of merging a discrete state space representing epithelial cells with a continuous reaction-diffusion equation grasping virus concentration. At the same time, we have used the so-called May-Nowak system – a well-known version of the classical ODE model – as a reference system. As for theoretical completeness, we provide a rigorous analysis of both models in the Appendix, including a well-posedness result related to the hybrid model and the study of the ODE model's temporal dynamics.

The hybrid model's computational implementation and the careful exploration of its results is in some sense the heart of our work – we highlight that our program code is based on a free and open source Java library, HAL (Hybrid Automata Library) [29], commonly used for oncology modeling.

Compared to the ODE system, both the decisive advantages and the main difficulties of the hybrid model are naturally related to the PDE-ABM system's added (and quite high-level) complexity: the inclusion of spatial effects. On the one hand, the limiting factors of this model include an increased computational demand and the fact that it is virtually impossible to consider a really large number of cells on an ordinary computer (we worked with a slice of tissue consisting of $4 \cdot 10^4$ cells). On the other hand however, this hybrid model provides us with the invaluable spatial distribution of infection spread: by running simulations for influenza and SARS-CoV-2 propagation, the results of our spatiotemporal PDE-ABM system suggested that influenza seems to generate sharper frontlines in virus concentration than COVID-19

does; moreover, especially for higher diffusion values, COVID-19 visibly spreads in a more homogeneous manner compared to influenza. This simply would not have been possible using the ODE model as the latter is defined only in time. The ODE system represents a scenario where all cells can interact with all virus particles, or in other words, it implicitly assumes an infinite diffusion coefficient in some sense. Real-life viruses however clearly have a finite diffusion rate. This also means that if the specific virus in question has a relatively low diffusion rate, then the ODE model's predictions regarding infection dynamics will be less accurate: the lower the diffusion coefficient, the more important it is to apply the more complex and more suitable spatial hybrid model. This phenomenon can be observed in Figure 4.3.6: a small diffusion value results in great differences between the respective solutions of the PDE-ABM system and the (4.2.7) ODE model, while the solutions are indeed close to each other for a larger diffusion value.

In terms of verifying the accuracy and correctness of our proposed model, we highlight the results of Section (4.3.2.1) – we have relatively successfully recreated the real results of a scientific *in vitro* experiment: our computer-simulated results matched the actual events and features of infection spread on a satisfactory level. Regarding correctness, we refer to Figure 4.3.8 as well: about 30 to 50% of the epithelial cells are destroyed in the upper respiratory system at the peak of infection, which corresponds to the observations of [42] and [50].

As for possible further improvements and applications of our hybrid spatial model, we mention two main points. Firstly; fine-tuning features such as immune response processes, time delay between infection and virus production, and the phenomenon of cell regeneration are ignored in our current study. These can be the subject of possible future work, although we note that the present model itself can also be considered to be highly realistic in specific cases where some of the above mentioned elements are naturally negligible (e.g. at the short early phase of an infection the immune system has typically not responded yet, while the time frame is too short for cell regeneration to be relevant). Secondly, we plan to apply the hybrid system for parameter fitting analogously as [42] used the ODE model for a similar task for the case of influenza A. In more detail, the authors of [42] calculated a best fit of the ODE model using experimental data on viral load – they extracted viral kinetic parameters such as infection rate, virus production rate, viral clearance rate, and the half-life of free infectious viruses. We simulated the corresponding scenario with both systems and – as expected, considering the relatively low diffusion value set for influenza – there was an apparent difference between the respective numerical solutions of the ODE model and the hybrid system. According to our results, [42] somewhat underestimates the R_0 value: as Figure 4.3.8 shows, in order to obtain a solution with the PDE-ABM model that corresponds to the ODE solution (and hence, to the real curve), it seems that the R_0 value of the hybrid model needs to be

higher than the value estimated by [42] to fit the experimental data. This is another example of how the assumption of homogeneous virus spread can be misleading – the kinetic values obtained by [42] could be adjusted towards their real biological value by means of the hybrid PDE-ABM model. Thus, parameter estimation and fitting the stochastic hybrid model to various virological data is something we also consider as valuable future work.

The complex hybrid approach allows our model to capture fundamental physical processes such as diffusion. We have seen that this is paramount in analysing spatiotemporal virus spread, but we emphasise that virus diffusion itself is not the only example for this feature's significance. Future works using this framework may consider immune response or antiviral drugs. For the latter, drug diffusion is essential, since spatial heterogeneity naturally arises as the drug enters the tissue through the capillary network. Hence, the diffusive property has a key role in the analysis of antiviral drug effectiveness, which can be precisely evaluated only in spatiotemporal context, and our proposed model can be of great use for assessing potential COVID-19 treatment strategies.

Our final synopsis is that the hybrid PDE-ABM model is better suited for thorough and detailed virus spread assessment than the classical ODE system. Following virus propagation on an individual cellular level and taking important spatial effects into account results in a more accurate and complete picture regarding the infection's outcome. Even though the additional integrated details clearly come at a price in terms of computational demand, this pays off very well in the form of information on spatial virus distribution and more accurate predictions.

Chapter 5

Stochastic variability

5.1 Introduction

This chapter is a supplementary study to [61] (chapter 4). In the latter chapter we applied a hybrid mathematical approach to investigate within-host virus dynamical phenomena on a cellular level. Conceptually, the fundamental idea behind hybrid PDE-ABM system was to form bridges between two modeling strategies, hence uniting the respective advantages of discrete and continuous techniques. The hybrid model is constructed by merging *i)* a PDE describing virus concentration and *ii)* an agent-based model representing target cells and their three possible states (healthy, infected, and dead). Finally, the system becomes complete thanks to the inclusion of meaningful interactions and feedback processes between these separate parts. This framework has two fundamentally important advantages. On the one hand, it yields spatially explicit information on virus propagation patterns, and on the other hand, its stochastic approach to state changes supports realistic simulation outputs. In more detail, the latter means that both the infection process (i.e. the $H \to I$ state change) and cell death itself (i.e. the $I \to D$ state change) are internally designed as non-deterministic processes: their implementation reflects the natural randomness of these events. In chapter 4 we predominantly showed this variability element from a single perspective: it was an indispensable feature needed to achieve realistic results. This chapter focuses on these stochastic elements from a new viewpoint.

As simulated infection outcomes may vary based on pure chance, it is essential to quantitatively estimate and outline some of the main uncertainties regarding the results. Our goal here is to assess the stochastic variability in the system: applying the theory of branching processes we rigorously tackle issues such as the probability of spontaneous virus extinction and we also perform some base-level statistical analysis. We emphasise that our investigation regarding stochastic variability is performed exclusively for SARS–CoV–2 infections.

We highlight that our implementation of the hybrid system is based on a free and

open source tool, HAL (Hybrid Automata Library) [29]: both in the present work and in [61] we have adapted, configured, and applied this software package to support repeated simulations for cell-level virus infections – our program code is publicly available on github [49].

5.2 Methods

5.2.1 Discrete-time branching processes

Branching processes [62] have been applied to neutron chain reactions, cancer growth, the survival of mutant genes and population growth, and naturally, one of its main concerns is population extinction. The hybrid PDE-ABM system and the theory of branching processes are two entirely different mathematical frameworks – both are capable of capturing virus propagation in a cell culture, each with its own set of strengths. Since the probability of ultimate, spontaneous extinction (n.b. extinction of the infection) is one of the central questions of the present article, here we turn to the powerful toolbox of branching processes.

Let X_n denote the total size of the population – in our case, the number of infected cells – at the n-th generation for $n \in \mathbb{N}_0$. The state space of the process $\{X_n\}_{n=0}^{\infty}$ is $\mathbb{N}_0$. The process $\{X_n\}_{n=0}^{\infty}$ is called a Galton-Watson branching process if the following three conditions hold.

1. Each individual in generation n has Y_n offsprings in the next generation, where Y_n is a random variable that takes values in $\mathbb{N}_0$. The offspring distribution of Y_n is $\{p_k\}_{k=0}^{\infty}$, i.e. we have

$$P(Y_n = k) = p_k, \quad k = 0, 1, 2, \ldots.$$

2. The number of offsprings an individual has is independent from all other individuals of the population.

3. All generations share the same offspring distribution, i.e. $Y_n = Y$.

We recall that the probability of ultimate population extinction is given by the solution of a fixed-point problem. Specifically, assuming that the probability generating function G_X of the branching process $\{X_n\}_{n=0}^{\infty}$ satisfies certain nice properties (for more details see [62]); moreover, $X_0 = N$, and $E(Y) > 1$; then there exists a unique q, $0 < q < 1$, such that $G_X(q) = q$, and

$$\lim_{n\to\infty} P(X_n = 0) = q^N. \tag{5.2.1}$$

5.2.2 Implementation and parametrization

Our implementation of the hybrid PDE-ABM system is described in detail in chapter 4, is publicly available in [49], and remains identical in this part of the investigation. The default parameters are also the same as given in (4.3.2) in chapter 4.

5.3 Results

All sections of this chapter aim to give a tangible answer to a single, rather generic question:

How much variability is there in the hybrid PDE-ABM system? (5.3.1)

In the following we elaborate two specific, concrete approaches.

5.3.1 Probability of spontaneous extinction

Roughly speaking, this section translates the previously stated main question (5.3.1) as *"Is spontaneous virus extinction possible or likely?"*, answers the latter with theoretical rigorousness, and it does so by approaching the number of infected cells as an $\{X_n\}_{n=0}^{\infty}$ branching process.

To motivate this section we begin with an experimental observation. We increase the baseline SARS–CoV–2 virus removal parameter to favor a potential extinction event and observe where individual infection dynamics arrive over time. Figure 5.3.1 shows the number of infected cells in two different simulations using the exact same parameter values and initial conditions. Clearly, the stochastic approach of the hybrid PDE-ABM framework does allow fundamentally different outcomes by happenstance.

We will apply (5.2.1) to precisely calculate the probability of extinction. As a first step, we focus on one single infected cell and determine the offspring distribution.

5.3.1.1 Single-cell scale: data fitting and parameter estimation

We focus on the generation change from X_0 to X_1 where the number of originally infected cells X_0 is set to 1. The number of direct successors – i.e. generated new infections or offsprings – of the originally considered one single cell is captured by the random variable Y. In order to apply (5.2.1) we need to estimate the $\{P(Y = k) = p_k\}_{k=0}^{\infty}$ probabilities, as these constitute the offspring distribution of the branching process and they determine the probability generating function G_X.

In order to estimate the offspring distribution and its parameters, a small modification is applied in our program code for the scope of the present subsection: newly

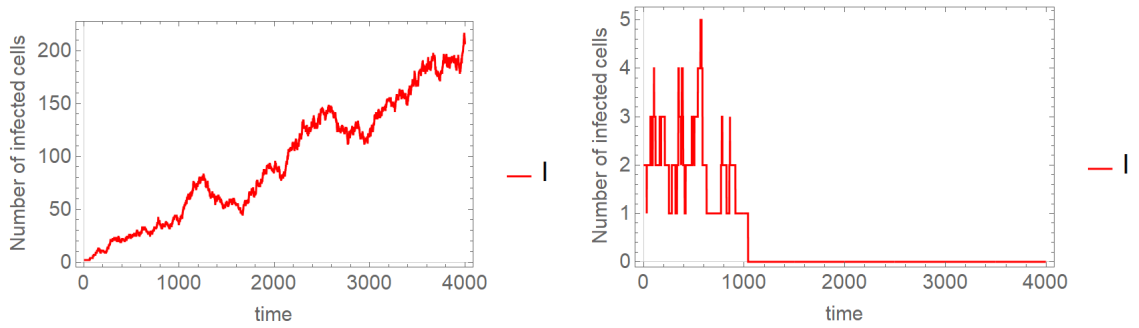

Figure 5.3.1: *The number of infected cells in two different simulations using the exact same parameter values. The stochastic nature of the hybrid PDE-ABM system clearly allows non-deterministic variability in the results. The figures were obtained by using the parameters given in (4.3.2), but a viral removal rate of* $9 \cdot 10^{-2}/min$ *was applied in both simulations (n.b. almost* 50 *times higher than the baseline* μ_V *parameter of SARS–CoV–2). The initial values were* $I_0 = 2$, $H_0 = 40000 - I_0$, $V_0 = 0$ *and* $D_0 = 0$.

infected cells are set not to produce any virus, hence every new infection in the branching process is surely the direct successor of the one infected cell we had in the beginning.

SARS–CoV–2 parameters The results of this paragraph are calculated for the parameter values of SARS–CoV–2 defined in Table 4.3.2 in chapter 4.

We estimate the $\{P(Y = k) = p_k\}_{k=0}^{\infty}$ probabilities by generating a frequency histogram. Specifically, we run our simulation 2000 times with identical parameters and explore where the infection process arrives over time (i.e. in each scenario we examine how many direct successors are generated by the original infected cell). Note that even though we allow these simulations to run for a long time, within the context of the branching process they still represent only one generation step. The results are shown in Figure 5.3.2.

Based on the results of 2000 simulations, one infected cell is responsible for maximum 78 and the minimum zero new infections.

As our next step we calculate the normalized counts: Figure 5.3.3 demonstrates the observed relative frequencies and the respective cumulative values in blue.

These data-based results show an apparent visual similarity to the corresponding features of a negative binomial distribution (shown in red in the same figure). The precise values of the p, r parameters in the $\mathcal{NB}(p, r)$ distribution can be obtained by a standard distribution-fitting procedure to sample data. As a result of using the curve fitting toolbox in *MATLAB*, we obtain $r = 1.0351$ and $p = 0.0781$.

Hence, for the case of SARS–CoV–2 parameter values we have

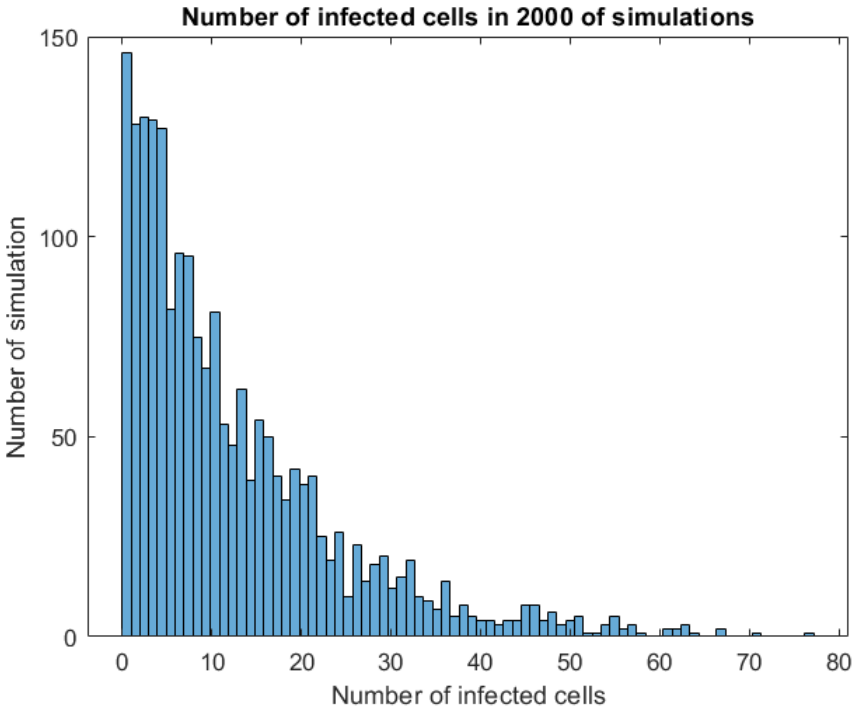

Figure 5.3.2: *Frequency histogram for the offspring distribution based on 2000 simulations. All simulations begin from a single infected cell and were executed with identical SARS–CoV–2 parameters given in Table 4.3.2 in chapter 4.*

$$Y \sim \mathcal{NB}(1.0351, 0.0781). \tag{5.3.2}$$

Fivefold virus removal rate The techniques and the results of this paragraph are analogous to the previous one, the only difference is the application of a five-folds higher virus removal rate. Both data and the fitted distribution are presented in Figure 5.3.4.

Again, we use curve fitting toolbox in *MATLAB* to estimate the parameters – we get $r = 1.0361$ and $p = 0.3032$; i.e. the best fit is given by

$$Y \sim \mathcal{NB}(1.0361, 0.3032). \tag{5.3.3}$$

5.3.1.2 Large-scale results: the fixed-point method

Previously we have successfully estimated the offspring distribution and the probability generating function of the branching process, now we are ready to calculate the probability of extinction. Analogously to the preceding subsection, we will

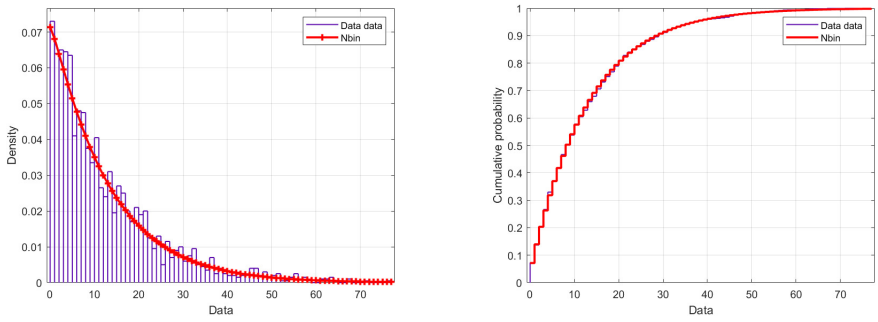

Figure 5.3.3: *The data-based relative frequencies and the respective cumulative values (in blue) vs. the corresponding features of the negative binomial distribution $\mathcal{NB}(p,r)$ with $r = 1.0351$ and $p = 0.0781$ (shown in red). All data were calculated using SARS–CoV–2 parameters as given in Table 4.3.2.*

consider two different virus removal rates – one being that of SARS–CoV–2, the other five times higher.

SARS–CoV–2 parameters Both of the methods we present here are based on (5.2.1). Specifically, for $N = 1$ the probability of extinction is the fixed point of the probability generating function G_X.

- In this case we consider $Y \sim \mathcal{NB}(r,p)$, in other words this scenario works with the theoretical version of the negative binomial distribution. As $r = 1.0351$ and $p = 0.0781$, we have $m = E(Y) = r(1-p)/p > 1$, and hence the fixed point method can be applied. Using the given parameter values in the

$$G_X(x) = \left(\frac{p}{1-(1-p)x}\right)^r \tag{5.3.4}$$

  probability generating function we can easily solve the

$$G_X(q) = q \tag{5.3.5}$$

  fixed-point problem to find $q = 0.0771$.

- In this second case we use the estimated version of G_X which is based on the experimentally observed frequencies and the respective p_k values (Figure 5.3.2). As Figure 5.3.5/**A)** illustrates, the fixed point is calculated by means of *MATLAB* using an iteration method. In this approach we obtain 0.07845 as the probability of ultimate extinction.

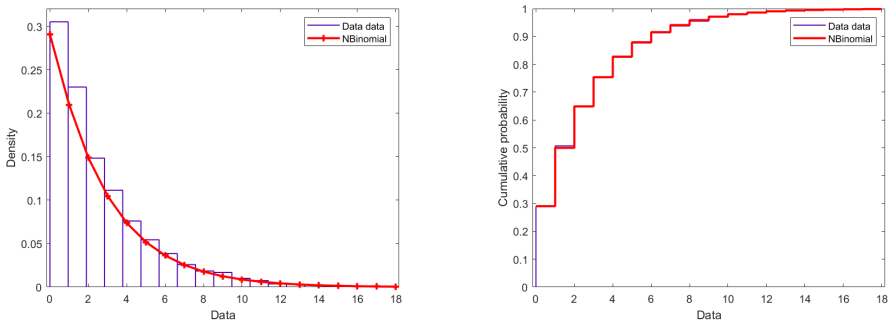

Figure 5.3.4: *The data-based relative frequencies and the respective cumulative values (in blue) vs. the corresponding features of the negative binomial distribution $\mathcal{NB}(p,r)$ with $r = 1.0361$ and $p = 0.3032$ (shown in red). All data were calculated using a five-folds higher virus removal rate compared to the original SARS–CoV–2 parameters given in Table 4.3.2, other parameter values remained unchanged.*

Hence, assuming SARS–CoV–2 parameters as defined in Table 4.3.2 in chapter 4, there is an approximately 7% chance that an infection originating from a single cell goes spontaneously extinct.

Note that this corresponds to our previous results detailed in chapter 4. In the latter we typically considered $I_0 = N = 20$ infected cells at the beginning and we found that virus spread essentially always thrives in this particular setting. In this case the theoretical chance of the infection spontaneously vanishing is q^N : using our newly obtained results this value is basically negligible, which is consistent with our previous observations.

Fivefold virus removal rate The parameters of the previous section can be manipulated to facilitate spontaneous virus extinction. Naturally, an increased virus clearance rate induces a higher probability of spontaneous virus extinction: as Figure 5.3.5/**B)** shows, a quintupled virus removal rate in the SARS–CoV–2 parameters leads to an extinction probability as high as 0.4136. The techniques used in this section are identical to those detailed before and hence we omit the details.

5.3.2 Variability, confidence bands

This part of the article aims to answer the central question (5.3.1) by briefly assessing some of the most fundamental statistical features related to the virus dynamical process. Here we work solely with SARS–CoV–2 virus parameters and similarly to what we assumed in chapter 4. In order to illustrate the stochastic variability of our model, we execute our hybrid simulation 2000 times with an identical setting. A 95% confidence interval is given visually both for the number of

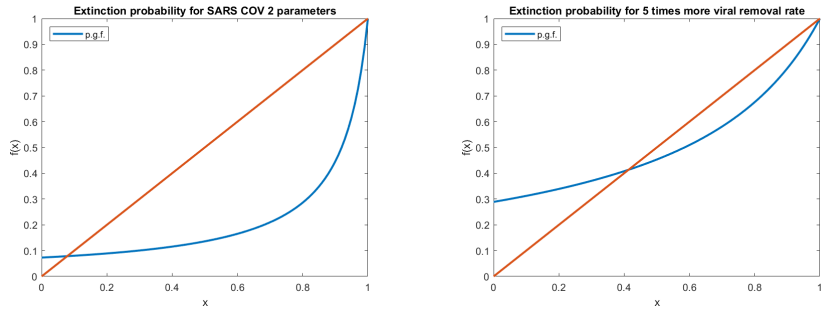

Figure 5.3.5: *Finding the probability of extinction using the fixed-point method for an experimentally estimated version of the G_X probability generating function. The probability of extinction appears as the intersection of the function G_X with the line $y = x$.* ***A)*** *All data were obtained using SARS–CoV–2 parameters.* ***B)*** *Data were obtained using a quintupled the virus removal rate compared to SARS–CoV–2 parameters (other parameter values remain unchanged).*

healthy and infected cells in Figure 5.3.6, the solid lines naturally correspond to the mean values.

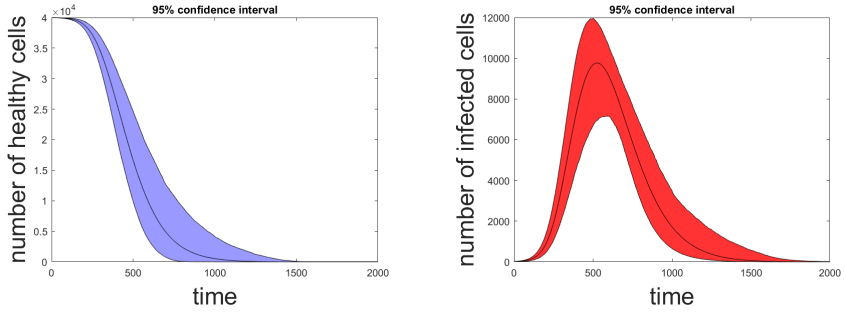

Figure 5.3.6: *Fundamental statistical features representing stochastic variability for our hybrid PDE-ABM model. Results were obtained by repeatedly running the hybrid simulation* 2000 *times, always assuming a default SARS–CoV–2 parametrization and $I_0 = 20$. The result shows in a tangible way that while peak sizes vary due to pure chance, the elimination of the cell culture as an outcome is virtually inevitable.*

The results shown in Figure 5.3.6 correspond to the observations made for our original model. The theoretical probability of spontaneous virus extinction is very small for $I_0 = 20$, and as expected, host cells are completely wiped out in all simulations – on the way to that final outcome small perturbations are however definitely present due to the stochastic nature of the model.

5.4 Discussion

The complex hybrid PDE-ABM approach we considered in chapter 4 allowed us to capture and predict the spatio-temporal viral dynamics in a cell population. Our hybrid model presented two fundamental advantages: firstly, it yielded vital information on the spatial patterns of virus spread, and secondly, its stochastic approach to state changes allowed more realistic simulation outputs. As simulated infection outputs varied based on pure chance, the quantitative assessment of stochastic uncertainty was a crucial remaining task. The present follow-up chapter serves this exact purpose as a supplementary study to chapter 4: our work successfully tackled non-deterministic variability in a tangible way by elaborating two specific, concrete approaches.

Applying the powerful theory of branching processes we rigorously verified an experimental observation suggested by our previous simulations: once established, infections almost never disappear spontaneously. Specifically, we calculated the probability of spontaneous virus extinction and for a single cell obtained an $\mathcal{O}(0.01)$ value, corresponding to our expectations. We highlight that we successfully estimated the offspring distribution of the branching process describing virus spread: based purely on the original model assumptions and our computer-generated data, we concluded that the number of new infections generated by a single infected cell is best described by a negative binomial distribution – we found a virtually perfect correspondence between the estimated and the observed curves. Our research concerning spontaneous ultimate extinction was conducted for SARS–CoV–2 infections, investigating two different virus removal rates. Increased virus clearance can be viewed as a positive immune response or an effect of treatment, this feature remains to be further investigated as future work.

We completed our study by performing some base-level statistical analysis: we explored fundamental features such as mean and we have calculated a 95% confidence interval for both the number of infected cells and healthy cells. The latter results visually confirmed a reasonable level of variability within our framework: on the one hand, non-deterministic uncertainty allows small and natural changes from outcome to outcome, on the other hand, successful large-scale predictions and analysis remain possible as the vast majority of infection curves remains close to their estimated mean.

Chapter 6

Paxlovid

6.1 Introduction

This chapter concentrates on the mathematical evaluation, assessment, and computation-based simulation of a promising antiviral drug, Paxlovid [63], which is essentially nirmatrelvir co-packaged with ritonavir. Nirmatrelvir is a protease inhibitor that is active against M^{pro}: inhibition of the SARS–CoV–2 main protease renders it incapable of processing polyprotein precursors, preventing virus production. Ritonavir is given as a pharmacokinetic enhancer: it slows down nirmatrelvir's metabolism allowing a twice daily administration regimen. Paxlovid (also known as PF-07321332) is orally bioavailable and it has excellent *in vivo* safety profiles [64, 65, 66].

Modeling has enhanced our understanding of the dynamics of viral spread, and it played an instrumental role in developing successful therapies for chronic viral infections such as HIV and HCV [67]. Mathematical models have proved to be indispensable tools in overcoming the challenges posed by the SARS–CoV–2 pandemic, too. In terms of investigating cellular–level antiviral dynamics, one of the most modern, state-of-the-art approaches consists in considering each component's physical dimension and capturing them within the framework of a spatial multiscale model accordingly. These systems incorporate size in a particular manner: rather than operating with a simple numerical value, what change in these models – depending on the size of a given biological entity – are the mathematical tools themselves that are applied to grasp these variables on different scales.

Considering our proposed model in chapter 4, we define a hybrid mathematical model by merging *i)* a partial differential equation representing local virus concentration, *ii)* an agent-based model describing target cells in the lung and their three possible states (uninfected, infected, and dead), and *iii)* a partial differential equation representing nirmatrelvir concentration. Naturally, the respective parts are closely and meaningfully intertwined: each considerable interaction and feedback process

connecting these separate biological participants is given formal definition and appears in the implementation. A detailed motivation, definition and construction of this model type and its various advantages are discussed in chapter 4 – here we limit ourselves to highlighting the role of including crucial spatial mechanisms: unlike other classical models such as the ODE (ordinary differential equations) approach, the present system is defined in both space and time, and consequently is able to capture highly significant – and in nature inherently spatial – physical phenomena such as virus diffusion.

Our goal here is to provide an assessment of Paxlovid based on mathematical simulations. We explore questions such as what happens if nirmatrelvir is taken without ritonavir, or how do expectations for treatment outcome change if tablets are taken with some delay. We emphasise that performing the analogous *in vivo* experiments on an actual person or animal would be either simply impossible or unethical, at the same time the corresponding *in silico* experiment can be conducted in just a few minutes at an ideally low cost.

6.2 Mathematical framework

6.2.1 The hybrid PDE-ABM model

the main multiscale framework is defined via forming meaningful bridges between two important and fundamentally different modeling techniques: *continuous* partial differential equations and *discrete* agent based models.

In the following, let Ω denote the area we are considering. For an *in vivo* experiment this would mean a small part of the lung tissue, while in the case of an *in vitro* experiment it would be the area of a single well in a laboratory plate. Section 6.2.1.2 introduces the *discrete* part of our hybrid model accounting for epithelial cells, whereas Sections 6.2.1.2 and 6.2.1.3 discuss the *continuous* component modeling the virus (V) and drug (N) concentration. The cornerstone observation motivating this separation is that viruses and drug molecules are several magnitudes smaller than epithelial cells [45]. Then, we present the parametrization of the model in Section 6.2.2. Finally, Section 6.2.3 contains details of the implementation.

6.2.1.1 Epithelial cells

One of the most important modeling decisions in chapter 4 was defining epithelial cells as discrete agents in an agent-based model (ABM). The diameter of epithelial cells is relatively significant [46, 47] and consequently, in terms of mathematical conceptualization it is natural to approach cells as separate entities and follow their respective states on an individual level.

The discrete state space of target cells is defined precisely as in chapter 4. For completeness, we recall some of the fundamental technical details; namely, we construct a two dimensional ABM state space by introducing a lattice of $k_1 \times k_2$ agents representing epithelial cells ($k_1, k_2 \in \mathbb{N}$). Cells are identified by means of the corresponding agent's place in the grid, or formally, by the (i, j) indices, where $(i, j) \in \mathcal{J} = \{(i, j) | 1 \leq i \leq k_1, 1 \leq j \leq k_2\}$. Finally, by setting the $\Omega_{i,j}$ notation for the open set occupied by the (i, j)-th cell, we have $\bar{\Omega} = \bigcup_{(i,j)\in\mathcal{J}} \bar{\Omega}_{i,j}$.

Regarding cell states in the context of the ABM space, the main concept is rather straightforward: each agent has three potential states. The latter is formally captured by the state function $s_{i,j}(t)$ representing that in this modeling framework an epithelial lung cell is considered to be either *uninfected*, *infected*, or *dead*:

$$s_{i,j}(t) = \begin{cases} \text{T}, & \text{if the } (i,j)\text{-th cell is alive and uninfected at time } t \\ \text{I}, & \text{if the } (i,j)\text{-th cell is infected at time } t \\ \text{D}, & \text{if the } (i,j)\text{-th cell is dead at time } t. \end{cases}$$

We note that the *uninfected*, *susceptible*, and *target (cell)* expressions are used interchangeably in the context of viral dynamics: they all refer to living cells that are susceptible to SARS–CoV–2 infection but are (for the time being) free from it.

Concerning state dynamics, the transition rules are set to mimic the biological phenomenon in question, the complete list is as follows:

- all living uninfected cells are susceptible target cells to virus infection;
- since the time frame of infection is relatively short, cell birth and cell division are ignored;
- infection is not reversible: an infected cell can not become a healthily functioning uninfected cell again;
- viral infection itself is the only reason for cell death, *i.e.* death related to any other natural cause is not accounted for (considering the 17-month half-life of lung epithelial cells [68], natural apoptosis may be ignored over the course of a 5-day Paxlovid treatment);
- the *uninfected* $\rightarrow$ *infected* state change: a target cell may become infected depending on the local virus concentration at the given cell. Infection itself is randomized and it occurs with a probability of P_I (for more details see chapter 4);
- the *infected* $\rightarrow$ *dead* state change: Analogously to infection, death is governed by a stochastic model with probability P_D.

6.2.1.2 Virus concentration

As discussed, virus concentration $V(t,x,y)$ is described as a variable that is continuously changing in both space and time, and as such, it is formally described by means of a partial differential equation (PDE):

$$\begin{cases} \frac{\partial V(t,x,y)}{\partial t} = D_V \Delta V - \mu_V V + (1-\eta_N(N)) \cdot \sum\limits_{(i,j)\in\mathcal{J}} g_{i,j}(t,x,y), \quad t>0,\ (x,y)\in\Omega, \\ \\ \frac{\partial V(t,x,y)}{\partial \nu} = 0, \quad t>0,\ (x,y)\in\partial\Omega, \end{cases} \tag{6.2.1}$$

where D_V stands for the virus diffusion coefficient, μ_V represents the viral clearance rate, N is the local concentration of nirmatrelvir (*i.e.* the active antiviral component of Paxlovid), η_N is the efficacy function of nirmatrelvir, while $g_{i,j}$ denotes the viral source term for the (i,j)-th infected cell.

Equation (6.2.1) accounts for the following modeling assumptions.

i) Virus particles spread across the domain primarily via diffusion.

ii) A non-specific, non-adaptive, simplified immune system is assumed which clears virions with a constant rate.

iii) A local nirmatrelvir concentration of $N(t,x,y)$ reduces virus production from infected cells by a ratio of $\eta_N(N(t,x,y))$, for more details see Section 6.2.1.3.

iv) Infected cells generate new virus particles in a process that is formally described by the $g_{i,j}$ source functions:

$$g_{i,j}(t,x,y) = \begin{cases} 0, & \text{if } s_{i,j}(t) = \text{T and } (x,y)\in\Omega_{i,j}, \\ f_{i,j}(t,x,y), & \text{if } s_{i,j}(t) = \text{I and } (x,y)\in\Omega_{i,j}, \\ 0, & \text{if } s_{i,j}(t) = \text{D and } (x,y)\in\Omega_{i,j}, \\ 0 & \text{if } (x,y)\notin\Omega_{i,j}. \end{cases} \tag{6.2.2}$$

In general, any reasonable $f_{i,j}(t,x,y)$ function may be allowed in the above formula (for more details see chapter 4 and [48]). We adopted the standard simplification commonly used in the field of viral dynamics: analogously to [69] and [70] a constant virus budding rate is assumed. In particular, we used the estimate $f_{i,j} = 3.72 \cdot 10^{-3}$ copies / (ml $\cdot$ minute $\cdot$ cell) , see [71].

6.2.1.3 Drug concentration

Paxlovid (also known as PF-07321332) is an an orally administered SARS–CoV–2 main protease inhibitor [64, 65, 66]. It is essentially a combination of two different drugs: nirmatrelvir – capable of effectively blocking virus production in infected cells – acts as its main antiviral component, while ritonavir serves to slow down the metabolism of nirmatrelvir to maintain significantly higher concentrations of the participant responsible for M^{pro}-inhibition. We emphasise that nirmatrelvir and ritonavir are not only separate entities as acting components: the corresponding drugs themselves are packaged in individual, separate tablets – this means that the theoretical possibility to take, for example, nirmatrelvir only (without the beneficial effect of ritonavir) is readily available. The remaining part of the section is dedicated to formulate the above statements in the context of the mathematical framework.

Nirmatrelvir concentration is modeled as a continuous variable and is denoted by $N(t, x, y)$. We highlight that – both for simplicity and because of the apparent lack of clinical data – we do not explicitly introduce the analogous $R(t, x, y)$ function for ritonavir concentration. Instead, we focus only on two specific scenarios: ritonavir is either taken as instructed (*i.e.* 100 mg of ritonavir every 12 hours), or not taken at all. Formally, we introduce the boolean r to mathematically grasp the above concept:

$$r = \begin{cases} \text{true}, & \text{if ritonavir is taken following official regimen,} \\ \text{false}, & \text{if ritonavir is not administered at all.} \end{cases}$$

Hence, this boolean is responsible for controlling N through the metabolism-related descriptors.

Two further anatomical details need to be taken into account before we can formulate the governing equations for drug concentration.

First, capillary density is very high in the lung. For example, in the case of rats, there are about 11 epithelial cells per a single alveolus [72]. Considering that there are approximately 40 capillary loops per alveolus [73], this gives circa 4 capillary loops per epithelial cell. Consequently, because of the abundant presence of neighbouring capillaries for a single cell, it is natural to assume a completely homogeneous drug distribution in the alveolar epithelium. Therefore, we work with $N(t)$ instead of $N(t, x, y)$, and the equation describing nirmatrelvir concentration becomes an ODE instead of a PDE.

Second, in order to reproduce the characteristic local concentration curves observed in clinical data (we refer to Figure 2A in [74]), we apply a standard pharmacokinetic (PK) dual compartment approach – akin to that utilized in [75] – assessing antiviral therapy targeting SARS–CoV–2. The latter model consists of a central compartment (*e.g.* stomach) responsible for first-level drug metabolism and a peripheral one (for the purpose of this manuscript the lung) containing the target site of nir-

matrelvir. Technically, we introduce an additional $c(t)$ function representing drug concentration at the central compartment – this is the the amount of nirmatrelvir that is already present in the patient's system, but is not yet locally available at the level of the lung's epithelial cells. In the context of the two-compartment model, $N(t)$ corresponds to the peripheral compartment's nirmatrelvir concentration. Similarly to the case of $N(t)$, an ODE is used to describe $c(t)$.

The complete system for nirmatrelvir concentration is then formally described by the following set of equations:

$$\begin{cases} \frac{\mathrm{d}c(t)}{\mathrm{d}t} = -\mu_c(r)c(t) + S(t,r), \\ \\ \frac{\mathrm{d}N(t)}{\mathrm{d}t} = -\mu_N(r)N(t) + \mu_c(r)c(t), \end{cases} \tag{6.2.3}$$

where S represents the nirmatrelvir source function in the body, corresponding to a twice-daily administration regimen (the time unit being $\tau = 1$ minute):

$$S(t,r) = \begin{cases} K(r), & \text{if } \mathrm{mod}(t, 12 \cdot 60) = 0 \\ 0, & \text{otherwise.} \end{cases}$$

The choice of $K(r)$ is discussed in the following section.

We note that the above set of equations holds primarily for *in vivo* scenarios. In case of *in vitro* experiments one might, for example, consider a simpler, constant presence of nirmatrelvir.

6.2.2 Parametrization

The configuration of the stochastic ABM state space and the PDE layer describing SARS–CoV–2 infection had been given in chapter 4. Here we set the parameter values that are related to the (new) calibrated layer representing Paxlovid-based antiviral therapy.

- **Drug removal rates: $\mu_c(r), \mu_N(r)$.** As we do not have direct information on the μ_c, μ_N coefficients, we deduce them indirectly by using frequently measured nirmatrelvir blood concentration values communicated in [74]. Of course, this argument raises the question whether it is reasonable to use blood concentration values to estimate local drug concentrations in the lung – the validity of this approach is reassured by the results of [76]. The $\mu_c(r)$ and $\mu_N(r)$ coefficients were set using *Mathematica*. We note that in the process we also benefited from *a priori* information on ritonavir from [74] and [77]: we used that in non-ritonavir-boosted cases the active component is apparently metabolised 3–4 times faster. The *Mathematica* notebook is available in our public Github repository [78].

- **Efficacy: η_N.** In our model η_N is defined by means of a Hill function – the parameters of the latter are set precisely to obtain an efficacy of 50% when the drug concentration takes the value of EC_{50} for nirmatrelvir w.r.t. SARS–CoV–2 (the latter parameter is approximately 62 nM according to [65]). Formally, η_N is defined as

$$\eta_N(N(t)) = \frac{1}{1 + \frac{EC_{50}}{N(t)}}. \tag{6.2.4}$$

  For simplicity, we use the notation $N(t)$ for drug concentration whether it is understood in nanomolars or in nanogramms per millilitre. Our implementation internally takes care of conversions when necessary due to data arriving from different sources.

The most important parameter values are summarized in Table 6.2.1.

Table 6.2.1: *Parameter configuration is primarily based upon best fit to actual data communicated in [74]. Previously existing parameters are defined in chapter 4.*

Symbol	Parameter	Unit	Ritonavir–boosted	Value
$\mu_c(r)$	drug removal rate	τ^{-1}	false	0.015
	in the stomach		true	0.005
$\mu_N(r)$	drug removal rate	τ^{-1}	false	0.013
	in the lung		true	0.004
$K(r)$	drug source	ng/ml/τ	false	1800
	in the stomach		true	6800

τ: time unit

6.2.3 Implementation

The present work is a direct continuation of chapter 4 and hence its technical foundations and principles remain unchanged. For the sake of compactness we avoid repetitive details – here we limit ourselves to summarizing the extended structure of our updated software with the help of the flowchart in Figure 6.2.1. The chart is divided into two main columns. On the left we have the program flow itself from

start to finish, while the three additional boxes on the right contain further details on the respective functions. After setup and initialization, the execution is controlled by a time loop: nirmatrelvir concentration, virus concentration, and cell states are updated for each time step (in our case $\tau = 1$ minute).

1. Nirmatrelvir concentration is calculated first (highlighted with a green frame): the most fundamental details of the process are given on the right-hand side, highlighted with an identical colour. There is a clear distinction between *in vitro* and *in vivo* cases: while the first scenario is implemented assuming a constant drug concentration, the latter utilizes a two-compartment PK system.

2. Updating virus concentration values entails recalculating the current values considering both natural decay and inflow from infected cells taking virus diffusion into account.

3. After the new drug and virus concentration values have been obtained at each cell, we are ready to update the cell states, i.e. consider potential cell infection and cell death – the former is highlighted in purple, the latter in gray. The schematic details are shown on the right with corresponding colours; we emphasise that the respective stochastic cores of these processes are very similar to each other. In both cases the algorithm calculates the probability of either infection or death.

Our numerical simulations are based on a free and open source java software package, HAL (Hybrid Automata Library) [29]; our source code is publicly accessible in the Github repository [78].

6.3 Results

6.3.1 Replication of in vitro pharmacometrics of Paxlovid

The initial step in identifying and testing clinically promising antiviral drugs consists in performing a great number of *in vitro* experiments evaluating their overall effects. We begin with this straightforward approach, too. In this first scenario we simulate a series of experiments corresponding to *in vitro* cases with different nirmatrelvir concentrations – all these configurations are otherwise identical in every other aspect. We simulate the course of SARS–CoV–2 infection over the course of four days and we compare our computer-generated predictions with real-life observations obtained by scientific experiments assessing nirmatrelvir. Specifically, we consider Figure 3D in [64] – here the authors evaluate PF-07321332 inhibition for (among other viruses) SARS–CoV–2 in viral-induced CPE assays, and their results are given for a series of different drug concentration values.

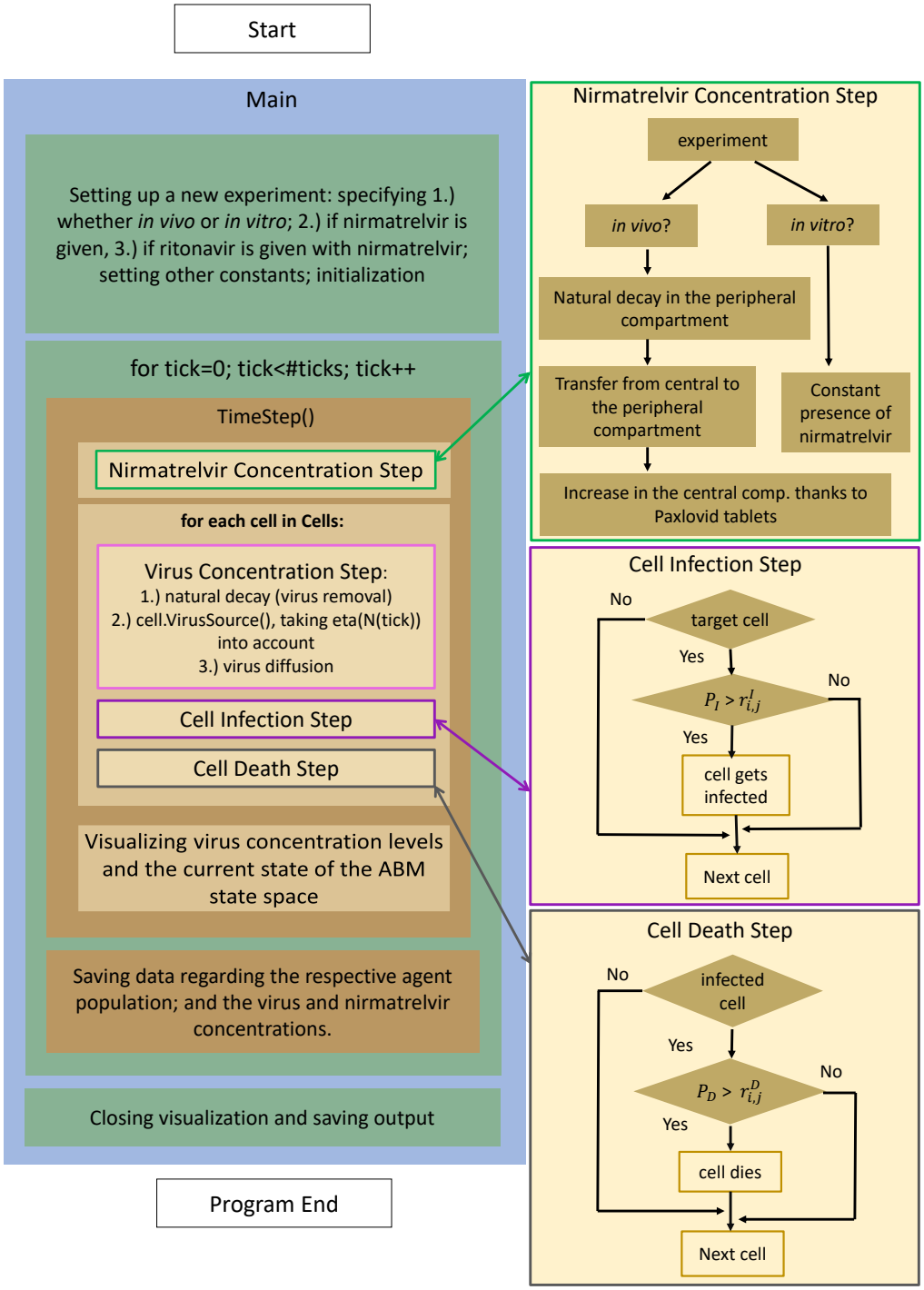

Figure 6.2.1: *The program flow diagram of the PDE-ABM model's implementation based on HAL [29].*

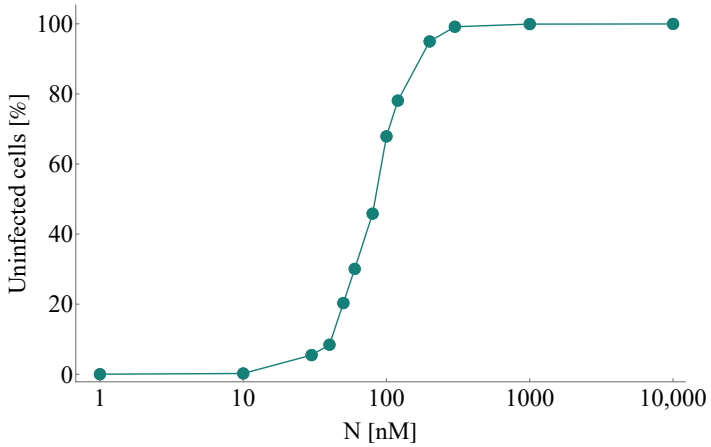

Figure 6.3.1: *A simulated series of in vitro experiments with increasing initial nirmatrelvir concentrations. Concentration levels are assumed to be constant throughout the entire course of each experiment. Every simulation follows the emerging infection dynamics for* 4 *days. SARS–CoV–2 infection and nirmatrelvir treatment are initialized simultaneously. Our computer-generated predictions correspond reassuringly to real-life scientific measurements assessing infection inhibition of PF-07321332, see Figure 3D in [64].*

Figure 6.3.1 demonstrates a notable resemblance to Figure 3D in [64]. Key features of inhibition efficacy match in a reassuring way: the characteristic shape itself of the calculated curve looks identical to its clinical counterpart, and the numbers connected to the main concentration window (approximately between 10 nM and 300 nM) corresponding to tangible increase are essentially the same, too.

While there is a clear match between clinical data and our calculated results, we highlight that there is a natural limit to accuracy due to simple lack of data. Both simulated and real-life outcomes naturally depend on key features such as the number of days the experiment went on for or the complete resolution of the state space (*i.e.* the total number of cells). While the supplementary material of [64] suggests that the authors mostly considered time intervals corresponding to 3–5 days, several parameter values are either unknown by nature or have not been disclosed.

6.3.2 Exploring in vivo pharmacometrics of Paxlovid

In this section we present and explain our most significant computational results representing simplified *in vivo* cases. We explore a series of scenarios with various configurations, one basic feature remains unchanged however in all of them: we assume that the most fundamental instructions given in Paxlovid's documentation [65] are followed at least for its nirmatrelvir component. Technically this means that once patients start taking Paxlovid, they steadily take at least nirmatrelvir for 5 days straight, 1 dose every 12 hours. Since Paxlovid is essentially nirmatrelvir co-packaged

with ritonavir, technically it is possible that a patient – either consciously because of an existing drug allergy or simply because of forgetfulness – takes only nirmatrelvir, without the added benefits of ritonavir. This degree of freedom is allowed and investigated throughout the simulations. Some other combinations and scenarios were excluded due to lack of data, again others were omitted simply because of the limited scope of the article.

It is important to note that the inherent, rather sharp distinction between the *in vitro* and *in vivo* clinical categories becomes notably smoother in the simulated context of our mathematical model. Figuratively speaking, we perform *in vivo* experiments "as if they were" *in vitro* in the sense that we have full control over (and full information on) which specific biological or anatomical processes are included and which ones are left out. Our framework is called hybrid because of the different mathematical theories it unites, but it proves to be hybrid in this point of view as well.

6.3.2.1 *In silico* testing of immediate Paxlovid-based intervention

We begin by simulating three basic scenarios and observing the respective outcomes. Figure 6.3.2 shows the course of SARS–CoV–2 infection assuming no antiviral intervention, Figure 6.3.3 follows a case where the patient takes nirmatrelvir only (*i.e.* the main acting component of Paxlovid, without the benefits of ritonavir), while Figure 6.3.4 represents the scenario where Paxlovid is taken exactly according to official instructions.

For the latter two cases we plot total virus concentration and nirmatrelvir concentrations both at the first level of metabolism in the body and locally at the epithelial lung cells, the results are shown in Figure 6.3.5.

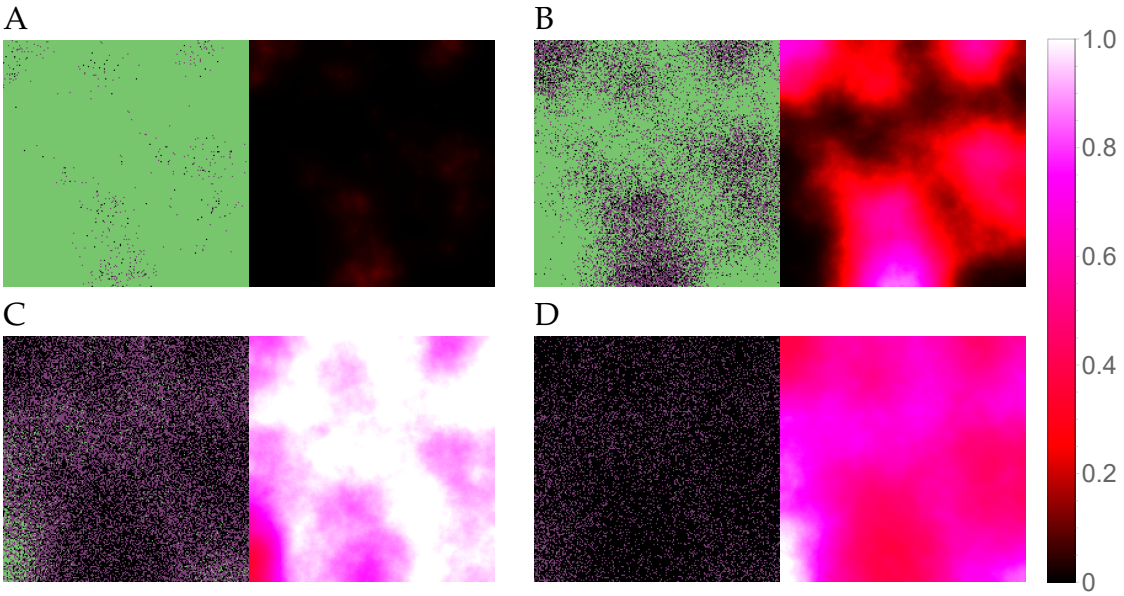

Figure 6.3.2: *Simulated spatiotemporal solutions captured (**a**) 24 hours, (**b**) 48 hours, (**c**) 72 hours, and (**d**) 96 hours after SARS–CoV–2 infection. **No antiviral intervention** took place in this case. The cellular state spaces are depicted on the left in all four subfigures; uninfected, infected and dead cells are denoted by green, purple, and black squares, respectively. Virus concentration values are shown on the right. The colour bar is understood in virions per unit space.*

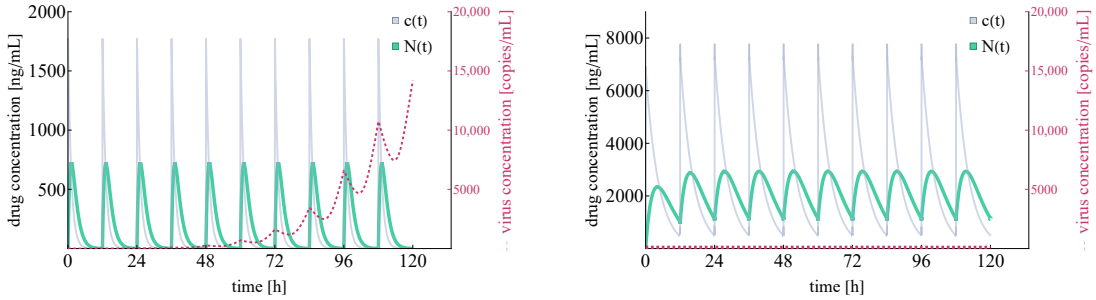

(a)nirmatrelvir only (b)Paxlovid

Figure 6.3.5: *Integrated virus concentration and nirmatrelvir concentration levels for two different scenarios representing nirmatrelvir-based intervention. Subfigure (**a**) shows the simulated outcome of applying nirmatrelvir without ritonavir, while subfigure (**b**) depicts the results of rigorous treatment with Paxlovid (ritonavir-boosted nirmatrelvir). SARS–CoV–2 virus concentrations are coloured in red (shown dashed), nirmatrelvir concentration levels – $N(t)$ and $c(t)$ – are depicted in sea green and light purple, respectively.*

In Figure 6.3.5, both the integrated virus and drug concentration values are note-

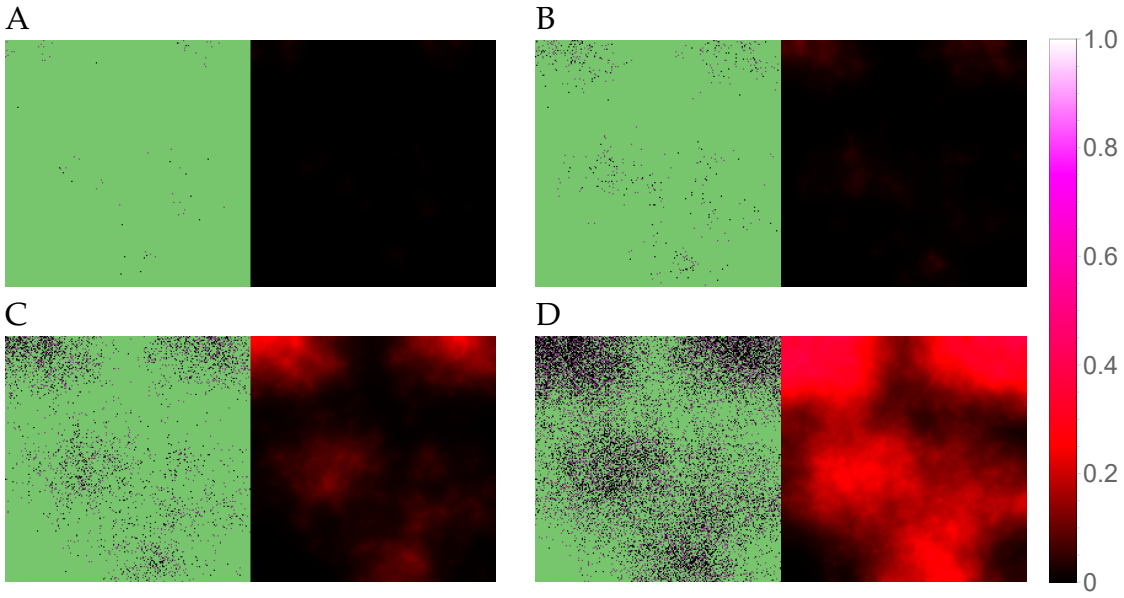

Figure 6.3.3: *Simulated spatiotemporal solutions captured (**a**) 24 hours, (**b**) 48 hours, (**c**) 72 hours, and (**d**) 96 hours after SARS–CoV–2 infection and simultaneous treatment with nirmatrelvir. In this case **nirmatrelvir was given without ritonavir**, intervention took place with no delay. The cellular state spaces are depicted on the left in all four subfigures; uninfected, infected and dead cells are denoted by green, purple, and black squares, respectively. Virus concentration values are shown on the right according to the scale in Figure 6.3.2.*

worthy. Firstly, we highlight that nirmatrelvir concentration levels clearly correspond to Figure 2A in [74] – this means that our simulations (both in the ritonavir-boosted and in the nirmatrelvir-only case) are running with highly realistic nirmatrelvir concentration levels. Secondly, our computational results correspond to straightforward, basic expectations suggested by the packaging of Paxlovid. In more detail; on the one hand nirmatrelvir in itself seems to be insufficient to control the infection (which explains why Paxlovid does not simply consist of nirmatrelvir tablets), and on the other hand, ritonavir-boosted nirmatrelvir is apparently capable to stop infection entirely (which is in accordance with the simple fact that Paxlovid is an authorized drug of great promise).

6.3.2.2 Evaluating the effects of treatment delay

The previous section's premise was similar to a classical *in vitro* configuration – in this original default case, infection and treatment began simultaneously. In order to make our model more realistic, here we introduce and explore a new degree of freedom: treatment delay.

We begin by exploring how simulated predictions seen in Figures 6.3.3, 6.3.4, and

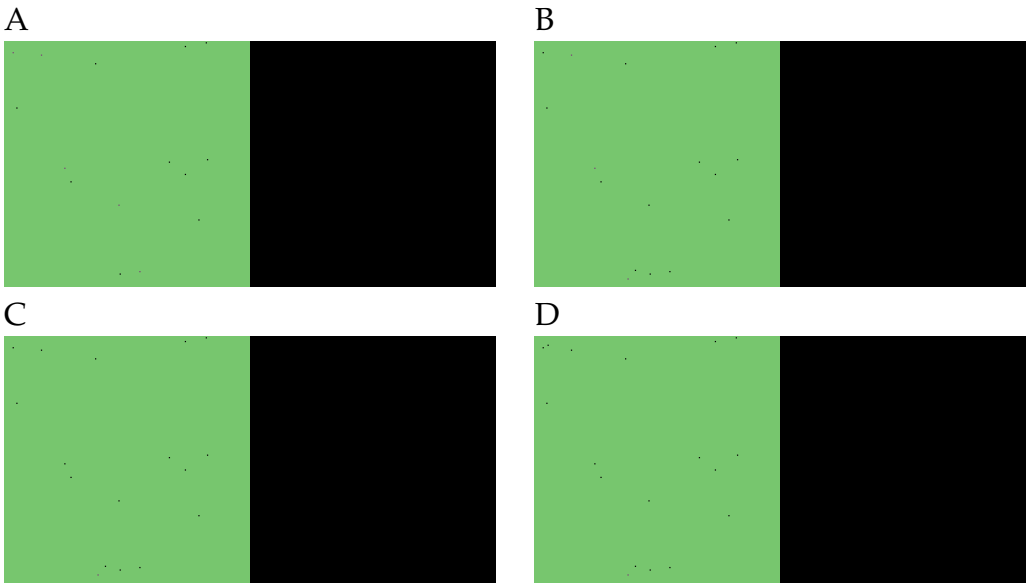

Figure 6.3.4: *Simulated spatiotemporal solutions captured (**a**) 24 hours, (**b**) 48 hours, (**c**) 72 hours, and (**d**) 96 hours after SARS–CoV–2 infection and simultaneous treatment with Paxlovid. In this case **ritonavir-boosted nirmatrelvir was given**,i.e. official instructions regarding Paxlovid were followed. Intervention took place with no delay. The cellular state spaces are depicted on the left in all four subfigures; uninfected, infected and dead cells are denoted by green, purple, and black squares, respectively. Virus concentration values are shown on the right according to the scale in Figure 6.3.2.*

6.3.5 would change if Paxlovid tablets were given with a delay.

In particular, Figure 6.3.6 and Figure 6.3.7 illustrate virus dynamical processes that are otherwise identical to the scenarios of Figure 6.3.3 and Figure 6.3.4, respectively, except for a 36-hour delay in initiating nirmatrelvir-based treatment (this also means that we follow these cases for an overall longer time period). The ritonavir-boosted scenario is particularly interesting. Though the first 36 hours see uninhibited virus spread, Figure 6.3.7 confirms that Paxlovid can control infection relatively well even in this particular, less favorable scenario: after the first 2 days there are almost no new cell infections at all, the only detectable change between the last four subfigures is infected cells gradually turning dead.

Similarly to Figure 6.3.5, Figure 6.3.8 shows integrated virus concentration and nirmatrelvir concentration levels, but, naturally, considering a 36-hour delay before Paxlovid is given.

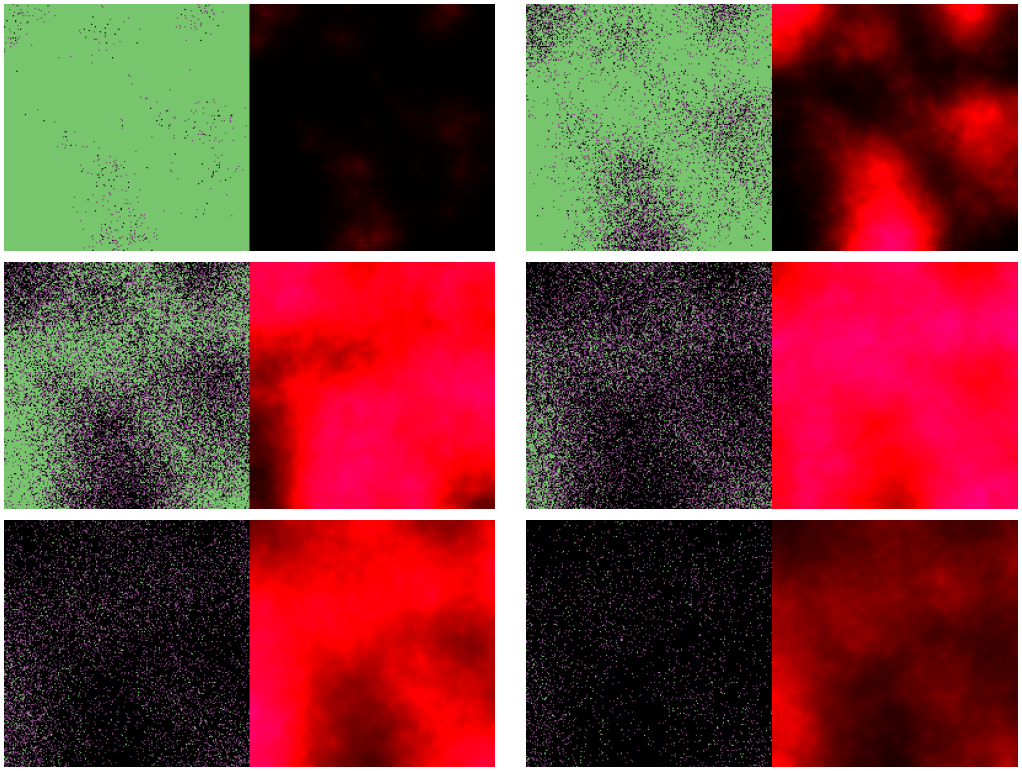

Figure 6.3.6: *Simulated spatiotemporal solutions captured (**a**) 24 hours, (**b**) 48 hours, (**c**) 72 hours, (**d**) 96, (**e**) 120, and (**f**) 144 hours after SARS–CoV–2 infection and delayed treatment with nirmatrelvir. In this case **nirmatrelvir was given without ritonavir**, intervention took place after a 36-hour delay. The cellular state spaces are depicted on the left in all four subfigures; uninfected, infected and dead cells are denoted by green, purple, and black squares, respectively. Virus concentration values are shown on the right according to the scale in Figure 6.3.2.*

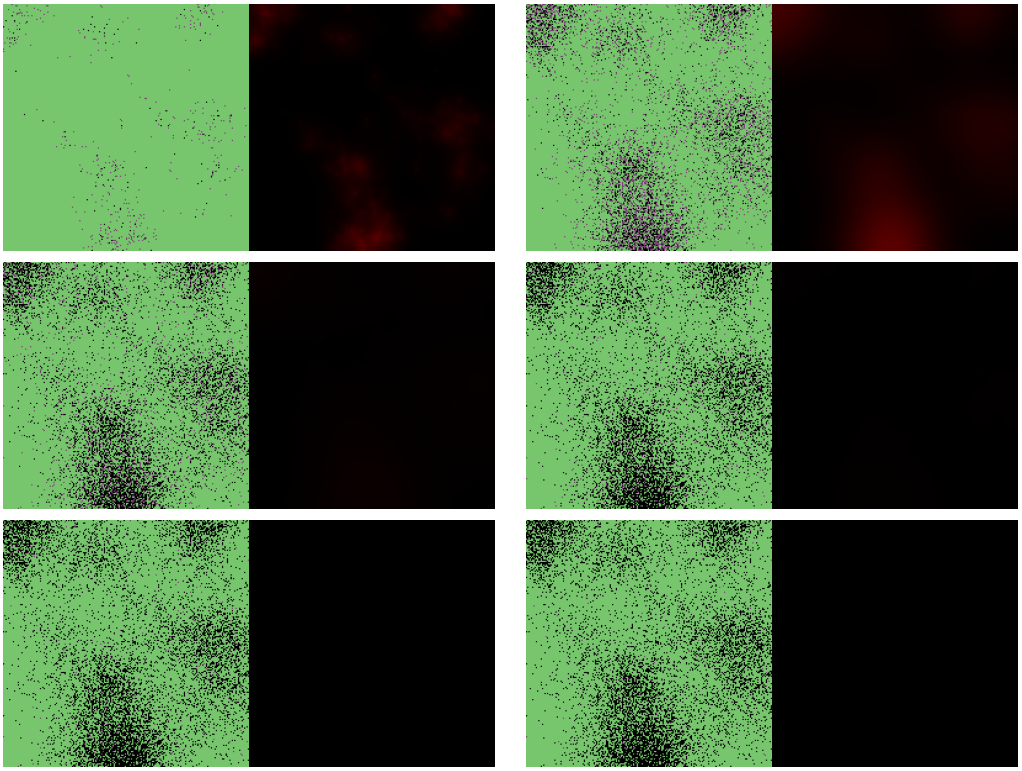

Figure 6.3.7: *Simulated spatiotemporal solutions captured (**a**) 24 hours, (**b**) 48 hours, (**c**) 72 hours, (**d**) 96, (**e**) 120, and (**f**) 144 hours after SARS–CoV–2 infection and delayed treatment with Paxlovid. In this case **ritonavir-boosted nirmatrelvir was given**, i.e. official instructions regarding Paxlovid were followed. Intervention took place after a 36-hour delay. The cellular state spaces are depicted on the left in all four subfigures; uninfected, infected and dead cells are denoted by green, purple, and black squares, respectively. Virus concentration values are shown on the right according to the scale in Figure 6.3.2.*

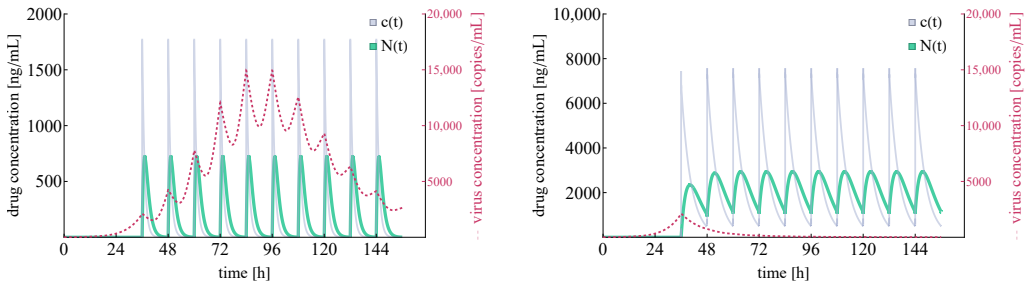

nirmatrelvir only Paxlovid

Figure 6.3.8: *Integrated virus concentration and nirmatrelvir concentration levels for two different scenarios representing nirmatrelvir-based intervention. In both cases tablets are given after a* ***36-hour delay*** *w.r.t infection initialization. Subfigure (**a**) shows the simulated outcome of applying nirmatrelvir without ritonavir, while subfigure (**b**) depicts the results of rigorous treatment with Paxlovid (ritonavir-boosted nirmatrelvir). SARS–CoV–2 virus concentrations are coloured in red (shown dashed), nirmatrelvir concentration levels – $N(t)$ and $c(t)$ – are depicted in sea green and light purple, respectively.*

Now we are ready to move on to this section's main purpose, namely, investigating outcomes and eventual averted tissue damage rates for a series of delay values with respect to the default (*i.e.* no delay) case. Note that with no particular immune response, total tissue damage (*i.e.* the ratio of cells that are either infected or already dead) after 5 days reaches 100 percent – this means that the ratio of eventually remaining susceptible target cells after Paxlovid treatment corresponds precisely to the damage that is averted because of Paxlovid.

Figure 6.3.9 illustrates the damaging effect of treatment delay from two different viewpoints.

The first one, Figure(6.3.9a) considers averted damage for a series of scenarios where each scenario assumes a 12–hour additional delay compared to the previous one. We highlight the sharp fall in effectiveness after a delay of 1.5 days: lack of timely Paxlovid-based antiviral intervention proves to be the most costly at this exact time window. For clarity we note that the expression *surviving cells* refers to the fraction of initially susceptible cells that has not become infected by the end of the observation period.

The main idea of the second approach (Figure(6.3.9b)) is to redefine the quantity on the horizontal axis: here, instead of linearly increasing delay times, the x axis follows initial damage rates (*i.e.* the level of damage that has been done until the moment treatment with Paxlovid is started). In other words, the latter approach depicts the relation between initial damage and averted damage.

Due to the lack of precise clinical data – and consequently, the relative uncertainty – regarding the exact diffusion coefficient value of SARS–CoV–2 we explore the

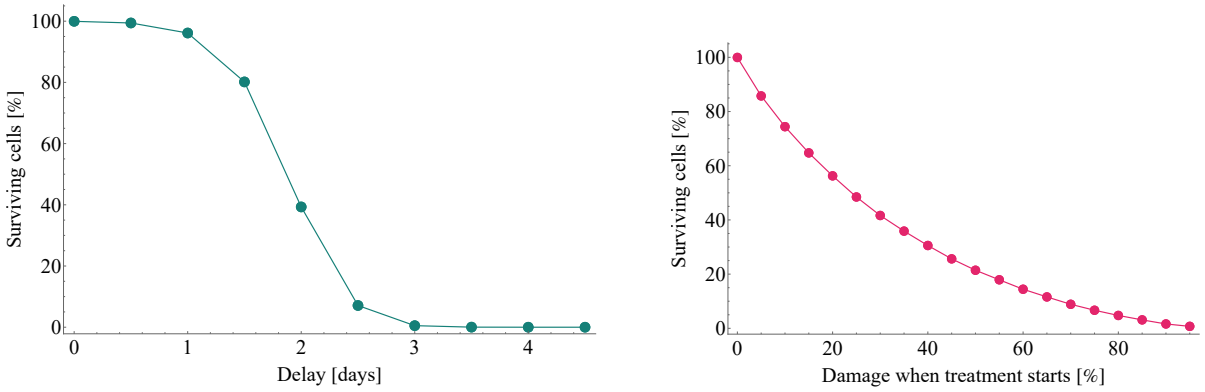

(a) **(b)**

Figure 6.3.9: *The damaging effect of treatment delay in two different approaches. Both subfigures illustrate the ratio of remaining uninfected target cells – the substantial difference between the two plots is the quantity measured on the horizontal axes. Subfigure (**a**) follows time, directly, on its x axes, while graph (**b**) depicts results w.r.t. initial damage rates. Results were calculated with the same fixed diffusion coefficient as used in chapter 4, namely,* $D_V = 0.2\sigma^2/min$.

respective sensitivity of the results shown in Figure(6.3.9b). Specifically, Figure 6.3.10 illustrates the corresponding results in a heatmap for different diffusion values. Compared to the default scenario assuming $D_V = 0.2$, the outcomes do not change substantially for even significantly higher D_V values; however, there is a clear pattern suggesting that infection outcomes are expected to be more favorable if the diffusion coefficient is several magnitudes lower.

Finally, we visualize the potency of Paxlovid in Figure 6.4.1: in this graph, we principally approach damage rates as areas. While this image is similar to Figure 6.3.9b in that the horizontal axis corresponds to initial damage, Figure 6.4.1 is ultimately structured differently. It distinguishes three types of damages and represents them as two-dimensional volumes—namely, we consider initial damage, damage after treatment initialization, and averted damage.

Naturally, the area between the $x = y$ line—depicted in (dotted) red—and the horizontal axis corresponds to the level of tissue damage suffered until the moment of Paxlovid-based intervention, i.e., initial damage.

As our next step, we visualize the unavoidable damage that occurs after intervention begins: the (dotted) curve depicted with blue shows the further damage that takes place even after the patient starts taking Paxlovid. Evidently, the area between the red line and the blue curve is the visual representation of damage after treatment initialization. This rate of damage is especially high when soaring virus concentration values are combined with a significant fraction of susceptible target cells at the initialization time of Paxlovid treatment. The latter is explained simply

by nirmatrelvir's mechanism of action: nirmatrelvir does effectively block virus production in infected cells, but it can not prevent target cells from getting infected, which is also apparent in the figure itself.

The third category, averted damage emerges in Figure 6.4.1 as the area between the blue curve and the horizontal line framing the graph from above (the latter naturally corresponds to the scenario where no medical intervention happens and full-scale damage takes place after 5 days). This shaded, light green area is the visual equivalent of the damage that is averted as a result of Paxlovid treatment, or in other words, the epithelial lung cells that are saved by this new M^{pro} inhibitor. Similarly to numerous other antiviral drugs (targeting a large variety of viruses), the principle of 'the sooner the better' proves to hold in this case, too: if intervention happens right at the beginning, almost the entire cell population can be saved by Paxlovid in case of a SARS-CoV-2 infection.

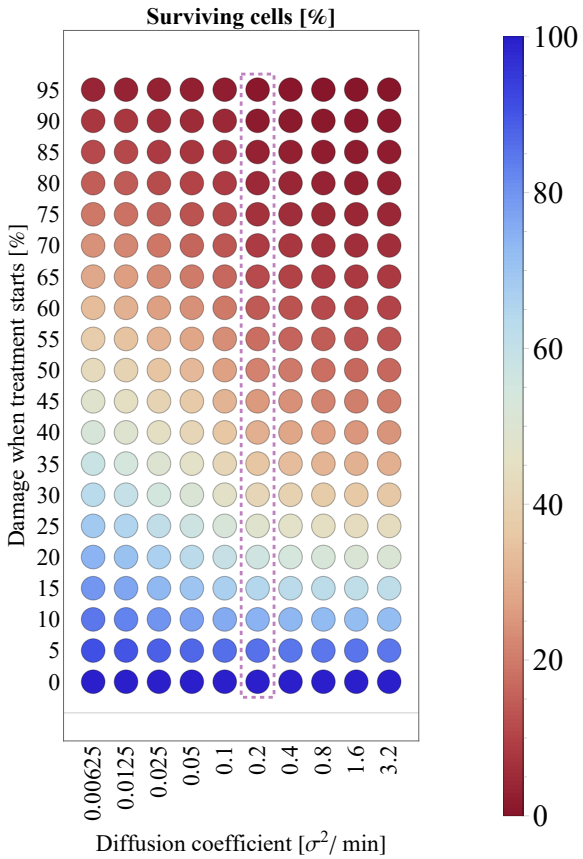

Figure 6.3.10: *Interplay between the virus diffusion coefficient (horizontal axis) and tissue damage at the initialization of Paxlovid treatment (vertical axis). The column corresponding to the particular (default) virus diffusion value of* $D_V = 0.2\sigma^2/min$ *(the one used in chapter 4) is highlighted with purple.*

6.4 Discussion

Even with worldwide vaccination programmes, SARS–CoV–2 and its newly emerging variants represent an unprecedented global challenge. Consequently, new alternative treatment options are still very much needed. This paper yields a mathematical, computation-based evaluation of one of the most promising SARS–CoV–2 inhibitors to date, Paxlovid. We implemented and carefully calibrated a multiscale mathematical framework to serve as a small *in silico* laboratory where the basic features of Paxlovid can be replicated, explained, and further investigated. Our calculations correspond to clinical expectations remarkably well: we successully replicated the outcome of a real-life *in vitro* experiment in the simulated context of our model, moreover, both the sufficiency and the necessity of Paxlovid's two main components were verified by our computations for a simplified *in vivo* case. To further improve Paxlovid's assessment, we generated a heatmap investigating the results' sensitivity to the inherently vaguely specified virus diffusion coefficient.

The proposed hybrid model has its limitations. In its present form, the system operates on a simplistic two-dimensional grid, ignoring the complex 3D geometry of the lungs, which may introduce bias or delays in the predictions. The implementation of a biologically more realistic three-dimensional structure falls beyond the scope of this study and is subject of future research. The increase of dimension (and of lattice size) inevitably affects the computational load and, hence, requires additional, technical optimization of the code in order to achieve the desired performance. Similarly, the current assumption of a constant virus clearance rate is ignoring the intricacies of the immune system that is a major limitation when considering *in vivo* scenarios. While in real life there is a significant virus release at burst, our model is averaging out the virus source over a time interval, hence we work with constant virus production rates, similarly to [69] and [70]. Consequently, this limitation is responsible for a slight overestimation regarding advancement of virus release. We note that in the context of our model it is straightforward to implement more sophisticated approaches as well (which would not be the case for example in an ODE-based system), and we also highlight that our source code includes a built-in option allowing to consider latency periods. However, that would require sufficiently detailed biological data for parametrization. Finally, we mention that our basic modeling approach to natural cellular life cycles, though being a simplification, is not expected to imply significant deviation from reality in the context of a 5-day long Paxlovid treatment: natural cell death is responsible only for circa 1% of cell population loss during this time frame according to the 17-month half-life of epithelial lung cells [68].

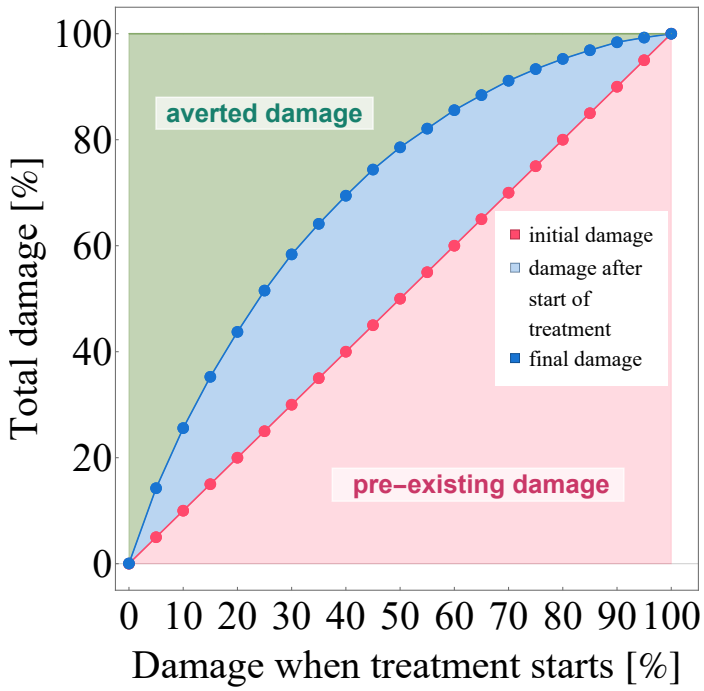

Figure 6.4.1: *The visualization of averted damage as a result of Paxlovid treatment. The quantity on the horizontal axis (and the $x = y$ line itself) represents the level of cell culture damage suffered until Paxlovid treatment begins, while data points depicted in blue show the unavoidable further damage that occurs after therapy commences. The shaded areas are a precise visual representation of initial damage (red), unavoidable post-intervention damage (blue), and averted damage (green). Evidently, the light green area represents those healthily functioning epithelial lung cells that were ultimately saved by Paxlovid.*

Despite the mathematical model's necessary simplifications and the short scope of this case study we were able to visualize and verify the importance of early interventions, moreover, we highlight that such hybrid models and computational frameworks hold a great deal of promise with applications such as supporting clinical trials by means of *in silico* experiments. Computation-based evaluation and simulation of therapies not only can enhance optimization of treatments, but a further development of this technology could also serve to reduce the need for animal testing in the future.

Summary

This PhD thesis presents models that contribute to the current state-of-the-art model for viral dynamics and cancer. The models are implemented in the HAL system. The application and adaptation of HAL system to viral dynamics is being conducted for the first time in the course of this PhD program.

The dissertation consists of three new models in Chapters 3, 4, and 6 that they use to address current and very significant questions.

Cancer model.

Development of resistance to chemotherapy in cancer patients strongly effects the outcome of the treatment. Due to chemotherapeutic agents, resistance can emerge by Darwinian evolution. Besides this, acquired drug resistance may arise via changes in gene expression. A recent discovery in cancer research uncovered a third possibility, indicating that this phenotype conversion can occur through the transfer of microvesicles from resistant to sensitive cells, a mechanism resembling the spread of an infectious agent. We present a model in chapter 3 describing the evolution of sensitive and resistant tumour cells considering Darwinian selection, Lamarckian induction and microvesicle transfer.

We also establish an agent based model as a spatial version of the ODE model and compare the outputs of the two models. We find that although the ODE model does not provide spatial information about the structure of the tumour, it is capable to determine the outcome in terms of tumour size and distribution of cell types.

The results of our models demonstrate the recent observation that some cancer cells can be transferred by microvesicles. It would be natural to observe how microvesicles affect treatment along with other factors contributing to the spread of cancer cells.

Viral dynamics for SARS-COV-2 and influenza.

We propose a hybrid partial differential equation – agent-based (PDE–ABM) model in chapter 4 to describe the spatio-temporal viral dynamics in a cell population. The virus concentration is considered as a continuous variable and virus movement is modelled by diffusion, while changes in the states of cells (i.e. healthy, infected, dead) are represented by a stochastic agent-based model. The two subsystems are intertwined: the probability of an agent getting infected in the ABM depends on the local viral concentration, and the source term of viral production in the PDE is determined by the cells that are infected.

We develop a computational tool that allows us to study the hybrid system and the generated spatial patterns in detail. We systematically compare the outputs with a classical ODE system of viral dynamics, and find that the ODE model is a good approximation only if the diffusion coefficient is large.

We demonstrate that the model is able to predict SARS–CoV–2 infection dynamics, and replicate the output of *in vitro* experiments. Applying the model to influenza as well, we can gain insight into why the outcomes of these two infections are different.

In chapter 5 we rigorously verify an experimental observation suggested by our previous simulations: once established, infections almost never disappear spontaneously. Using the powerful toolbox of branching processes we theoretically calculate the probability of extinction for a single cell and obtain an $\mathcal{O}(0.01)$ value corresponding to our expectations.

We also explore fundamental statistical features such as mean and a 95% confidence interval for the number of infected cells. The latter results visually confirm a satisfactory level of variability within the system: on the one hand it supports small and natural changes from outcome to outcome, on the other hand it clearly allows successful large-scale prediction and analysis as most infection curves remain close to the average.

Paxlovid.

Paxlovid is a promising, orally bioavailable novel drug for SARS-CoV-2 with excellent safety profiles. Our main goal in chapter 6 is to explore the pharmacometric features of this new antiviral. To provide a detailed assessment of Paxlovid, we propose a hybrid multiscale mathematical approach. We demonstrate that the results of the present in silico evaluation match the clinical expectations remarkably well: on the one hand, our computations successfully replicate the outcome of an actual in vitro experiment; on the other hand, we verify both the sufficiency and the necessity of Paxlovid's two main components (nirmatrelvir and ritonavir) for a simplified in vivo case. Moreover, in the simulated context of our computational framework, we visualize the importance of early interventions and identify the time window where a unit-length delay causes the highest level of tissue damage. Finally, the results' sensitivity to the diffusion coefficient of the virus is explored in detail.

Publications

Journal publications

[1] Attila Dénes, **Sadegh Marzban**, and Gergely Röst. Global analysis of a cancer model with drug resistance due to Lamarckian induction and microvesicle transfer. *Journal of Theoretical Biology*, 527, 110812, year = 2021 .

[2] **Sadegh Marzban**, Renji Han, Nóra Juhász, and Gergely Röst. A hybrid PDE-ABM model for viral dynamics with application to SARS-CoV-2 and influenza. *Royal Society Open Science*, 8(11), 210787, year = 2021 .

[3] Ferenc A. Bartha, Nóra Juhász, **Sadegh Marzban**, Renji Han, and Gergely Röst. In Silico Evaluation of Paxlovid's Pharmacometrics for SARS-CoV-2: A Multiscale Approach. *Viruses*, 14(5), 1103, year = 2022 .

Bibliography

[1] Macal CM, North MJ. Tutorial on agent-based modeling and simulation. In Proceedings of the Winter Simulation Conference, 2005. 2005 Dec 4 (pp. 14-pp). IEEE.

[2] Airley, R., 2009. *Cancer chemotherapy*, Wiley-Blackwell.

[3] Skeel, R.T., 2007. *Handbook of cancer chemotherapy*, Lippincott Williams & Wilkins.

[4] Easwaran, H., Tsai, H.-C., Baylin, S. B., 2014. Cancer epigenetics: tumour heterogeneity, plasticity of stem-like states, and drug resistance. Mol. Cell 54, 716–727, https://doi.org/10.1016/j.molcel.2014.05.015.

[5] Gerlinger, M., Swanton, C., 2010. How Darwinian models inform therapeutic failure initiated by clonal heterogeneity in cancer medicine. Br. J. Cancer 103, 1139–1143, https://doi.org/10.1038/sj.bjc.6605912.

[6] Gillies, R. J., Verduzco, D., Gatenby, R. A., 2012. Evolutionary dynamics of carcinogenesis and why targeted therapy does not work. Nat.Rev. Cancer 12, 487–493, https://doi.org/10.1038/nrc3298.

[7] Li, Q. et al., 2016. Dynamics inside the cancer cell attractor reveal cell heterogeneity, limits of stability, and escape. Proc. Natl. Acad. Sci.USA 113, 2672–2677, https://doi.org/10.1073/pnas.1519210113.

[8] Pisco, A. et al., 2013. Non-Darwinian dynamics in therapy-induced cancer drug resistance. Nat. Commun. 4, 2467. https://doi.org/10.1038/ncomms3467

[9] Bebawy, M. et al. 2009. Membrane microparticles mediate transfer of p-glycoprotein to drug sensitive cancer cells. Leukemia 23, 1643–1649, https://doi.org/10.1038/leu.2009.76.

[10] Cesi, G. et al. 2016. Transferring intercellular signals and traits between cancer cells: extracellular vesicles as “homing pigeons”. Cell Commun. Signal. 14, Art. No. 13,https://doi.org/10.1186/s12964-016-0136-z.

[11] Lopes-Rodrigues, V. et al., 2017. Identification of the metabolic alterations associated with the multidrug resistant phenotype in cancer and their intercellular transfer mediated by extracellular vesicles. Sci. Rep. **7**, 44541, `https://doi.org/10.1038/srep44541`.

[12] Amy L. Bauer, Catherine A.A. Beauchemin, Alan S. Perelson, Agent-based modeling of host–pathogen systems: The successes and challenges, Information Sciences, Volume 179, Issue 10, 2009, Pages 1379-1389, ISSN 0020-0255, https://doi.org/10.1016/j.ins.2008.11.012.

[13] Catherine Beauchemin, Probing the effects of the well-mixed assumption on viral infection dynamics, Journal of Theoretical Biology, Volume 242, Issue 2, 2006, Pages 464-477, ISSN 0022-5193, https://doi.org/10.1016/j.jtbi.2006.03.014.

[14] Georg A. Funk, Vincent A.A. Jansen, Sebastian Bonhoeffer, Timothy Killingback, Spatial models of virus-immune dynamics, Journal of Theoretical Biology, Volume 233, Issue 2, 2005, Pages 221-236, ISSN 0022-5193, https://doi.org/10.1016/j.jtbi.2004.10.004.

[15] Claude-Michel Brauner,Danaelle Jolly,Luca Lorenzi,Rodolphe Thiebaut, Heterogeneous viral environment in a HIV spatial model,Discrete and Continuous Dynamical Systems.

[16] Eric Bonabeau, Agent-based modeling: Methods and techniques for simulating human systems, Proceedings of the National Academy of Sciences, 99,suppl_-3,7280-7287,2002 doi = 10.1073/pnas.082080899.

[17] Hwang SW, Kirst MJ, Chiu S, Tolomiczenko G, Kiss A, Cowan L, Levinson W. Multidimensional social support and the health of homeless individuals. J Urban Health. 2009 Sep;86(5):791-803. doi: 10.1007/s11524-009-9388-x. Epub 2009 Jul 23. PMID: 19629703; PMCID: PMC2729873.

[18] Glen CM, Kemp ML, Voit EO (2019) Agent-based modeling of morphogenetic systems: Advantages and challenges. PLOS Computational Biology 15(3): e1006577. https://doi.org/10.1371/journal.pcbi.1006577.

[19] Cilfone NA, Perry CR, Kirschner DE, Linderman JJ. Multi-scale modeling predicts a balance of tumor necrosis factor-α and interleukin-10 controls the granuloma environment during Mycobacterium tuberculosis infection. PLoS One. 2013 Jul 15;8(7):e68680. doi: 10.1371/journal.pone.0068680.

[20] Figueredo GP, Joshi TV, Osborne JM, Byrne HM, Owen MR. On-lattice agent-based simulation of populations of cells within the open-source Chaste framework. http://doi.org/10.1098/rsfs.2012.0081.

[21] Segovia-Juarez JL, Ganguli S, Kirschner D. Identifying control mechanisms of granuloma formation during M. tuberculosis infection using an agent-based model. J Theor Biol. 2004;231:357–76.

[22] Fallahi-Sichani, Mohammad,El-Kebir, Mohammed, Marino, Simeone, Kirschner, Denise E. Linderman, Jennifer J, Multiscale Computational Modeling Reveals a Critical Role for TNF-α Receptor 1 Dynamics in Tuberculosis Granuloma Formation, The Journal of Immunology, 10.4049/jimmunol.1003299.

[23] Zaiyi Guo, Peter M.A. Sloot, Joc Cing Tay, A hybrid agent-based approach for modeling microbiological systems, Journal of Theoretical Biology, Volume 255, Issue 2, 2008, Pages 163-175, ISSN 0022-5193, https://doi.org/10.1016/j.jtbi.2008.08.008.

[24] Zhihui Wang, Joseph D. Butner, Romica Kerketta, Vittorio Cristini, Thomas S. Deisboeck, Simulating cancer growth with multiscale agent-based modeling, Seminars in Cancer Biology, Volume 30, 2015, Pages 70-78, ISSN 1044-579X, https://doi.org/10.1016/j.semcancer.2014.04.001.

[25] Dada Joseph O.,Mendes Pedro, Multi-scale modelling and simulation in systems biology , 2011, Pages 86-96, Integrative Biology, VL 3, IS 2 The Royal Society of Chemistry, http://dx.doi.org/10.1039/C0IB00075B

[26] Angermann, B., Klauschen, F., Garcia, A. et al. Computational modeling of cellular signaling processes embedded into dynamic spatial contexts. Nat Methods 9, 283–289 (2012). https://doi.org/10.1038/nmeth.1861

[27] Bailey AM, Lawrence MB, Shang H, Katz AJ, Peirce SM (2009) Agent-Based Model of Therapeutic Adipose-Derived Stromal Cell Trafficking during Ischemia Predicts Ability To Roll on P-Selectin. PLOS Computational Biology 5(2): e1000294. https://doi.org/10.1371/journal.pcbi.1000294.

[28] Kaul H, Cui Z, Ventikos Y (2013) A Multi-Paradigm Modeling Framework to Simulate Dynamic Reciprocity in a Bioreactor. PLOS ONE 8(3): e59671. https://doi.org/10.1371/journal.pone.0059671

[29] Bravo RR, Baratchart E, West J, Schenck RO, Miller AK, Gallaher J, Gatenbee CD, Basanta D, Robertson-Tessi M, Anderson AR. Hybrid Automata Library: A flexible platform for hybrid modeling with real-time visualization. PLoS computational biology. 2020 Mar 10;16(3):e1007635.

[30] McNamee, N. et al., 2018. Extracellular vesicles and anti-cancer drug resistance. BBA Rev. Cancer 1870, 123–136, https://doi.org/10.1016/j.bbcan.2018.07.003.

[31] Samuel, P. et al., 2017. Mechanisms of drug resistance in cancer: the role of extracellular vesicles. Proteomics 17, 1600375, https://doi.org/10.1002/pmic.201600375.

[32] Arduin H, de Cellès MD, Guillemot D, Watier L, Opatowski L. An agent-based model simulation of influenza interactions at the host level: insight into the influenza-related burden of pneumococcal infections. BMC infectious diseases. 2017 Dec;17(1):1-2.

[33] Sousa, D. et al., 2015. Intercellular transfer of cancer drug resistance traits by extracellular vesicles. Trends Mol. Med. 21, 595–608, https://doi.org/10.1016/j.molmed.2015.08.002.

[34] Álvarez-Arenas, A. et al., 2019. Interplay of Darwinian selection, Lamarckian induction and microvesicle transfer on drug resistance in cancer. Sci. Rep. 9, Article No. 9332. https://doi.org/10.1038/s41598-019-45863-z

[35] Dénes, A., Röst, G., 2020. Global analysis of a cancer model with drug resistance due to microvesicle transfer, in: R. P. Mondaini (Ed.), *Trends in biomathematics: modeling cells, flows, epidemics, and the environment*, Springer, Cham, pp. 71–80, https://doi.org/10.1007/978-3-030-46306-9_5.

[36] DeConti, R.D. et al., 1973. Clinical and pharmacological studies with cis-Diamminedichloroplatinum(II), Cancer Res. 33, 1310–1315.

[37] Durán, M.R. et al., 2016. Transfer of drug resistance characteristics between cancer cell subpopulations: a study using simple mathematical models, Bull. Math. Biol. 78, 1218–1237.

[38] Liu, X. et al., 2018. A deterministic and stochastic model for the system dynamics of tumour–immune responses to chemotherapy, Physica A 500, 162–176.

[39] Niiranen, A. et al., 1992. Adjuvant chemotherapy after radical surgery for non-small-cell lung cancer: A randomized study, J. Clin. Oncol. 10, 1927–1932, https://dx.doi.org/10.1200/JCO.1992.10.12.1927.

[40] Luqmani, Y.A., 2005. Mechanisms of drug resistance in cancer chemotherapy, *Med. Princ. Pract.* **15**, Suppl. 1, 35–48.

[41] Nowak M, May RM. Virus dynamics: mathematical principles of immunology and virology. Oxford University Press, UK. 2000 Nov 23.

[42] Baccam P, Beauchemin C, Macken CA, Hayden FG, Perelson AS. Kinetics of influenza A virus infection in humans. Journal of virology. 2006 Aug 1;80(15):7590-9.

[43] Peter S, Dittrich P, Ibrahim B. Structure and hierarchy of SARS-CoV-2 infection dynamics models revealed by reaction network analysis. Viruses. 2021 Jan;13(1):14.

[44] Cilfone NA, Kirschner DE, Linderman JJ. Strategies for efficient numerical implementation of hybrid multi-scale agent-based models to describe biological systems. Cellular and molecular bioengineering. 2015 Mar;8(1):119-36.

[45] Bar-On YM, Flamholz A, Phillips R, Milo R. Science Forum: SARS-CoV-2 (COVID-19) by the numbers. elife. 2020 Mar 31;9:e57309.

[46] Carcaterra M, Caruso C. Alveolar epithelial cell type II as main target of SARS-CoV-2 virus and COVID-19 development via NF-Kb pathway deregulation: A physio-pathological theory. Medical Hypotheses. 2021 Jan 1;146:110412.

[47] Mason RJ. Biology of alveolar type II cells. Respirology. 2006 Jan;11:S12-5.

[48] Beauchemin C, Forrest S, Koster FT. Modeling influenza viral dynamics in tissue. In International Conference on Artificial Immune Systems 2006 Sep 4 (pp. 23-36). Springer, Berlin, Heidelberg.

[49] Marzban S, Han R, Juhász N, Röst G. Hybrid PDE-ABM model for viral dynamics. 2021. doi:10.5281/zenodo.4758518

[50] Bocharov GA, Romanyukha AA. Mathematical model of antiviral immune response III. Influenza A virus infection. Journal of Theoretical Biology. 1994 Apr 21;167(4):323-60.

[51] Hernandez-Vargas EA, Velasco-Hernandez JX. In-host Mathematical Modelling of COVID-19 in Humans. Annu Rev Control. 2020;50: 448–456

[52] Hernandez-Vargas EA. Modeling and Control of Infectious Diseases in the Host: With MATLAB and R. Academic Press. 2019 Feb 14.

[53] Yang W, Elankumaran S, Marr LC. Concentrations and size distributions of airborne influenza A viruses measured indoors at a health centre, a day-care centre and on aeroplanes. Journal of the Royal Society Interface. 2011 Aug 7;8(61):1176-84.

[54] Sego TJ, Aponte-Serrano JO, Ferrari Gianlupi J, Heaps SR, Breithaupt K, Brusch L, Crawshaw J, Osborne JM, Quardokus EM, Plemper RK, Glazier JA. A modular framework for multiscale, multicellular, spatiotemporal modeling of acute primary viral infection and immune response in epithelial tissues and its application to drug therapy timing and effectiveness. PLoS computational biology. 2020 Dec 21;16(12):e1008451.

[55] Smith HL. Monotone dynamical systems: an introduction to the theory of competitive and cooperative systems: an introduction to the theory of competitive and cooperative systems. American Mathematical Soc.; 2008.

[56] Ye QY, Li ZY, Wang MX et al. Introduction to reaction-diffusion equations (in Chinese). Science Press, Beijing. 2011.

[57] Abuin P, Anderson A, Ferramosca A, Hernandez-Vargas EA, Gonzalez AH. Characterization of SARS-CoV-2 dynamics in the host. Annual reviews in control. 2020 Oct 6.

[58] Van den Driessche P, Watmough J. Reproduction numbers and sub-threshold endemic equilibria for compartmental models of disease transmission. Mathematical biosciences. 2002 Nov 1;180(1-2):29-48.

[59] Outlaw VK, Bovier FT, Mears MC, Cajimat MN, Zhu Y, Lin MJ, Addetia A, Lieberman NA, Peddu V, Xie X, Shi PY. Inhibition of coronavirus entry in vitro and ex vivo by a lipid-conjugated peptide derived from the SARS-CoV-2 spike glycoprotein HRC domain. MBio. 2020 Sep 1;11(5):e01935-20.

[60] Carrat F, Vergu E, Ferguson NM, Lemaitre M, Cauchemez S, Leach S, Valleron AJ. Time lines of infection and disease in human influenza: a review of volunteer challenge studies. American journal of epidemiology. 2008 Apr 1;167(7):775-85.

[61] Marzban S, Han R, Juhász N, Röst G. A hybrid PDE–ABM model for viral dynamics with application to SARS–CoV–2 and influenza. Royal Society Open Science. 2021. https://doi.org/10.1098/rsos.210787

[62] Allen LJ. An introduction to stochastic processes with applications to biology. CRC press; 2010 Dec 2.

[63] Pfizer. PAXLOVID™ (nirmatrelvir tablers; ritonavir tablets). *Pfizer Medical Information* **2022**.

[64] Owen, D.R.; Allerton, C.M.; Anderson, A.S.; Aschenbrenner, L.; Avery, M.; Berritt, S.; Boras, B.; Cardin, R.D.; Carlo, A.; Coffman, K.J.; Dantonio, A.; et al. An oral SARS-CoV-2 Mpro inhibitor clinical candidate for the treatment of COVID-19. *Science* **2021 Dec 24**;*374(6575)*:1586–93. [CrossRef] [PubMed]

[65] FDA. Fact Sheet For Healthcare Providers: Emergency Use Authoriziation for Paxlovid™. *United States Food and Drug Administration* **2022**. Available online: `https://www.fda.gov/media/155050/download` (accessed on 21 April 2022).

[66] EMA. Annex I – Conditions of Use, Conditions for Distribution and Patients Targeted and Conditions for Safety Monitoring Addressed to Member States – for Unauthorised Product – Paxlovid (PF-07321332 150 mg and ritonavir 100 mg) – Available for Use. *European Medicines Agency* **2022**. (accessed on 21 April 2022).

[67] Perelson, A.S.; Ke, R. Mechanistic modeling of SARS–CoV–2 and other infectious diseases and the effects of therapeutics. *Clin Pharmacol Ther* **2021 Apr**;*109(4)*:829-40. [CrossRef] [PubMed]

[68] Rawlins, E.L.; Hogan, B.L.M. Ciliated epithelial cell lifespan in the mouse trachea and lung. *Am J Physiol Lung Cell Mol Physiol* **2008 Jul**;*295(1)*:L231–4. [CrossRef] [PubMed]

[69] Lord, J.S.; Bonsall, M.B. The evolutionary dynamics of viruses: virion release strategies, time delays and fitness minima. *Virus Evol* **2021 Apr 27**;*7(1)*:veab039. [CrossRef] [PubMed]

[70] Perelson, A.S. Modelling viral and immune system dynamics. *Nat Rev Immunol* **2002 Jan**;*2(1)*:28–36. [CrossRef] [PubMed]

[71] Hernandez-Vargas, E.A.; Velasco-Hernandez, J.X. In-host mathematical modelling of COVID-19 in humans. *Annu Rev Control* **2020 Jan 1**;*50*:448–456. [CrossRef] [PubMed]

[72] Laurent, G.J.; Shapiro, S.D. (eds). *Encyclopedia of respiratory medicine*, Vol. 3., 1st ed.; Academic Press: Cambridge, Massachusetts, USA, 2006. [CrossRef]

[73] Willführ, A.; Brandenberger, C.; Piatkowski, T.; Grothausmann, R.; Nyengaard, J.R.; Ochs, M.; Mühlfeld, C. Estimation of the number of alveolar capillaries by the Euler number (Euler-Poincaré characteristic). *Am J Physiol Lung Cell Mol Physiol* **2015 Dec 1**;*309(11)*:L1286-93. [CrossRef] [PubMed]

[74] Singh, R.S.; Toussi, S.S.; Hackman, F.; Chan, P.L.; Rao, R.; Allen, R.; Van Eyck, L.; Pawlak, S.; Kadar, E.P.; Clark, F.; Shi, H. Innovative Randomized Phase 1 Study and Dosing Regimen Selection to Accelerate and Inform Pivotal COVID-19 Trial of Nirmatrelvir. *Clin Pharmacol Ther* **2022 Apr 7**. [CrossRef] [PubMed]

[75] Goyal, A.; Cardozo-Ojeda, E.F.; Schiffer, J.T. Potency and timing of antiviral therapy as determinants of duration of SARS-CoV-2 shedding and intensity of inflammatory response. *Sci Adv* **2020 Nov 20**;*6(47)*:eabc7112. [CrossRef] [PubMed]

[76] Hu, W.J.; Chang, L.; Yang, Y.; Wang, X.; Xie, Y.C.; Shen, J.S.; Tan, B.; Liu, J. Pharmacokinetics and tissue distribution of remdesivir and its metabolites nucleotide monophosphate, nucleotide triphosphate, and nucleoside in mice. *Acta Pharmacol Sin* **2021 Jul**;*42(7)*:1195-1200. [CrossRef] [PubMed]

[77] Olkkola, K.T.; Palkama, V.J.; Neuvonen, P.J. Ritonavir's role in reducing fentanyl clearance and prolonging its half-life. *Anesthesiology* **1999 Sep**;*91(3)*:681-5. [CrossRef] [PubMed]

[78] Bartha, F.A.; Juhász, N.; Marzban, S.; Han, R; Röst, G. Supplementary codes for *In silico* evaluation of Paxlovid's pharmacometrics for SARS–CoV–2: a multiscale approach. *Github* **2022.** Available online: `https://github.com/epidelay/paxlovid-x-sars-cov-2` (accessed on 21 April 2022).

Acknowledgments

First of all, I would like to thank my supervisor, Gergely Röst, for directing my PhD studies. I would also like to thank my colleagues and friends who helped me to realize the results presented here and to enjoy the period of my studies. Last, but not least, I wish to thank my wife and family for their constant love and support.